New Concepts for Functional 0-3 Nanocomposites and Magnetic Field Sensors

Dissertation

zur Erlangung des akademischen Grades
Doktor der Ingenieurwissenschaften
(Dr.-Ing.)
der Technischen Fakultät
der Christian-Albrechts-Universität zu Kiel

Björn Gojdka

Kiel
2012

1. Gutachter: Prof. Dr. Franz Faupel

2. Gutachter: Prof. Dr. Lorenz Kienle

3. Gutachter: Prof. Dr. Andreas Heilmann

Datum der mündlichen Prüfung: 28.11.2012

In Memory of Dr. Vladimir Zaporojtchenko

Scientist, Colleague, Friend

Abstract

A novel physical vapor deposition (PVD) concept for the precise tailoring of functional granular (0-3) nanocomposites has been developed in Part I. In order to realize the deposition concept experimentally, a new high-vacuum deposition system is designed and constructed. As part of the concept, the separation of the matrix deposition and nanoparticle formation by a gas aggregation cluster source (GAS) enables advanced deposition process control. Making use of the technique, functional 0-3 nanocomposites are tailored and investigated regarding their suitability as magnetoelectric (ME) and high-k materials. Prior to the production of 0-3 nanocomposites, individual deposition processes are developed for the composite constituents and the latter are characterized separately.

For the first time, the self-constructed GAS of the research group is used in order to produce magnetic nanoparticles. The output characteristic of the GAS and the properties of the resulting Cobalt (Co) nanoparticles are characterized. The particles exhibit a narrow size distribution and are of homogeneous spherical shape as desired for high-k materials. Both the deposition rate and the lateral deposition profile of the GAS are highly tunable by the process gas flow, allowing flexible adjustment of the GAS output for the co-deposition process. Co nanoparticle films with a thickness of several hundreds of nm are found to be ferromagnetic at room temperature and to exhibit high porosity which could be of relevance for example in catalytic applications and for sensors.

Aiming for the nanoengineering of ME and high-k materials, aluminum nitride (AlN) is chosen as the matrix material due to its dielectric and piezoelectric properties. Since AlN is required to be highly textured in order to exhibit piezoelectricity, a respective deposition process is developed. For the first time in the research group, reactive sputtering is established, using a metallic Al target and N_2 process gas. In order to stabilize the reactive process, pulsed DC power is applied, as well for the first time in the research group. The developed process yields exclusively c-axis oriented AlN with a full width at half maximum (FWHM) rocking curve below 2°. The piezoelectric constant of $d_{33,\mathrm{f}} \approx 5\,\mathrm{pm/V}$ and dielectric permittivity $\varepsilon \approx 10$ of the deposits are in good agreement with values reported in other studies for high-quality AlN.

The individual deposition processes are subsequently joined in order to co-deposit 0-3 AlN/Co nanocomposites. It is found that the preformed nanoparti-

cles charge electrically in the plasma of the matrix deposition. As a consequence the particles do not reach the substrate if the latter is electrically floating, too. A quasi-co-sputtering concept is developed in order to circumvent the repulsion of the particles. Magnetic 0-3 AlN/Co nanocomposites are successfully produced, demonstrating the feasibility of the novel deposition concept and the functionality of the newly constructed deposition system. Subsequently, the AlN/Co nanocomposites are characterized regarding their suitability as ME and high-k materials.

The dielectric permittivity of the AlN/Co composites is increased by up to a factor of 30. However, dielectric loss and dc leakage currents increase drastically. While the composites require further optimization in order to attain technical relevance, the results demonstrate the general feasibility of the developed deposition concept for the PVD of high-k materials. So far, high-k cermets have been prepared only by sintering, limiting their reproducibility and applicability.

Regarding the suitability as ME materials, several inherent drawbacks of the 0-3 approach with metallic particles are identified. The crystallinity of the AlN matrix is found to degrade due to the inclusion of nanoparticles already at low filling factors, diminishing the piezoelectric effect. Further challenges are posed by the increased dielectric permittivity and deteriorated insulating properties of the composite. Based on the results, the 0-3 nanocomposite approach with metallic particles appears to be unsuitable for the fabrication of high-performance ME materials and respective existing literature is critically discussed.

While in Part I the granular ME nanocomposite approach is investigated for magnetic sensing, in Part II a novel magnetic field sensor based on a laminar (2-2) geometry is presented. Both projects belong to the SFB 855 "*Magnetoelectric Composites - Future Biomagnetic Interfaces*" which aims at the development of a new generation of magnetic field sensors especially for biomagnetic applications. A proof-of-principle study is conducted with a mechanically excited MEMS-oscillator which is coated with an amorphous $(Fe_{90}Co_{10})_{78}Si_{12}B_{10}$ functional layer. Young's modulus E of the latter can be modified due to the delta-E effect by application of magnetic fields. As a consequence, the resulting shift of the oscillator's resonance frequency can be exploited to measure magnetic fields. The demonstrator is shown to detect magnetic fields as low as 400 nT and optimized future designs might reach sensitivities below 100 pT. The novel concept is sensitive to biomagnetically relevant low-frequency magnetic fields, requires no cooling, possesses vector-field capacity and is potentially fully integrable. The journal *Nature* presented the concept as a research highlight.

Contents

List of acronyms

ac	**a**lternating **c**urrent
AFM	**A**tomic **F**orce **M**icroscopy/**M**icroscope
BCC	**B**ody **C**entred **C**ubic
BTO	**B**a**T**i**O**$_3$; Barium Titanate
DBLI	**D**ouble **B**eam **L**aser **I**nterferometer
dc	**d**irect **c**urrent
DSP	**D**ouble-**S**ide **P**olished
EDX	**E**nergy-**D**ispersive **X**-ray spectroscopy
EFTEM	**E**nergy-**F**iltered **T**ransmission **E**lectron **M**icroscopy
FCC	**F**ace **C**entred **C**ubic
FIB	**F**ocused **I**on **B**eam
FWHM	**F**ull **W**idth at **H**alf **M**aximum
GAS	**G**as **A**ggregation Cluster **S**ource
HCP	**H**exagonal **C**losed **P**acked
HRTEM	**H**igh **R**esolution **T**ransmission **E**lectron **M**icroscope
HV	**H**igh **V**acuum
ICP-MS	**I**nductively **C**oupled **P**lasma - **M**ass **S**pectroscopy
ME	**M**agneto**e**lectric
MEMS	**M**icro**e**lectro**m**echanical **S**ystems
MD	**M**ulti**d**omain
PLL	**P**hase **L**ocked **L**oop
PSD	**P**osition **S**ensitive **D**etector
PZT	**P**b [**Z**r$_x$**T**i$_{1-x}$] **O**$_3$; Lead Zirconate Titanate
QCM	**Q**uartz **C**rystal **M**icrobalance
rf	**R**adio **F**requency
rms	**R**oot **M**ean **S**quare
SAED	**S**elective **A**rea **E**lectron **D**iffraction
SCCM	**S**tandard **C**ubic **C**entimeters per **M**inute
SD	**S**ingle**d**omain
SEM	**S**canning **E**lectron **M**icroscope**M**icroscopy
SP	**S**uper**p**aramagnetic
TEM	**T**ransmission **E**lectron **M**icroscope/**M**icroscopy
TMP	**T**urbo **M**olecular **P**ump
VSM	**V**ibrating **S**ample **M**agnetometer
XRD	**X**-**R**ay **D**iffraction

List of mathematical symbols

A; $\hat{A}$	area; amplitude
B	magnetic flux density
C	capacitance
d	distance; thickness
d_{ij}	piezoelectric coefficient
D	electric displacement; particle diameter
E	energy; electric field; Young's modulus
f	frequency
f_{dc}	frequency of pulsed DC power for magnetron sputtering
f_{p}	pulsing frequency of quasi-co-sputtering
H; H_{C}	magnetic field; coercive field
I	current
J	current density
k	spring constant
k_{B}	Boltzmann's constant
K	anisotropy
l	length
m; M; M_{S}	magnetic moment; magnetization; saturation magnetization
p_{main}; p_{LL}	pressure in main chamber and in transfer load lock
P	polarization; discharge power
p^m	piezomagnetic coefficient
R	resistance
S	mechanical strain
s	elastic compliance
t	time
T; T_{C}; T_{N}	temperature; Curie-temperature; Néel-temperature
U; U_{t}; U_{s}	voltage; target bias; sample bias
V	volume
Z	impedance
α	magnetoelectric coefficient
ε_r; ε_r'; ε_r''	relative dielectric permittivity; real part of ε_r; imaginary part of ε_r

List of mathematical symbols

(continued)

ϕ	x-ray incident angle in rocking curve geometry
Φ	gas flow
$\Phi_{\mathrm{Ar,0}}$	Ar gas flow through center magnetron
$\Phi_{\mathrm{Ar,GAS}}$	Ar gas flow through gas aggregation cluster source
λ	magnetostrictive strain; wavelength
λ_{S}	saturation magnetostriction
$\lambda_{\mathrm{S,i}}$	saturation magnetostriction of ideal demagnetized state
λ_{P}	saturation magnetostriction of polycrystalline specimen
μ; μ_0	magnetic permeability; magnetic permeability of free space
θ	x-ray incident angle in 2θ geometry
ρ; ρ_{C}	density; volume filling factor; percolation threshold
σ	mechanical stress; electrical conductivity
ω	angular frequency

Part I

0-3 Functional Nanocomposites

Chapter 1

Part I - Introduction

Functional nanocomposites represent a vast field of research and application.[1] They have already been used for centuries, for example in order to color the windows of medieval churches. Back then, however, the application of nanocomposites was simply based on empirical experience and was by no means connected with fundamental physical understanding. During the last decades significant advances both in preparation and characterization of nanocomposites have drastically increased the understanding and facilitation of nanocomposites.

Nowadays, functional nanocomposites of various geometries can be prepared from a tremendous range of materials by a wide variety of techniques like sintering, sol-gel, thermal evaporation and magnetron sputtering, each technique with its own (dis-)advantages. However, modern applications of nanocomposites require a precise tailoring of the composite morphology, filling factor, electrical properties and chemical composition. Dry physical vapor deposition (PVD) techniques provide a versatile tools for the deposition of functional composites. A common PVD technique is magnetron sputtering, which has already been introduced in the 1970's[2] and since then has been further refined by advanced operation modes like reactive[3] or pulsed[4] sputtering. Magnetron based deposition has been widely employed to prepare self-organized granular nanocomposites by co-deposition for various material combinations.[1,5] However, the realization of nanocomposites comprising reactive nanoparticles is still challenging by co-sputtering. This holds for most magnetic metals and alloys, while especially magnetic nanocomposits possess high application potential.

With the development of gas aggregation cluster sources (GAS) in the 1980's[6] and 1990's[7] a new PVD tool has been available for the production of nanoparticles. The separation of the cluster formation process and the matrix deposition promises advanced control over the morphology and the composition of granular nanocomposites. In turn, a deposition concept combining a GAS and conventional magnetron sputtering should enable the tailoring of a wide variety of granular nanocomposites including magnetic ones.

Such advanced process control is required in various research areas like per-

colative materials with high dielectric permittivity (high-k)[8] and magnetoelectric (ME) composites[9]. For high-k materials, a precise control of the composite composition[10] and the particle shape[11] is required in order to yield reproducible results. In addition, high-k cermets have been prepared so far only by sintering and a suitable PVD preparation route would increase their technical applicability.

The preparation of granular ME composites is a challenging task since such materials require the combination of a piezoelectric matrix on the one hand and magnetic particles on the other hand. Accordingly, both the crystallographic structure and the chemical composition of the composite have to be well controlled. In addition, a good mechanical coupling between the two phases has to be achieved. The suitability of a nanogranular approach with metallic magnetic particles for ME nanocomposites will be studied based on the advanced process control provided by the PVD concept which is to be developed in the course of this work.

In summary the aims of Part I of this work are as follows:

1. to develop a versatile deposition concept which is capable of tailoring a wide variety of functional granular nanocomposites. This task includes the design and construction of a new high-vacuum deposition system.

2. to produce and characterize magnetic granular nanocomposites as a proof-of-principle demonstration of the aforementioned deposition concept.

3. to study the feasibility of the deposition concept as a PVD preparation route for the design of percolative high-k nanocomposites.

4. to study the feasibility of a granular nanocomposite approach with metallic particles for ME composites.

Part I is organized as follows: the fundamental theoretical aspects of the tasks are discussed in chapter 2, including the physical phenomena exploited in ME and high-k materials. In chapter 3, the high-vacuum deposition system which was constructed in the course of this work is presented and the employed characterization procedures are discussed. Prior to the deposition of nanocomposites, the composite constituents are investigated individually in chapter 4. Subsequently, the developed deposition concept is presented and the resulting nanocomposites are investigated regarding their suitability for high-k and ME materials in chapter 5.

Chapter 2

Theory

The following chapter covers the theoretical background of Part I of this thesis. First, fundamental physical phenomena are addressed which provide the basis for the subsequent review of magnetoelectric (ME) and high-k nanocomposite applications. Motivated by the requirements of ME and high-k materials, the choice of aluminum nitride (AlN) and cobalt (Co) as a demonstrator system is discussed. Subsequently, key aspects of the PVD methods employed in the course of this work for the deposition of AlN/Co nanocomposites are presented. Finally, relevant characterization techniques are discussed including peculiarities which have to be taken into account for the interpretation of experimental results.

2.1 Fundamental Physical Phenomena

2.1.1 Piezoelectricity

The direct piezoelectric effect was discovered by the Curie brothers in 1880.[12] It describes the property of a crystalline material to develop an electric polarization P proportional to an applied mechanical stress σ

$$P_i = d_{ijk}\,\sigma_{jk} \qquad \text{(using Einstein's sum convention)} \tag{2.1}$$

where d_{ijk} are the piezoelectric coefficients. The positive and negative centers of charge in a crystal are being displaced with respect to each other upon application of a mechanical stress only if the crystal structure is non-centrosymmetric. Accordingly, 20 of the 21 non-centrosymmetric crystal classes exhibit the piezoelectric effect, excluding the cubic class 432 in which other symmetries cancel out the effect.[13]

Subsequently, Lippmann[14] predicted in 1881 the converse piezoelectric effect, describing a mechanical strain of a material upon application of an electric field. His prediction was experimentally confirmed again by the Curie brothers[15].

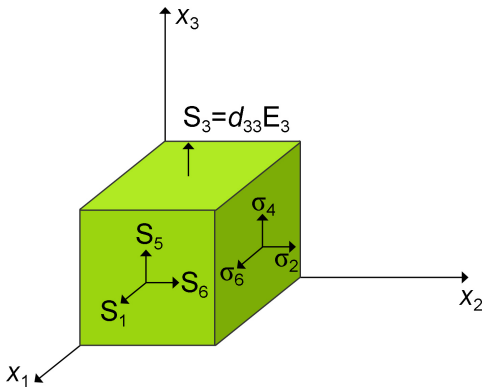

Notation	
Tensor	Matrix
11	1
22	2
33	3
23,32	4
31,13	5
12,21	6

FIG. 2.1: Visualization of the matrix notation with examples of stress and strain directions. Refer to text for details.

The direct and converse piezoelectric effect can be described by the constitutive equations

$$D_i = d_{ijk}\,\sigma_{jk} + \varepsilon^{\sigma}_{ij}\,E_j \tag{2.2}$$

$$S_{ij} = d_{ijk}\,E_k + s^{E}_{ijkl}\,\sigma_{kl} \quad . \tag{2.3}$$

In Equation (2.2) D denotes the electric displacement, d the piezoelectric coefficients (which are the same for direct and converse effect), σ mechanical stress, ε^{σ} dielectric permittivity at constant σ and E electric field. Equation (2.3) describes the converse effect where S is mechanical strain and s^{E} elastic compliance at constant electric field.

Due to symmetry considerations the third-rank tensor d_{ijk} comprises 18 independent components instead of 27, see for example Uchino[16]. For a more convenient treatment, Equations (2.2) and (2.3) can be re-written in the *matrix notation*

$$D_i = d_{ik}\,\sigma_k + \varepsilon^{\sigma}_{ij}\,E_j \tag{2.4}$$

$$S_k = s^{E}_{kl}\,\sigma_l + d_{ki}\,E_i \tag{2.5}$$

where $i, j \in \{1, 2, 3\}$ and $k, l \in \{1 \ldots 6\}$. In this notation index values k, l of $1, 2, 3$ represent normal strain or stress directions whereas $4, 5, 6$ denote shear strain or stress respectively, as illustrated in Fig. 2.1. Accordingly, the piezoelectric coefficient d is given by

$$d_{ik} = \left.\frac{\partial D_i}{\partial \sigma_k}\right|_{E=\text{const.}} = \left.\frac{\partial S_k}{\partial E_i}\right|_{\sigma=\text{const.}} \quad . \tag{2.6}$$

As an example, matrix-notation d_{33} corresponds to d_{333} in tensor-notation and represents the piezoelectric coefficient for a strain S_{33} along the x_3-direction due to an electric field E_3. In the AlN-based composites investigated in this work d_{33}

is the piezoelectric figure of merit for the magnetoelectric effect as is discussed in chapter 2.2.2.

10 out of the 20 non-centrosymmetric point groups possess a unique polar axis which leads to the property of spontaneous polarization along this axis in addition to the piezoelectric effect. This phenomenon is called the pyroelectric effect since the magnitude of spontaneous polarization varies with temperature. If additionally the direction of the spontaneous polarization can be changed by an external electric field the material is said to be ferroelectric.

2.1.2 Magnetostriction

A substance changes its dimensions in an external magnetic field as was first observed by Joule[17] in 1842. He reported that an iron rod increased its length l upon application of a magnetic field. This anisotropic change of dimensions

$$\lambda = \frac{\Delta l}{l} \tag{2.7}$$

is termed *Joule* or *anisotropic* magnetostriction. At very high fields also the effect of isotropic volume magnetostriction occurs. Since this so-called *forced* magnetostriction is in the order of $\Delta V/V = 10^{-10}$ per Oersted it is usually negligible. Thus, in the following *magnetostriction* refers to Joule magnetostriction. According to Equation (2.7) $\lambda > 0$ holds if a substance elongates in the direction of applied field and $\lambda < 0$ if a contraction along the field direction occurs. For the ferromagnetic $3d$ metals the effect is in the range of $\lambda = \pm 10^{-5}$–10^{-4} and can reach $\lambda = \pm 10^{-3}$ for $4f$ metals and alloys. Due to a transversal strain $\lambda_\perp = -\lambda/2$ occurring in addition to the longitudinal strain λ the specimen's volume stays constant during Joule magnetostriction. Figure 2.2 shows a typical magnetostriction curve versus applied field H during a full magnetization cycle. The value of the magnetostriction observed at saturation is denoted λ_S. It should be noted that λ_S is not necessarily a figure of merit for ME materials. The latter rather require a high $\partial\lambda/\partial H$ as will be discussed in chapter 2.2.2.

The magnetostrictive effect originates from spin-orbit coupling. The latter is a quantum-mechanical effect which couples the orientation of the magnetic moment m of an atom to it's surrounding electron cloud. This in turn results in a coupling of magnetic and elastic effects.[18] Upon changing the direction of magnetization via an applied magnetic field the minimum of a crystal's free energy might shift towards new interatomic equilibrium bond lengths. Figure 2.3 schematically illustrates the basic mechanism of magnetostriction in a ferromagnetic material. Above T_C there is no ferromagnetic order and the magnetic moments are aligned randomly as depicted in Fig. 2.3(a). Below T_C, Fig. 2.3(b), spontaneous magnetization occurs, leading to spontaneous magnetostriction. Subsequently, field-induced magnetostriction is observed upon application of a magnetic field as

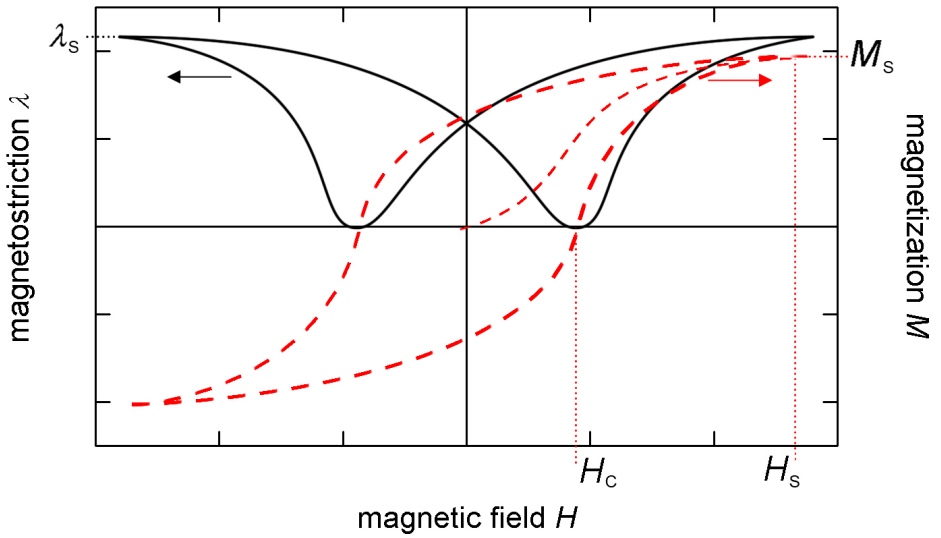

FIG. 2.2: Generic "butterfly"-curve of magnetostriction versus magnetic field H (black, straight) with saturation magnetostriction λ_S. Respective magnetization M of the specimen (dashed, red) with saturation magnetization M_S at saturation field H_S and coercive field H_C.

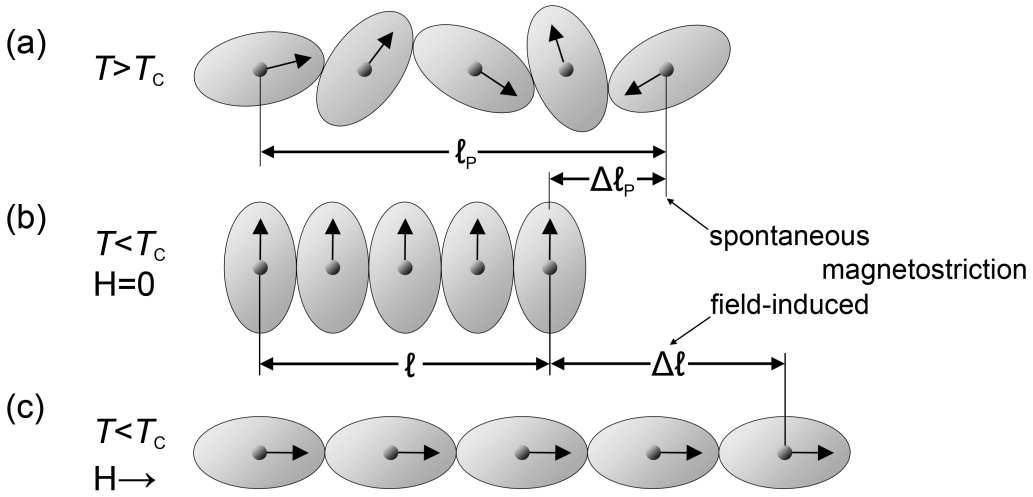

FIG. 2.3: Schematic of the origin of magnetostriction. Black dots represent nuclei, arrows depict magnetic moment and spheres illustrate electron clouds. (a) paramagnetic state above T_C. (b) spontaneous magnetization below T_C and (c) field-induced magnetostriction.

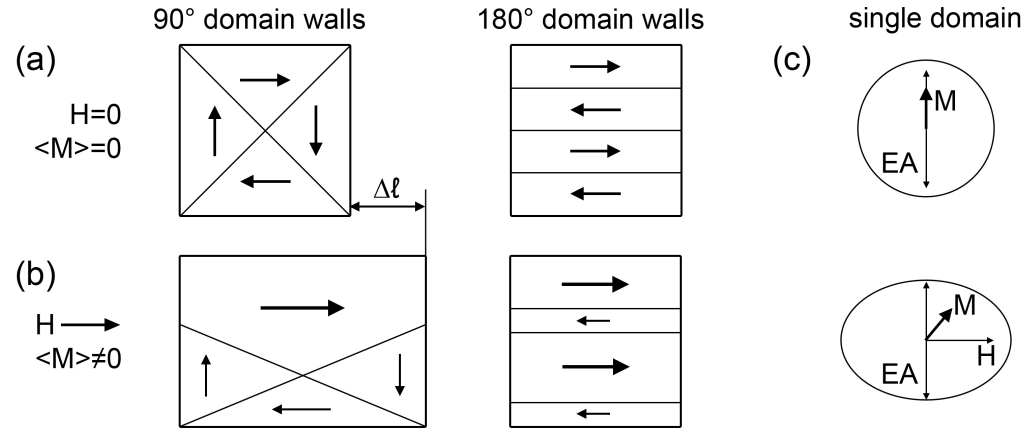

FIG. 2.4: Illustration of the influence of domain configuration on magnetostriction. (a) initially demagnetized states with exclusive 90° domain walls (left) and 180° domain walls (right), respectively. (b) magnetized states, exhibiting no magnetostriction in the 180° specimen and Δl in the 90° case. Magnetostriction due to domain rotation off the easy axis (EA) is depicted in (c) for a single domain particle.

depicted in Fig. 2.3(c). The *inverse* magnetostrictive effect describes the influence of an applied mechanical stress on the magnetization of a specimen. It is the origin of stress anisotropy. For small variations $\delta\sigma$ and δH linearized constitutive equations can be formulated for the magnetomechanical coupling

$$S_i = s_{ij}^H \, \sigma_j + p_{ki}^m \, H_k \tag{2.8}$$

$$B_m = p_{mj}^m \, \sigma_j + \mu_{mk}^\sigma \, H_k \tag{2.9}$$

analogous to Equations (2.4) and (2.5). s^H denotes elastic compliance at constant H, μ^σ magnetic permeability at constant σ and

$$p_{ki}^m = \left. \frac{\partial S_k}{\partial H_i} \right|_{\sigma=\text{const.}} = \frac{\partial \lambda_k}{\partial H_i} \tag{2.10}$$

the piezomagnetic coefficient.[19] It should be pointed out that strictly speaking piezomagnetism and magnetostriction are not synonymous. Piezomagnetism originates from an absence of crystal symmetry (like piezoelectricity) and, unlike magnetostriction, piezomagnetic strain changes sign upon reversal of the magnetic field direction. In addition, a non-zero net magnetization can be induced in a demagnetized piezomagnetic specimen in absence of an applied magnetic field by external stress alone. This is not true for magnetostriction.[20] However, it has become customary in literature to use the term *piezomagnetic* coefficient[9,19] instead of magnetostrictive coefficient for the quantity p^m defined in Equation (2.10) and the work at hand will follow this custom.

The influence of the initial state on the magnetostrictive effect is illustrated in Fig. 2.4. Two different initial domain configurations of demagnetized samples

are depicted in Fig. 2.4(a). The left one includes only 90° domain walls while the right one incorporates exclusively 180° domain walls. Upon magnetization only the 90° sample exhibits magnetostriction, as shown in Fig. 2.4(b). This is due to the fact that 90° domain wall motion aligns the magnetostrictive distortions along the field, leading to a net change in length Δl. On the other hand, the geometric distortion induced by magnetostriction is invariant to the reversal of magnetization direction. Thus 180° domain wall motion does not change the length l of a specimen. In addition to domain wall motion, magnetization rotation also leads to magnetostriction. In this case the orientation of M_S is rotated relatively to the crystal axes as illustrated in Fig. 2.4(c) for a single-domain particle (cf. chapter 2.1.3).

Since the actual value of λ depends on the initial state of the specimen, as depicted in Fig. 2.4, an ideal demagnetized state is defined for reference. This state is characterized by the occurrence of all possible types of domains in a specimen with each domain occupying the same volume. The saturation magnetostriction measured from such an ideal demagnetized state is referred to as $\lambda_{\mathrm{S,i}}$. If the magnetization and the measurement direction of the magnetostriction are parallel, one finds for hexagonal crystals with the easy axis parallel to the c-axis[20]

$$\lambda_{\mathrm{S,i}} = \lambda_\mathrm{A}\left[\left(1-\alpha_3^2\right)^2 - \left(1-\alpha_3^2\right)\alpha_3^2\right] + 4\lambda_\mathrm{D}\left(1-\alpha_3^2\right)\alpha_3^2 \tag{2.11}$$

where λ_A and λ_D are material constants, with $\lambda_A = -45 \times 10^{-6}$ and $\lambda_D = -100 \times 10^{-6}$ for Co.[21] α_3 denotes the direction cosine between the measurement direction and the basal plane of the hexagonal crystal. The absence of $\alpha_{1,2}$ reflects the uniaxial anisotropy along the c-axis.

In the case of a polycrystal the magnetostrictive contributions of the individual grains have to be averaged over their orientations. The resulting saturation magnetostriction of a polycrystalline material measured parallel to the magnetization is referred to as λ_P. Since preferred grain orientation influences λ_P, which is defined for random grain orientation, reported values may differ for a given material.[20]

The application of magnetostriction for the design of magnetoelectric composites is addressed in chapter 2.2.2.

2.1.3 Magnetism in Nanoparticles and Nanocomposites

Magnetic nanoparticles have been intensively studied in recent years since their unique physical properties can be potentially employed in a wide range of applications. Examples are biomedicine[22,23], nanoelectronics[24,25], catalysis[26,27] and data storage[28,29]. An important aspect of magnetic nanoparticles and particle assemblies is the size dependence of their magnetic properties which will be addressed in the following.

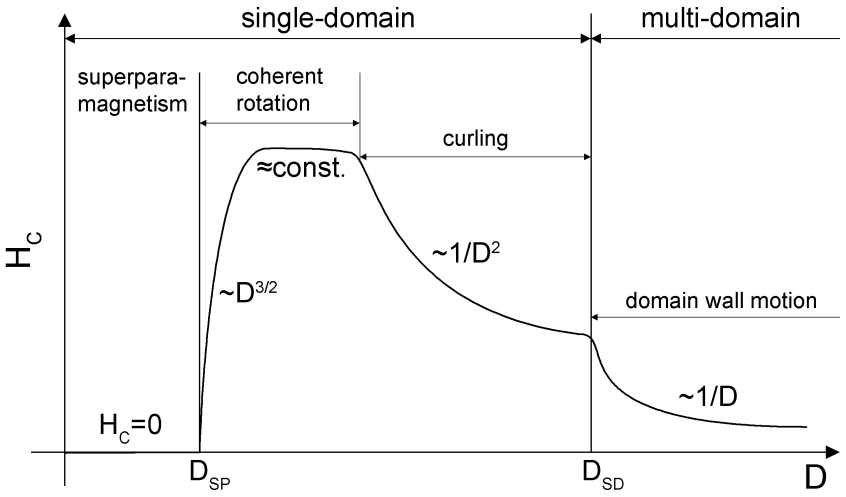

FIG. 2.5: (a) Generic plot of coercivity H_C versus diameter D for non-interacting particles. The exponents relate to increasing D.

First the influence of a magnetic particle's diameter D on the coercivity H_C is considered. The latter is an important property in many applications[29] and strongly depends on D as depicted in Fig. 2.5. A thorough discussion of $H_C(D)$ is given for example by Cullity and Graham[30] and by O'Handley[31]. Particles of diameter $D > D_{SD}$, which are large enough to contain domain walls, are called *multidomain* (MD) particles. A magnetization reversal occurs accordingly by domain wall motion. Since this process is easy compared to spin rotation, H_C is comparatively low. Large MD particles exhibits a lower H_C than smaller MD particles. This is because domain wall nucleation becomes easier in large particles due to the higher probability of surface defects which act as wall nucleation sites. In addition, the magnetization reversal of a large particle will influence an assembly's total magnetization more strongly than the reversal of a small particle.[30]

In particles of diameter $D < D_{SD}$ the reduction of magnetostatic energy due to a multidomain state is less than the energy necessary for domain wall formation. Thus, in such particles a singledomain (SD) state manifests. The magnetization reversal occurs accordingly by spin rotation. Since the rotation away from the easy axis has to overcome restoring forces resulting from shape, stress and crystal anisotropy, SD particles exhibit higher H_C than MD particles. For larger SD particles the spins rotate in the so-called curling mode which results in size-dependent H_C. At a certain SD particle size, the coherent rotation mode is energetically favorable, leading to almost constant H_C. Upon further decrease of D the superparamagnetic limit D_{SP} is approached. In this region H_C decreases since the thermal energy $k_B T$ starts sufficing to randomly reverse the magnetization direction of individual particles as will be discussed in the following.

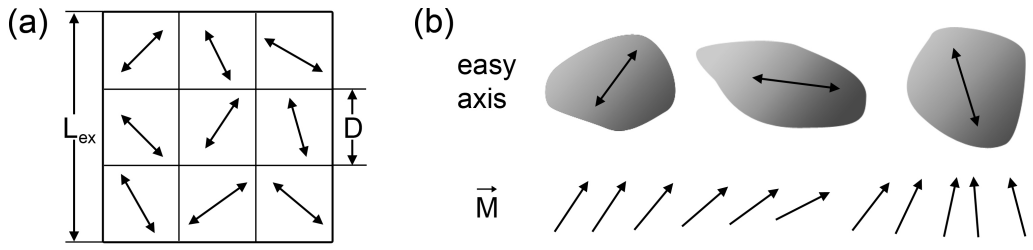

FIG. 2.6: (a) Illustration of random anisotropy model for interacting particles, after Herzer[32]. (b) Ferromagnetic interaction between particles with randomly oriented easy axis.

For uniaxial SD particles of volume V the energy barrier for reversing the magnetization direction is $\Delta E = KV$, where K is the anisotropy constant.[30] Consequently, $k_\mathrm{B}T > \Delta E$ will hold for $D \leq D_\mathrm{SP}$ and the magnetization direction of the particle will reverse randomly. In this case an ensemble of (non-interacting) particles with $D < D_\mathrm{SP}$ exhibits no remanent magnetization and $H_\mathrm{C} = 0$, cf. Fig. 2.5. On the other hand the comparatively large magnetic moments of the individual particles can be aligned by an external field, leading to a net magnetization orders of magnitude higher than that of paramagnetic materials. Magnetic particles below D_SP are thus called *superparamagnetic* (SP). The probability of magnetization reversal is given by the Boltzmann factor $\exp(-KV/k_\mathrm{B}T)$. Accordingly, the magnetization M of a magnetized ensemble of SP particles will decay following

$$-\frac{dM}{dt} = f_0\, M\, e^{-KV/k_\mathrm{B}T} = \frac{M}{\tau} \tag{2.12}$$

where $f_0 \approx 10^9\,\mathrm{s}^{-1}$ is a constant (the frequency factor). It follows that the relaxation time τ after which the remanent magnetization decreases to $1/e$ of its initial value is

$$\tau = (f_0\, e^{-KV/k_\mathrm{B}T})^{-1} \tag{2.13}$$

and varies rapidly with V and T, resulting in a reasonably well-defined onset of superparamagnetism. Commonly $\tau = 100\,\mathrm{s}$ is chosen to define the transition[30]. In this case Equation (2.13) yields for uniaxial particles

$$V_\mathrm{SP} = \frac{25\, k_\mathrm{B}\, T}{K} \quad \text{and} \quad T_\mathrm{B} = \frac{K\, V}{25\, k_\mathrm{B}} \tag{2.14}$$

where $V_\mathrm{SP} = V(D_\mathrm{SP})$ and T_B is the *blocking temperature*. Above T_B particles are superparamagnetic and they exhibit ferromagnetic hysteresis below T_B.

So far, non-interacting particles were considered. In nanostructured magnetic materials, however, the individual grains can ferromagnetically couple over an exchange length L_ex to each other.[33] The interaction of small particles with $D \leq L_\mathrm{ex}$ and randomly oriented crystal anisotropy K results in a reduced average

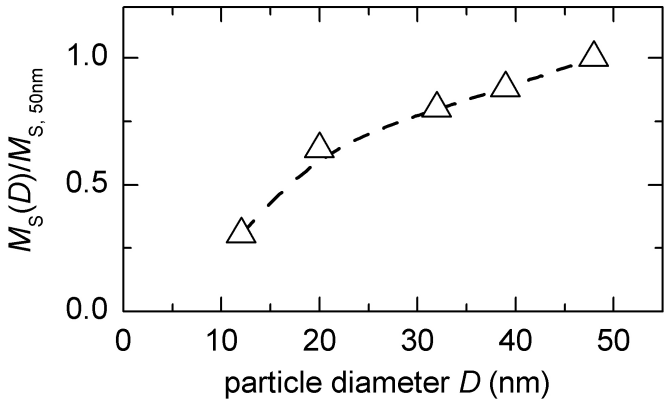

FIG. 2.7: Generic plot of saturation magnetization M_S versus diameter D based on data from Gong et al.[39].

anisotropy $\langle K \rangle = K/\sqrt{N}$ where $N = (L_{ex}/D)^3$ is the number of averaging particles. Within this random anisotropy model (RAM) Herzer[32] derived for small particles $D \leq D_{SD}$ that $H_C \propto D^6$ and accordingly for the permeability $\mu \propto D^{-6}$. Thus, depending on the particle diameter, increased H_C and decreased μ in magnetic nanocomposites pose potential challenges for the design of high-performance magnetoelectric nanocomposites (cf. chapter 2.2.2). However, acknowledging the existence of these obstacles, this work studies the fundamental feasibility to engineer ME 0-3 nanocomposites with metallic particles. In this context the fine adjustment of particle size and particle interaction in order to optimize H_C and μ[34] is of subordinate priority.

Apart from H_C, Berkowitz et al.[35] were the first to report a size dependency of the saturation magnetization M_S (at room-temperature). As was discussed above, when $KV \approx k_B T$ the magnetization direction of a single domain particle can be reversed randomly by thermal fluctuations. This increasing probability of magnetization fluctuation is accompanied by a reduction of the saturation magnetization. It is still under debate[36] whether the effect originates from surface effects like spin canting[37] or finite size effects[38]. Figure 2.7 illustrates the dependence of M_S (D) in nanoparticles as found in experimental[39] and theoretical[36] studies.

The size dependencies of H_C and M_S have to be taken into account for the interpretation of the magnetic data obtained from Co nanoparticles in chapters 4.2 and 5.

2.2 Applications of 0-3 Nanocomposites

The term *nanocomposite* refers to a vast class of materials which on the one hand consist of two or more phases and on the other hand include at least one geometrical dimension below 100 nm. Nanocomposites can be classified based on

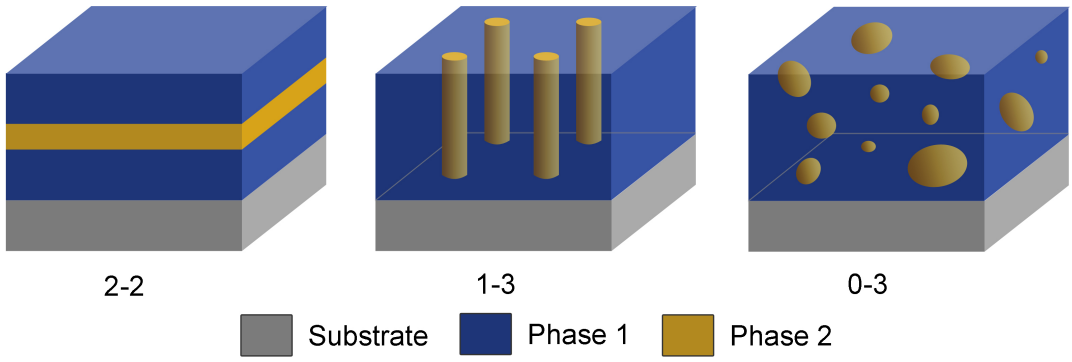

FIG. 2.8: Geometries of two-phase composites.

their geometry. Shown in Fig. 2.8 are laminar (2-2), pillar-like (1-3) and granular (0-3) composites, with the numbers in brackets denoting the dimensionality of the different phases.

Granular (0-3) nanocomposites with metallic nanoparticles embedded in a dielectric matrix are intensively studied due to the possibility to tailor their physical properties according to the technical requirements of a wide range of applications.[5] The latter range from perfect light absorbers[40] to antibacterial applications,[41] photocatalysis,[41] microelectronics[42] and data storage[29,43].

During the last decade, the magnetoelectric (ME) effect and the enhancement of dielectric permittivity ε_r have been intensively studied in 0-3 nanocomposites. While these effects are highly interesting for example for microelectronics[44] and magnetic sensing[9], they require advanced nanofabrication techniques for the precise tailoring of the composite structure, the filling factor ρ, and the particle size D. Making use of the deposition concept developed in the course of this work, 0-3 nanocomposites were deposited and investigated regarding their suitability for high-k and ME applications. The theoretical background of these two research areas is thus discussed in more detail.

2.2.1 High-k Materials

The electric permittivity ε_r of a dielectric can be enhanced by the presence of metallic particles as was already predicted in the 1970's.[45,46] Since then, intensive experimental research has been conducted in order to tailor such high-k materials.[a] For ceramic based 0-3 composites close to percolation $\varepsilon_r = 10^3$–10^5 have been reported[8] with an enhancement factor of up to approximately 100 between composite and pure matrix[8,47].

The physical reason for the increase of ε_r is due to the formation of microcapacitor networks.[46] The individual microcapacitors are formed by neighboring

[a] while the symbol "ε_r" is used in this work to denote the relative dielectric permittivity, the material class as such is commonly referred to as "high-k".[8,44]

particles which are separated by a layer of dielectric matrix. Near percolation, conducting channels stretch across the composite, blocked only by thin layers of dielectric. Each of these channels, connected in parallel, contributes a high capacitance.[46]

Accordingly, the volume filling factor ρ represents a central quantity for high-k composites with

$$\rho = \frac{V_{\text{fill}}}{V_{\text{fill}} + V_{\text{matrix}}} \tag{2.15}$$

where V_{fill} denotes the volume of the filling phase and V_{matrix} the matrix volume. Theory predicts ε_r of a 0-3 composite to diverge at a critical filling factor ρ_C, the *percolation threshold*, following

$$\varepsilon_r(\rho) = \varepsilon_r|_{\rho=0} \left| \frac{\rho_C - \rho}{\rho_C} \right|^{-q} \tag{2.16}$$

where $\varepsilon_r|_{\rho=0}$ is ε_r of the pure dielectric matrix and $q \approx 1$.[10,45,46] As was shown by Scher and Zallen[48] the percolation threshold for non-overlapping, monodisperse, spherical particles is reached at a critical volume fraction of $\rho_C \approx 0.16$,[49] which is known as the Sher-Zallen invariant[8].

Besides the real part of ε_r, however, dielectric losses have to be considered for most applications as a figure of merit for high-k materials as well. In an ideal, lossless dielectric, considered as a perfect capacitor, a voltage $U = U_0 \sin(\omega t)$ results in a current $I_{\text{C}} = C\dot{U} = C\omega U_0 \cos(\omega t)$ which is phase-shifted by 90° with respect to U. Accordingly, the time average dissipated power $\langle P \rangle$ is

$$\langle P \rangle = \frac{1}{T}\int_0^T I_{\text{C}} U \,\mathrm{d}t = \frac{1}{T}\int_0^T I_0 U_0 \cos(\omega t)\sin(\omega t)\mathrm{d}t = 0 \quad . \tag{2.17}$$

Losses thus result from a component I_{R} in phase with U. In this case the phase of U and I is not 90° and $I = I_0 \cos(\omega t - \delta)$ as shown in Fig. 2.9(a). This results in a net average dissipated power of

$$\langle P \rangle = \frac{1}{T}\int_0^T U_0 \sin(\omega t) I_0 \cos(\omega t - \delta)\mathrm{d}t = \frac{1}{2} U_0 I_0 \sin\delta \quad . \tag{2.18}$$

From $I_0 = I_{\text{C}}/\cos\delta$ and $I_{\text{C}} = \omega C U_0$ it follows that

$$\langle P \rangle = \frac{1}{2} U_0 I_{\text{C}} \tan\delta = \frac{1}{2} U_0^2 \omega C \tan\delta \quad . \tag{2.19}$$

The term $\tan\delta$ is called *dissipation factor* since it corresponds to the fraction of $U_0 I_{\text{C}}$ which is dissipated. In complex notation the fact that $I = I_0 e^{i\omega t}$ consists of a lossless capacitive part and a lossy part can be conveniently described by introduction of a complex permittivity $\hat{\varepsilon}_r = \varepsilon_r' - i\varepsilon_r''$. Considering a voltage

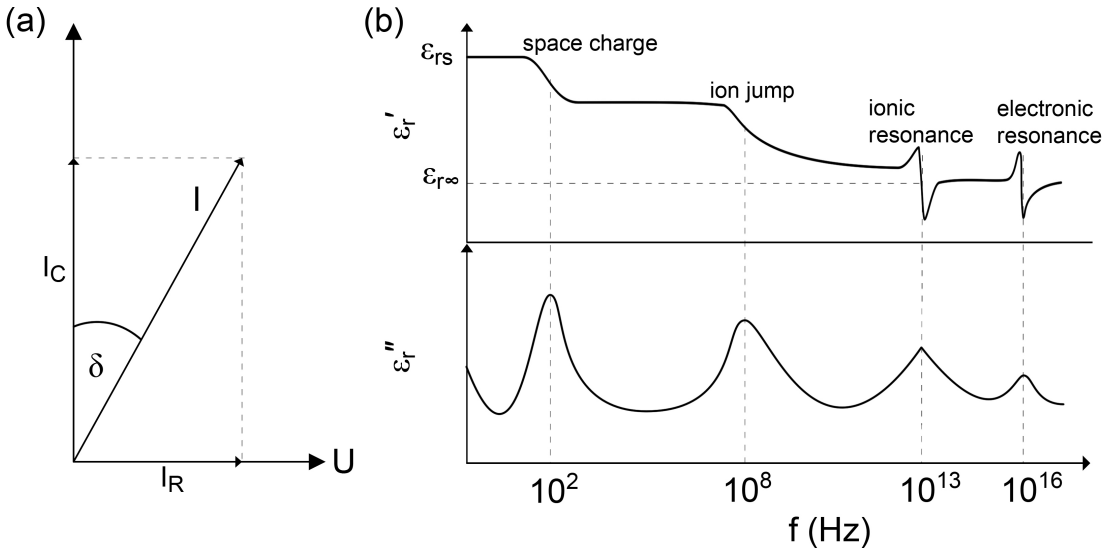

FIG. 2.9: (a) Phasor diagram of a non-ideal ("lossy") capacitor. (b) Frequency dispersion of ε_r' and ε_r'' for a solid with multiple relaxation and resonance modes, after Buchanan[50].

$U = U_0 e^{iwt}$ and a lossless (vacuum) capacitance C_0 it follows for I in a lossy dielectric

$$I = \hat{\varepsilon}_r C_0 \dot{U} = i\omega\hat{\varepsilon}_r C_0 U = i\underbrace{\omega\varepsilon_r' C_0 U}_{I_\mathrm{C}} + \underbrace{\omega\varepsilon_r'' C_0 U}_{I_\mathrm{R}} \quad . \tag{2.20}$$

The imaginary unit i in I_C of Equation (2.20) accounts for the phase of 90° between the lossless part of I and U. As previously discussed, $\tan\delta$ represents the fraction of dissipated power and it follows from Equation (2.20) that

$$\tan\delta = \frac{\varepsilon_r''}{\varepsilon_r'} \quad . \tag{2.21}$$

The dissipation factor $\tan\delta$ is a true material property. There are several loss mechanisms which occur in different frequency regimes depending on the underlying physical processes.[50] At high frequencies $f = 10^{10}$–10^{16} Hz resonance losses occur due to absorption by electronic or ionic vibrations close to their natural eigenfrequencies.

Relaxation losses can occur over a wide frequency range. They originate from dielectric relaxation due to comparatively slow polarization processes in the dielectric like dipolar orientation, ion jumps and electron hopping. According to Debye the diffusional polarization $P(t)$ approaches its final value P_0 following[50]

$$P(t) = P_0\left(1 - e^{-t/\tau}\right) \tag{2.22}$$

with the relaxation time τ. The solution of this equation yields the Debye-equations[50]

$$\varepsilon'_r = \varepsilon'_{r\infty} + \frac{\varepsilon'_{rs} - \varepsilon'_{r\infty}}{1 + \omega^2\tau^2} \tag{2.23}$$

$$\varepsilon''_r = \varepsilon'_{r\infty} + \frac{(\varepsilon'_{rs} - \varepsilon'_{r\infty})\,\omega\tau}{1 + \omega^2\tau^2} \tag{2.24}$$

where ε'_{rs} and $\varepsilon'_{r\infty}$ are the real parts of permittivity measured at static or low-frequency fields and at high frequencies, respectively. Losses during space charge polarization associated with ion migration and electrode contacts usually occur at low frequencies $f < 1\,\mathrm{kHz}$. However, space charge losses due to the presence of grain boundaries and inhomogeneous phases can occur at higher frequencies up to $f \approx 10^6\,\mathrm{Hz}$. A typical graph of $\varepsilon_r(f)$ for a solid with multiple relaxation and resonance modes is shown in Fig. 2.9(b). ε'_r decreases with increasing f as the different polarization modes are successively damped out. Peaks in ε''_r occur at the relaxation and resonance frequencies of the different loss mechanisms. Another contribution to loss is a non-zero dc conductivity, leading to leakage currents especially in the vicinity of the percolation threshold.[8]

High-k composites are discussed in literature for several potential applications like gate dielectrics[44] and supercapacitors[47]. Especially for charge storage the *dielectric strength* of a material is a crucial property. It is defined as the electric field E_b at which a dielectric fails and electric breakdown occurs. The latter commences when an electron avalanche is initiated due to collision ionization upon sufficient acceleration of conduction band electrons by an applied electric field.[51] E_b is not an exclusively intrinsic material property since it depends on external parameters like temperature, material microstructure and sample geometry, as well. With regard to percolative 0-3 composites Lustfeld et al.[52] found within a simplified 1D-model that E_b, and thus the maximal storable energy, scales with $1/\varepsilon_r$. Hence they doubt that 0-3 high-k materials are suitable for energy storage. However, 0-3 high-k materials remain interesting for other applications like FET gate dielectrics.[44] Although drastic increases of ε_r could be achieved in 0-3 composites, even at low $\tan\delta$, the technical applicability of such materials remains an issue. So far ceramic based high-k 0-3 composites have been prepared by sintering methods which require high temperatures.[47,53,54] Such temperatures can be incompatible with microtechnology processes. Another obstacle for technical applicability of percolative high-k composites is the strong variation of ε_r with particle shape, particle size[11,52] and filling factor ρ close to the percolation threshold ρ_C[10]. Accordingly, in order to obtain reproducible material properties, precise control of the filling factor and the particle shape is required.

2.2.2 Magnetoelectric Composites

The induction of an electric polarization P by an applied magnetic field H or the occurrence of a magnetization M upon application of an electric field E is called the *magnetoelectric* (ME) effect.[b] Some single-phase materials, like $BiFeO_3$, exhibit the ME effect and have been intensively studied in recent years.[56] However, this so-called *direct* ME effect is very small and observed only at low temperatures. Thus, the *indirect* ME effect, first proposed by van Suchtelen[57] in 1972, is more interesting from a technological point of view. In this scheme the ME effect is a product property resulting from a mechanical stress-strain coupling of a magnetostrictive and a piezoelectric phase, neither of which exhibit a ME effect on its own.

During the last decade, research of such ME composites has experienced a renaissance thanks to better theoretical understanding and advanced fabrication methods.[56,58] The indirect ME effect is several orders of magnitude higher than the direct effect[56] yielding immense potential for technical applications.[58,59] Common connectivity schemes of the piezoelectric and magnetostrictive phases are laminar (2-2), pillar-like (1-3) or granular (0-3). While laminar structures are easier to produce, thanks to the successive deposition of the different phases and geometrical suppression of leakage currents, theory predicts high ME effects in the more complicated granular type due to the much larger interface that can be created.[9,60]

Consider a two-phase ME composite consisting of a piezoelectric matrix in which magnetostrictive particles are embedded. In such a composite, a magnetic field H will lead via magnetostriction λ to a stress σ in the matrix, inducing an electric polarization P[9,57]

$$\alpha = \frac{\partial P}{\partial H} = \frac{\partial P}{\partial \sigma}\frac{\partial \sigma}{\partial \lambda}\frac{\partial \lambda}{\partial H} = \kappa\, d\, p^m \tag{2.25}$$

where α is the effective ME coefficient, κ accounts for the coupling between the composite phases, d and p^m are the piezoelectric and piezomagnetic coefficients, respectively. Depending on the geometry of the ME device, entries of the ME voltage coefficient tensor α_{ME} are often used as a figure of merit for ME materials[9,61]

$$\alpha_{\mathrm{ME}} = \frac{\partial E}{\partial H} = \frac{d_{ij}}{\varepsilon_0\, \varepsilon_{r,\,ij}}\kappa\, p^m_{kl} \tag{2.26}$$

where ε_r is the relative permittivity of the composite. For 0-3 composites numerical calculations predict a maximum α_{ME} at filling factors close to $\rho = 0.6$,[60,62] with ρ denoting the volume fraction of the composite occupied by the magnetostrictive phase, cf. Equation (2.15).

[b] parts of the ME theory section 2.2.2 are excerpted from Gojdka et al.[55]

Concerning the application of ME materials for example in sensors, not only α_{ME} has to be considered as a figure of merit. The dielectric loss factor $\tan\delta$ affects the crucial signal-to-noise ratio, as modeled for various laminar ME systems.[63,64] For example, Jahns et al.[61] found the noise voltage of a ME cantilever sensor to increase with $\tan\delta$ following

$$V_{noise} \propto \frac{1}{\sqrt{\tan\delta + 1/\tan\delta}} \tag{2.27}$$

due to thermal noise of the piezoelectric layer.

A wide range of ceramic granular ME bulk composites have been studied. However, these composites are usually either prepared by sintering,[65] often degrading the ME properties and making the process incompatible with common microtechnology, or adhesively bonded which gives rise to losses at the interface[59]. Nanogranular ME films, on the other hand, promise higher ME effects for several reasons. The high ratio of surface to volume of nanoparticles results in a large interface between the magnetostrictive and piezoelectric phases, leading to good connectivity. In addition, using advanced deposition methods, nanogranular films can be tailored on a nanoscopic scale, improving the interface of the phases and rendering the deposition process compatible with existing microtechnology. In order to improve the performance of nanogranular ME films, magnetostrictive metals and alloys appear promising, as some exhibit magnetostriction orders of magnitude higher than that of ferrites.[66,67] However, due to the reactivity of magnetostrictive metals and alloys, the preparation of such 0-3 nanocomposite films with magnetic metallic particles remains challenging. So far only Park et al.[68] reported on a magnetoelectric coefficient α_{ME} for a BTO/Co 0-3 film prepared by co-sputtering. However, the reported ME effect is very likely a measuring artifact as will be discussed in chapter 5.2.

2.3 Properties of Aluminum Nitride and Cobalt

Aluminum nitride (AlN) was chosen for the dielectric matrix and magnetic cobalt (Co) for the nanoparticulate phase. The physical properties of the materials will be discussed in the following, motivating why the system AlN/Co is suitable both for testing the new sputtering concept and as a proof-of-principle system for high-k and ME materials.

2.3.1 Aluminum Nitride

Physical Properties of Aluminum Nitride

Aluminum nitride (AlN) is a III-V nitride commonly crystallizing in the wurtzite structure, depicted in Fig. 2.10, which is the thermodynamically stable phase

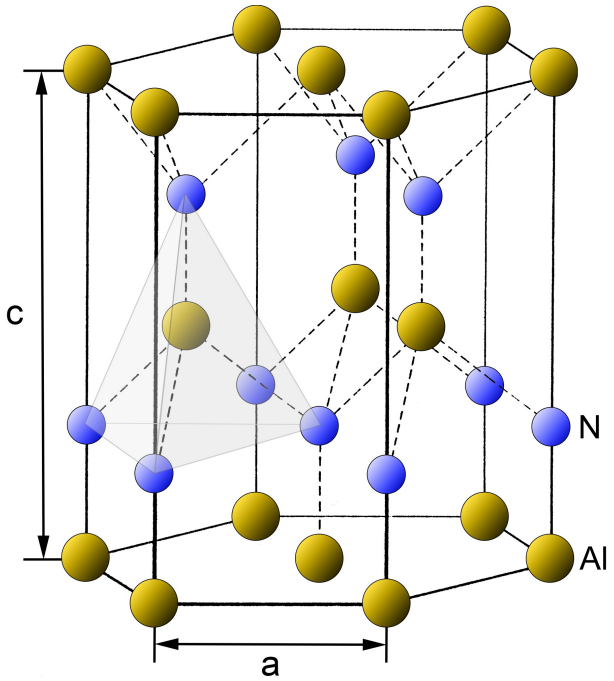

FIG. 2.10: (a) Wurtzite crystal structure of AlN with $a = 3.11\,\text{Å}$ and $c = 4.98\,\text{Å}$[69]. The shaded volume illustrates the tetrahedral coordination.

of AlN at ambient conditions.[69] Under special growth conditions other phases were reported.[70,71] The wurtzite structure consists of two interpenetrating hcp sublattices occupied by Al- and N-atoms, respectively, with each atom being coordinated tetrahedrally. Since the wurtzite structure (point group $6mm$) lacks centrosymmetry, piezoelectric polarization occurs along its c-axis. In addition, the latter represents a polar axis and as a consequence AlN is pyroelectric.[72]

AlN bulk ceramics do not exhibit net piezoelectric polarization since the crystal grains are randomly oriented. Thus, piezoelectricity is observed only in AlN single crystals and textured thin films, with typical $d_{33} = 3\text{–}5\,\text{pm/V}$[73–75] for highly c-axis oriented films. For the latter, the magnitude of the piezoelectric coefficient is directly correlated to the degree of c-axis orientation. Martin et al.[73] reported a linear relationship between d_{33} and XRD rocking curve width (cf. chapter 2.5.3). Extrapolating the decrease of d_{33} they found $d_{33} = 0$ for a rocking curve full width at half maximum of $\text{FWHM}_{\text{AlN(002)}} \approx 4°$ of the AlN(002) peak. In order to achieve c-axis oriented growth, several deposition parameters have to be taken into account. In former reports, various metals were investigated regarding their suitability as substrate for the c-axis oriented growth of AlN and excellent results were achieved with a seed layer of Pt(111) grown on Si.[76,77] A layer of SiO_2 acts as a diffusion barrier between Pt and Si. The lattice mismatch between Pt(111) and AlN(002) of approximately 11% did not influence the AlN texture negatively as Dubois and Muralt[77] pointed out. They concluded that

the matching symmetry of the Pt(111) plane (fcc) and the AlN(002) plane (hcp) in combination with the chemical inertness of Pt against N^+ are responsible for the highly oriented c-axis growth of AlN. The chemical stability of Pt offers the additional advantage that the substrate can be prepared and stored *ex-situ*. Accordingly, platinized Si will be used as substrate in the presented studies of AlN and AlN/Co composites. The development of a suitable AlN deposition process as part of the presented thesis will be discussed in chapter 4.1.

AlN is a ceramic dielectric with low loss $\tan\delta = O(10^{-3})$, typical ε_r = 8–11 and dielectric strength of E_b = 4–5.5 MV/cm.[73,74] With a wide bandgap of E_g = 6.2 eV, typical resistivity of AlN is in the range of $\rho = 10^{11}$–$10^{13}\,\Omega\,\mathrm{cm}$[78]. AlN decomposes at comparatively high temperatures $T \approx 2400\,^\circ\mathrm{C}$[79] and its standard heat of formation is $\Delta H_f^0 \approx -318\,\mathrm{kJ/mol}$[80]. Young's modulus of AlN is $E = 308\,\mathrm{GPa}$[81], making it a relatively stiff material.

2.3.2 Cobalt

Cobalt (Co) is a 3*d* transition metal with stable hcp-phase below 400 °C. Above that temperature a phase transition to fcc occurs and mixed phases of hcp and fcc are often observed due to the small energy difference between the two structures.[80] Co is ferromagnetic below the Curie-temperature of T_C = 1131 °C

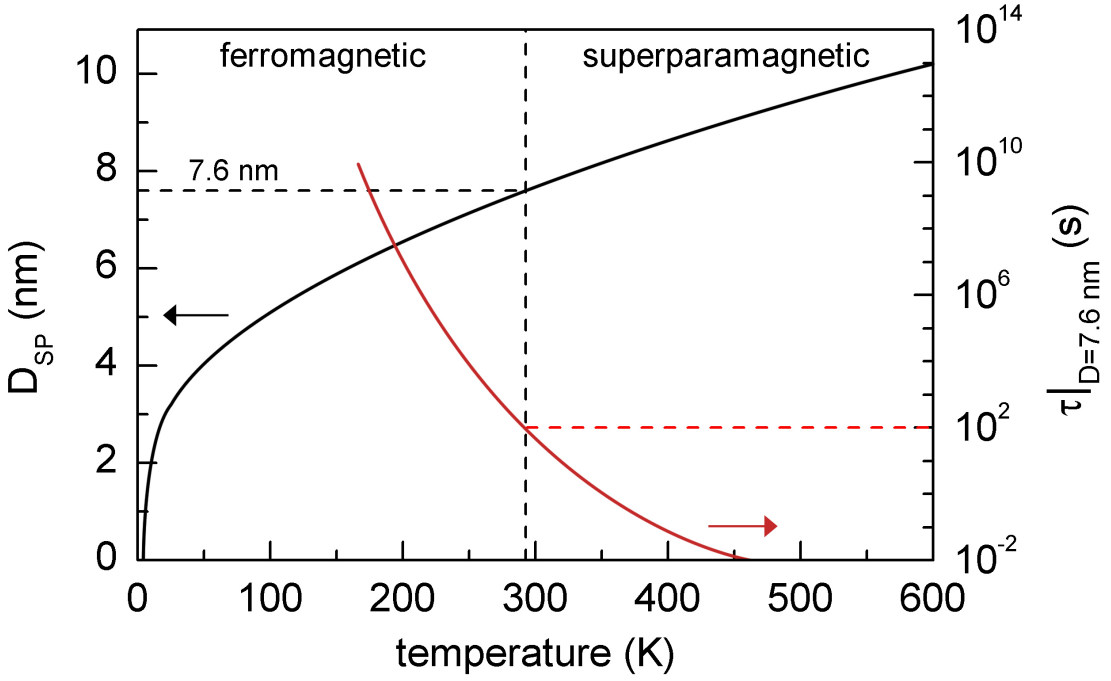

FIG. 2.11: Black line: critical diameter D_SP of Co particles with respect to temperature T. Red line: magnetism for D = 7.6 nm versus temperature T, with a blocking temperature of T_B = 293 K, after[82].

with a bulk saturation magnetization at room-temperature of $M_{S,bulk} = 1.42 \times 10^6$ A/m.[83] Its magnetic easy axis is oriented along the [1000]-direction (c-axis) and all directions within the (002) basal plane are equally hard, rendering the crystalline anisotropy of Co uniaxial. Among the $3d$ metals Co exhibits the highest saturation magnetostriction of $\lambda_P = -62 \times 10^{-6}$.[84] The size dependence of the magnetic properties for Co nanoparticles is illustrated in Fig. 2.11. Accordingly, the critical diameter for the transition from ferromagnetic to superparamagnetic behavior at room temperature is $D_{SP} \approx 7.6$ nm for individual particles.

The magnetic properties of Co can be influenced by the presence of CoO as the latter is antiferromagnetic below its Néel-temperature of $T_N = 270$ K.[85] Meiklejohn and Bean[86] were the first to report on magnetization loops which were shifted upon cooling by 1 kOe in Co-CoO core-shell nanoparticles due to antiferromagnetic coupling. Accordingly, attention will be paid to the presence of oxygen and its possible influence on the magnetization data in the experimental chapters 4.2 and 5.

2.3.3 AlN/Co as a demonstrator system

The deposition process of the desired AlN(002)/Co composites requires reactive pulsed dc sputtering at elevated substrate temperature for the matrix. The dielectric AlN deposit might be electrically floating, especially when the application of an rf-bias is desired, giving rise to a floating potential U_{fl} due to the magnetron plasma. Co is exposed to a reactive N^+ atmosphere during reactive deposition of AlN. Thus, pre-formation of Co nanoparticles in the cluster source appears advantageous to achieve magnetic properties. Due to its complexity, the tailoring of AlN(002)/Co composites appears suitable to test the developed deposition concept.

The high dielectric breakdown strength and low $\tan\delta$ of AlN are both advantageous for the matrix component of percolative high-k material. Regarding the metallic phase, percolative high-k materials have been successfully prepared with various metals[8,10,54,87] and composites with Ni yielded excellent results[47,88]. Thus, one can expect Co to perform similarly, due to similar material properties like electrical conductivity $\sigma_{Co} = 1.7 \times 10^5\,(\Omega\text{cm})^{-1}$ and $\sigma_{Ni} = 1.4 \times 10^5\,(\Omega\text{cm})^{-1}$.[89] In addition, Nan et al.[8] summarized existing reports by pointing out that the choice of metal does obviously not influence the properties of high-k composites. From Equation (2.16) and $\varepsilon_r^m \approx 10$ follows that AlN based percolative composites will not reach the high absolute values of $\varepsilon_r = 10^3 - 10^5$ reported in previous studies.[8] However, while microelectronics utilize SiO_2 with $\varepsilon_r = 3.9$ and metal oxides with $\varepsilon_r \approx 10$–20, further downscaling will require an increase of ε_r by preparation routes compatible with process limitations.[44] Thus, already a moderate relative increase of ε_r is of technological interest[90] and, depending on the application, extremely high absolute values of ε_r are not necessarily a figure of merit[52] (cf. chapter 2.2.1). Apart from the

technological point of view, the AlN/Co system can be used to study the feasibility of a magnetron based PVD approach to the fabrication of percolative high-k materials in contrast to existing sintering techniques.

As in the case of high-k materials, the low $\tan\delta$ of AlN is advantageous for ME materials, too. The ratio $\varepsilon_r/d_{33} \approx 0.5$ V/pm, cf. Equation (2.26), of AlN is even better than that of ferroelectric PZT ($\varepsilon_r/d_{33} \approx 0.35$ V/pm)[75]. In addition, considering environmental aspects and legal regulations, AlN would be a lead free alternative to commonly used PZT.[91] The comparatively high Young's modulus of AlN must be considered detrimental for the ME effect, but not crucial for a proof-of-principle investigation of the fundamental suitability of 0-3 nanocomposites for ME materials. While ferroelectric perovskites offer the possibility of electrical poling after deposition, they do not appear to be compatible with a metallic magnetostrictive phase since oxygen admixture and high temperatures are required for crystalline growth.[92] Thus, oxygen-free low-temperature sputter deposition of highly-oriented AlN appears advantageous compared to other piezoelectric materials like ZnO and perovskites. Even if Co_xN_y is formed during co-deposition, thermal decomposition by tempering in vacuum is possible. Suzuki et al.[93] found all Co_xN_y to decompose to Co at 300 °C and Maya et al.[43] demonstrated the pyrolysis of CoN to Co in AlN/Co composites at a moderate temperature of $T = 400°$ C. In combination with the thermal stability of AlN, this enables recovery of the magnetic properties by selective thermal decomposition if CoN should be formed during deposition. On the other hand, perovskites are well-known for becoming conductive upon annealing in vacuum due to the creation of oxygen vacancies.[94,95] Using Co as magnetostrictive phase no stoichiometric concerns have to be taken into account. While on a first glance highly magnetostrictive materials like TbFe or amorphous FeCoSiB might appear more attractive for high-performance ME composites, the complexity of the deposition would increase considerably due to the high reactivity of the involved elements and stoichiometric concerns. Thus, Co represents a robust choice for the magnetostrictive phase of a proof-of-principle system.

In summary, the respective physical properties and deposition conditions render AlN/Co a suitable system for the proof-of-principle investigations of the presented work. To increase the performance after the fundamental questions have been addressed, more complex materials might be employed in prospective studies as will be discussed in the conclusions of part I (chapter 5.2.3).

2.4 Physical Vapor Deposition

Numerous techniques have been developed for the deposition of thin films including wet chemistry, chemical vapor deposition and physical vapor deposition (PVD). In the latter the atoms of a solid material source are transferred into the gas phase either by evaporation or atomic collision impact. Subsequently the

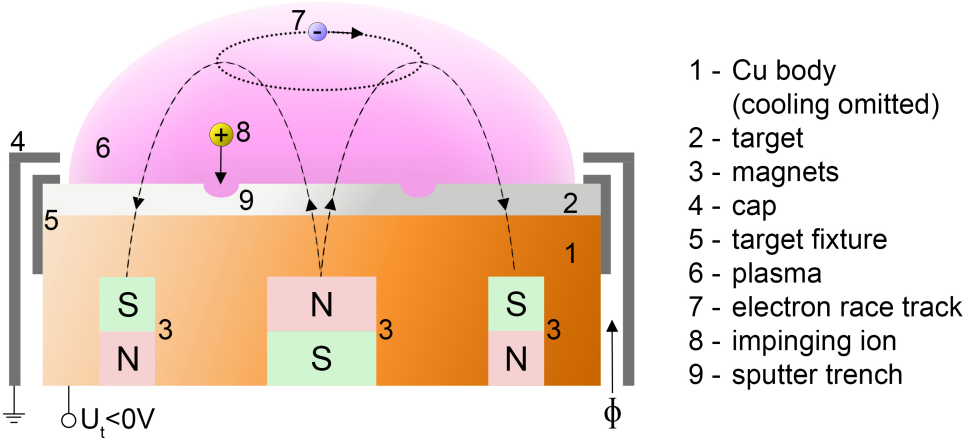

FIG. 2.12: Principle of a planar balanced magnetron. For the sake of clarity only the $\mathbf{E} \times \mathbf{B}$-drift component of the electron movement is depicted.

gaseous atoms are transported through a vacuum environment to the substrate. With PVD processes a wide range of materials can be deposited in a clean and dry environment. Typical PVD techniques include thermal evaporation, pulsed laser deposition and magnetron sputtering.

2.4.1 Magnetron Sputtering

Magnetron sputtering is a well-established PVD technique which is readily used today both in science and industrial production. Since the basic technique is discussed in great depth in literature[96–99], it will be introduced only briefly in the following. Already in 1852 Grove[100] observed the deposition of a metal film opposite the cathode of a dc glow discharge. However, the simple glow discharge deposition suffered from low deposition rates and restriction to metallic materials. This changed with the development of advanced magnetron deposition devices in the 1960's and 1970's.[2,101,102] Magnetron sputtering allows for high-rate deposition of a multitude of different materials like metals, alloys, ceramics and polymers. Figure 2.12 depicts the common planar balanced magnetron arrangement. Permanent magnets create an arc-shaped magnetic field $\mathbf{B}$ above a disc of source material (the *target*). Upon application of a negative voltage $U_t = 10^2$–10^3 V to the target, a glow discharge is initiated in the introduced process gas. The presence of the magnetic and electric fields force the free electrons to gyrate in a closed loop (the *race track*) above the target due to the $\mathbf{E} \times \mathbf{B}$-drift following

$$m_e \, \mathbf{a} = -q \, (\mathbf{E} + \mathbf{v} \times \mathbf{B}) \quad . \tag{2.28}$$

This trapping increases the ionization efficiency of the electrons in the plasma, allowing operation of the magnetron in a lower pressure range than for a simple

glow discharge arrangement. Subsequently, the vaporization of the target occurs due to kinetic energy transfer upon the impact of the ions which are accelerated towards the target by the applied target bias U_t. Target erosion is highest in the area below the electron race track since most ionization of the process gas occurs in this region.

A physical aspect closely connected to plasma based deposition processes is the charging of surfaces which are exposed to the plasma. In typical glow discharges the thermal velocity of electrons usually exceeds that of the ions by a factor of 10^3.[103] As a consequence of the high electron mobility, the plasma (bulk) is always more positive than adjacent surfaces. The minimum positive potential is the plasma potential ϕ_{P_0} with respect to ground.[104] An electrically floating surface immersed in plasma charges negatively, with respect to ground potential, to a floating potential $\phi_{\mathrm{fl},0} < \phi_{\mathrm{P},0}$. In steady-state the potential drop $U_\mathrm{fl} = \phi_{\mathrm{fl},0} - \phi_{\mathrm{P},0}$ between plasma bulk and floating surface leads to a balance of electron and ion currents $I_\mathrm{e}(U_\mathrm{fl}) + I_\mathrm{i}(U_\mathrm{fl}) = 0$ towards the surface. The resulting potential drop is given by[104]

$$U_\mathrm{fl} = \phi_{\mathrm{fl},0} - \phi_{\mathrm{P},0} = -\frac{T_e}{e_0} \ln\left(\frac{m_i}{2.3\, m_e}\right) \tag{2.29}$$

where T_e is the electron temperature in eV, e_0 elementary charge and m_i and m_e are ion and electron mass, respectively. Equation (2.29) yields for Ar $U_\mathrm{fl} \approx -10\, T_e$ and with $T_e = O(1\,\mathrm{eV})$ it follows that surfaces immersed in Ar plasma are bombarded by ions with $E_\mathrm{kin} = O(10\,\mathrm{eV})$. This bombardment results in surface and subsurface modifications which essentially influence the growth of films.[105–107]

Following the above line of reasoning, particles in a plasma charge, too, to floating potential[108,109] ϕ_fl as has already been modeled in 1926 by Mott-Smith and Langmuir[110]. This effect is of fundamental importance for various fields of research like astrophysics[111] and industrial applications[112,113], for example etching or PVD processes. Thus, the charging of particles has been intensively studied in the emerging field of so-called *dusty plasmas*[114] and has to be considered in the presented work for the development of a co-deposition concept with a cluster source (cf. chapter 5).

Reactive Sputtering

Inert gas like Ar is used for sputter deposition of films with a chemical composition corresponding to the target material. However, the chemical composition of a deposit can be modified intentionally by introducing a reactive process gas. The technique of *reactive sputtering* is most commonly employed to deposit compounds from a metallic target, offering advantages compared to the direct sputtering of the respective compound target. A metallic target allows the application of dc power and yields higher deposition rates than a ceramic target. In addition,

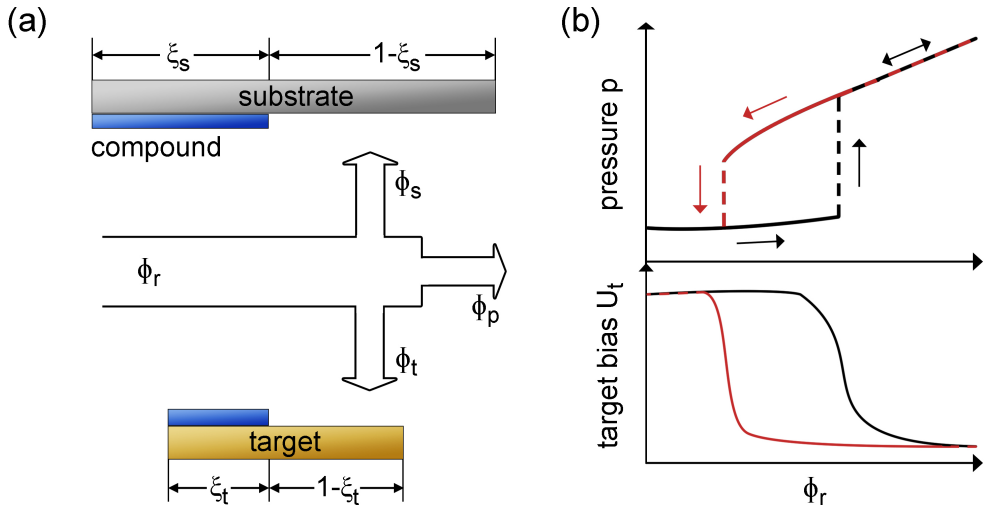

FIG. 2.13: (a) Flows of reactive gas during sputtering. (b) System pressure p (top) and target bias U_t (bottom) versus reactive gas flow Φ_r. Black: increasing Φ_r, red: decreasing Φ_r.

the stoichiometry of the deposit can be influenced via the partial pressure of the reactive gas. However, reactive sputtering can be complex and some theoretical considerations have to be taken into account in order control the process.[115]

The reactive gas not only interacts with the material deposited on the substrate but with the target surface as well, having important consequences for the sputtering process. An according model was proposed by Berg et al.[3],[116]. Various textbooks[117] provide an in-depth discussion of reactive sputtering.

As depicted in Fig. 2.13(a), a flow Φ_r of reactive process gas introduced into the system can be divided into the consumption by the substrate Φ_s and the target Φ_t, respectively, and the outgoing flow Φ_p generated by the pumping system. As a consequence, a fraction ξ_t of the target surface A_t is covered by compound while the rest $1 - \xi_t$ remains metallic. ξ_t depends obviously on the available amount of reactive gas. Accordingly, the evolution of system pressure p with respect to the reactive process gas flow Φ_r is depicted in Fig. 2.13(b). Starting at $\Phi_r = 0$ the target operates in metallic mode, until a critical point $\Phi_{r,c}$ is reached. Up to $\Phi_{r,c}$ the reactive gas is consumed by the formation of compound material and as a consequence p does not increase significantly. The target can operate in metallic mode while stoichiometric compound is formed at the substrate since the transferred source atoms cover a wider substrate area A_s than they did in the target erosion track. At $\Phi_{r,c}$, however, $\xi_t = 1$ and the target switches from metallic to ceramic mode. Consequently the sputtering rate drops which in turn results in a slower formation of compound. Thus, the system pressure jumps at $\Phi_{r,c}$ and afterwards increases linearly (assuming constant pumping speed). The transition back to metallic mode upon decreasing Φ_r occurs at $\Phi_{r,m} < \Phi_{r,c}$ due to the lower reactive gas consumption by compound formation in ceramic mode.

The sputter characteristic of a target crucially depends on whether the target is in metallic or ceramic mode as shown in Fig. 2.13(b). Since the sputtering yield for metals is generally several times higher than for oxides the target erosion rate r_t drops drastically when the target switches to ceramic mode. This transition is accompanied by a considerable change of the target bias voltage

$$U_\mathrm{t} = \frac{E_0}{\gamma\,\varepsilon_i\,\varepsilon_e\,\varsigma\,n} \tag{2.30}$$

where E_0 is the effective ionization energy, ε_i the ion collection efficiency, ε_e the fraction of the theoretical number of ions each electron generates, ς the effective gas interaction probability and n a multiplication factor accounting for ionization by electrons which are generated in the discharge sheath.[118] The decrease of U_t upon transition to ceramic mode occurs as the secondary electron emission coefficient γ is higher for compounds than for their metallic counterparts.[119] Note that not only the target state influences U_t but according to Equation (2.30) also the gas composition, for example due to species dependent ionization energy E_0. In addition γ is found to actually decrease upon oxidation of certain metals.[118] However, in the case of Al, relevant to the presented work, γ increases upon formation of AlN on the target surface.[118] Furthermore it should be mentioned for the sake of clarity that, although U_t is negative, it is usually referred to in positive values. Thus, the behavior of U_t illustrated in Fig. 2.13(b) is called a *decrease* since the absolute value of U_t decreases, although the value mathematically increases as the bias voltage is negative.

The hysteresis in both r_t and U_t is a direct consequence of the preceding discussion of $p\,(\Phi_\mathrm{r})$. However, depending on the experimental conditions like pumping speed[120] or target area[121], hysteresis can be differently pronounced or even not present at all.

Pulsed DC Sputtering

Pulsed dc sputtering is a further modification of basic dc sputtering. It is commonly applied in order to stabilize magnetron operation by prevention of arcing during reactive sputtering. The technique is employed in industrial deposition processes of dielectric materials and is still subject of fundamental research. Accordingly, there are various review articles emphasizing applied[4,99,122] and fundamental[123,124] aspects of pulsed dc sputtering. As the name suggests, dc power is not supplied continuously to the magnetron but the target bias U_t is applied in pulses. The operation is termed *unipolar* if $U_\mathrm{t} \leq 0\,\forall t$, as illustrated in Fig. 2.14(a), and *bipolar* if additional positive pulses are applied.[99] In real experimental or industrial setups, the pulses are usually not square but might exhibit considerable overshoots. This behavior can be exploited to influence the plasma properties and in turn the deposition process.[123] The two parameters introduced by pulsed dc sputtering are the pulsing frequency f_dc and the duty

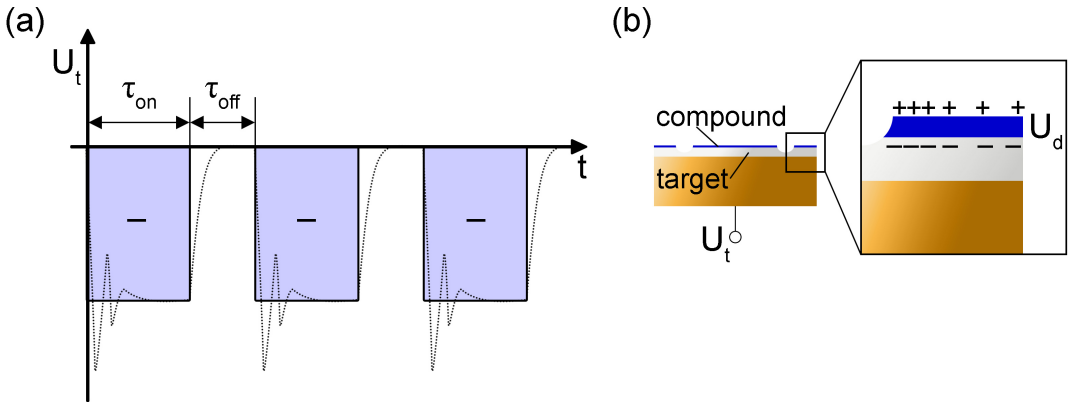

FIG. 2.14: (a) Illustration of target bias U_t during unipolar pulsed dc sputtering. If $U_\mathrm{t} > 0$ during τ_off the pulsing is bipolar. The dotted line depicts commonly observed overshoots. (b) Schematic charge accumulation on a metallic target during reactive sputtering.

cycle. The latter is defined as $\tau_\mathrm{on}/(\tau_\mathrm{on} + \tau_\mathrm{off})$, that is the fraction of on-time per cycle to total cycle length.

During reactive sputtering part of a metallic target's surface is covered by compound material as was explained in the previous chapter. These insulating areas accumulate a positive charge Q since ions impinge on the target during sputtering. The accumulated charge results in a voltage U_d between dielectric surface and metallic target as depicted in Fig. 2.14(b). For continuous dc operation and a sufficiently high breakdown strength of the compound layer the latter would be charged until eventually the target bias voltage $U_\mathrm{d} = U_\mathrm{t}$ is reached. At that point the ions would be no longer accelerated towards the target. However, in a dielectric layer of a few nm on the target surface[116], electrical breakdown will occur since typical breakdown fields are in the range of $E_\mathrm{b} = 1$–$10\,\mathrm{MV/cm}$. In this case so-called *arcing* happens, especially in compound-covered target regions close to the race track.[125] As a consequence magnetron operation becomes instable since the power supply is forced to disrupt the discharge. In addition, droplets can be ejected from the target surface during arcing, which degrade the quality of the deposit.[4]

By means of pulsed dc power such arcing can be prevented since during $U_\mathrm{t} \geq 0$ free electrons from the plasma can reach the target surface and neutralize the accumulated positive charges Q. Typical pulsing frequencies are $f_\mathrm{dc} = 10$–$350\,\mathrm{kHz}$.[123] The necessity of f_dc to be in this range can be derived in first-order approximation by considering the voltage U_d across a dielectric layer with thickness d on the target in a plate capacitor model:[4,126]

$$U_\mathrm{d} = \frac{Q}{C} = \frac{Q\,d}{\varepsilon_r\,\varepsilon_0\,A} \tag{2.31}$$

where C and A are the capacitance and the area, respectively, of the capacitor.

Furthermore $Q = J\,A\,t$ with J being the ion current density during sputtering. Thus, an electric field

$$E_\mathrm{d} = \frac{U_\mathrm{d}}{d} = \frac{J}{\varepsilon_r\,\varepsilon_0}\,t \tag{2.32}$$

builds up. With average values of AlN, $\varepsilon_r = 10$ and $E_\mathrm{b} = 5\,\mathrm{MV/cm}$ (cf. chapter 2.3.1), and a typical current density of $J = 20\,\mathrm{mA/cm^2}$ the breakdown field is reached after $t_\mathrm{b} \approx 2 \times 10^{-4}\,\mathrm{s}$. Thus, charging must be interrupted at $f_\mathrm{dc} \geq 1/t_\mathrm{b} = 5\,\mathrm{kHz}$ to prevent arching. While this is an approximate lower boundary (for AlN), typically used values are in the range of $f_\mathrm{dc} = 10$–$100\,\mathrm{kHz}$.[122]

Besides the prevention of arcs during reactive sputtering, pulsed dc power can also improve the physical properties of a deposit.[127–129] Fundamental research has been conducted in order to link the observed modifications of the deposits to the underlying plasma physics.[123,124,130] It was found that the energy flux towards the substrate was influenced by f_dc and duty cycle as a consequence of changes in the plasma density and ion energies. Accordingly, the pulsing parameters can be used to tune the properties of a deposit since film growth is crucially influenced by energy flux onto the substrate.[105–107]

2.4.2 Gas aggregation cluster source

The unique physical properties of nanoparticles are of great interest for fundamental research and a wide range of applications. Thus, different techniques have been demonstrated to produce nanoparticles with specific morphology and chemical composition. Among them, gas aggregation cluster sources (GAS) have become a versatile tool for the creation of nanoparticles in the gas phase.[131] Nanoparticles are generated in a GAS by condensation of supersaturated metal vapor inside a vessel. Inert gas acts as a thermal bath which promotes the condensation of clusters. There are various GAS variants which mainly differ in the kind of vapor source. The first GAS was proposed in 1980 and included a crucible in which metal was thermally evaporated.[6]

In 1992 Haberland et al.[132] presented a GAS based on magnetron sputtering. The size of the particles could be tuned between 10^1–10^6 atoms. In addition a high fraction of the particles left the source electrically charged, enabling the possibility to accelerate them towards the substrate.[7] Since magnetron sputtering provides an effective[133] and versatile route for the creation of metal vapor, Haberland-type GAS have been used to produce nanoparticles from many metals like Au, Ag, Cu[134], Ti[135], Co[136] and many others[131,133,137,138]. The comparatively high kinetic energy in the order of 10 eV of metal atoms in a magnetron discharge is advantageous in a GAS since the probability of re-attachment to the cathode is reduced.[139] Upon leaving the cathode, the sputtered atoms are thermalized due to collisions with inert gas atoms. Considering a typical kinetic energy $E \approx 10\,\mathrm{eV}$ of a sputtered atom[140] and a mass comparable to the inert species, the metal

atoms are thermalized after a distance of $l \approx 1\,\mathrm{cm}$.[141] Subsequent nucleation and growth of clusters can be separated into three stages[142–144] by the model of liquid droplets in a supersaturated vapor[133,142,145]. First, dimers form in a three-body collision between two individual metal atoms M and an inert atom I

$$2\mathrm{M} + \mathrm{I} \rightarrow \mathrm{M}_2 + \mathrm{I} \quad . \tag{2.33}$$

The inert atom on the one hand enables energy and momentum conservation and on the other hand stabilizes the formed dimer.[144,146] The generation of dimers poses the bottleneck of particle formation since the rate of this process is lower than the subsequent growth of the clusters by two-body collisions.[143,147] Subsequent growth proceeds either by addition of single atoms to the clusters or by coagulation.[146] In the aggregation region close to the cathode the number density of free metal atoms n_f is higher than the number density of atoms bound in clusters, $n_f \gg n_b$.[141] Under these conditions growth proceeds by attachment of single atoms to clusters

$$\mathrm{M_n} + \mathrm{M} \rightarrow \mathrm{M_{n+1}} \quad . \tag{2.34}$$

Upon leaving the aggregation region, $n_f \ll n_b$ holds and cluster coagulation governs the third stage of particle growth

$$\mathrm{M_n} + \mathrm{M_m} \rightarrow \mathrm{M_{n+m}} \quad . \tag{2.35}$$

Within the aggregation region, the coagulated clusters can rearrange in order to minimize their surface energy. The necessary surface mobility results from the small cluster size and the heating of the inert buffer gas during the sputtering operation.[148] The inert buffer gas not only promotes the vapor condensation, but the escaping gas flow also transports the formed particles out of the GAS.[131] The thermalized particles are carried through the nozzle, forming a cluster beam. Having left the GAS the nanoparticles move with a typical speed of $30 - 200\,\mathrm{m/s}$.[143,149] Considering the impact of a Co nanoparticle with a diameter of $D = 7\,\mathrm{nm}$ at a speed of $200\,\mathrm{m/s}$[149] each atom has a kinetic energy of $E_\mathrm{a} = 12\,\mathrm{meV}$. When the kinetic energy per atom is lower than the binding energy of the cluster constituents, which is usually below 1 eV per atom, the cluster remains intact upon impact on the substrate.[144] This deposition mode, which is typical for GAS-produced clusters, is called *soft landing*. Highly compact films can be produced by acceleration and subsequent fragmentation of the particles on the deposit.[7,144] However, this work aims at the embedding of metallic nanoparticles in a matrix. Thus, in the framework of this thesis, soft landing of the magnetic clusters is desired.

The operation of a magnetron in a GAS arrangement can be instable due to electric breakdown. As Smirnov[148] estimated for Ti, Cu and Ag, magnetron discharge parameters of $P = 100\,\mathrm{W}$ and $p = 100\,\mathrm{Pa}$ provide a suitable working point

for a GAS since cluster evaporation due to buffer gas heating is not dominant under such conditions.[148] Magnetrons, however, are usually designed for operation at $p \leq 1\,\mathrm{Pa}$, and electrical breakdown can be an issue in Haberland-type GAS.[150] The voltage U_b leading to breakdown at pressure p and electrode separation d can be estimated by Paschen's law which was derived by Townsend[151]

$$U_\mathrm{b} = \frac{p\,d}{\ln\left(K\,p\,d\right) - \ln\left(\ln\left(1+\gamma^{-1}\right)\right)} \frac{K\,E_\mathrm{I}}{e_0} \tag{2.36}$$

where γ is the secondary ionization coefficient, $K = k_\mathrm{B}\,T/\sigma$ accounting for the ionization cross section, E_I ionization energy and e_0 elementary charge. In the magnetron employed in this work d can be as high as $d = 3\,\mathrm{mm}$ and stable operation of the GAS is desired up to $p_\mathrm{GAS} \approx 200\,\mathrm{Pa}$ resulting in $U_\mathrm{b} \approx 250\,\mathrm{V}$. This potential experimental obstacle will be addressed in chapter 3.

2.5 Characterization Techniques

The characterization techniques employed in the course of this work will be introduced in the following. Since they are well-established standard techniques the discussion represents only a brief overview addressing important key points. For further details the reader might refer to the cited literature. Apart from the basic working principles, practical aspects of the employed techniques for the characterization of AlN/Co 0-3 nanocomposites are emphasized.

2.5.1 Scanning Electron Microscopy / Energy Dispersive X-ray Spectroscopy

In scanning electron microscopy (SEM) free electrons are generated for example thermionically or by field emission and are subsequently accelerated towards the sample. Focusing of the beam generates an electron probe which allows for 1–10 nm imaging resolution. By scanning the beam over the surface an image is generated. In contrast to transmission electron microscopy (TEM), SEM can be applied to bulk samples since no transmission of the electrons through the sample is required. The textbook by Reimer[152] gives an in-depth discussion of the technique.

Various elastic and inelastic interactions between electrons and sample can be exploited for imaging as well as for structural and chemical analysis. Within the interaction volume, the primary electron beam is completely diffused due to multiple scattering and gradual energy loss of the electrons. Depending on the interaction, secondary-, backscattered- and Auger-electrons can be detected above the sample as depicted in Fig. 2.15. Commonly, secondary electrons with $E_\mathrm{SE} < 50\,\mathrm{eV}$ are used for imaging as they can be easily collected. They are generated by inelastic collisions either of primary or backscattered electrons. For

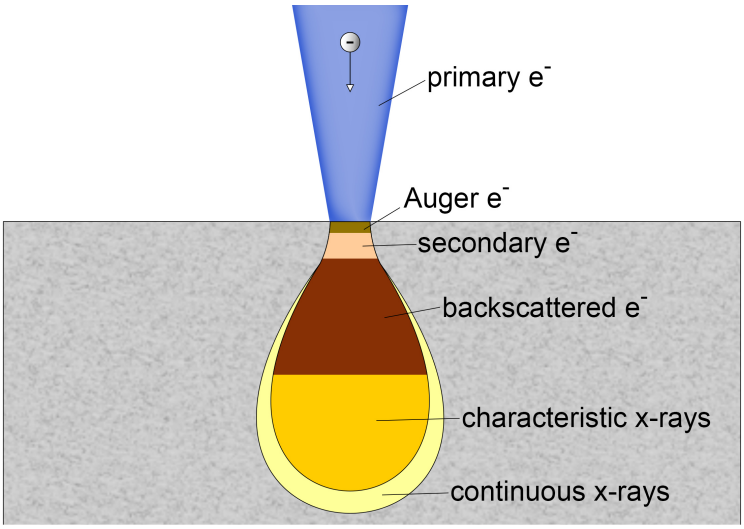

FIG. 2.15: Schematic of the interaction volume of an electron beam in a sample during scanning electron microscopy (SEM).

chemical analysis characteristic x-rays can be exploited which are generated by the ionization of sample atoms by electron collisions and subsequent de-excitation. In energy dispersive x-ray spectroscopy (EDX) these x-rays are recorded by an energy-dispersive detector. Due to their characteristic origin, elemental concentrations can be determined by comparison to a known standard signal of the element in question. However, it has to be considered that the interacting electrons require sufficient energy in order to excite the characteristic radiation of an element. Thus, the intensity of characteristic radiation decreases with interaction depth and finally only continuous radiation is generated.

The filling factor ρ of a composite of thickness d_c can be determined by comparison of the intensity I_f of the filling phase, corresponding to a nominal thickness d_f, to the intensity I_s of a pre-characterized standard deposit of thickness d_s

$$\rho = \frac{d_\mathrm{f}}{d_\mathrm{c}} = \frac{I_\mathrm{f}}{I_\mathrm{s}} \frac{d_\mathrm{s}}{d_\mathrm{c}} \quad . \tag{2.37}$$

In this calculation intensity variations due to limited penetration depth of the electron beam and varying intensity contributions within the interaction volume are neglected. This is justified on the one hand considering a penetration depth in the order of 1 μm versus a sample thickness of some 100 nm and on the other hand by choosing a standard sample thickness comparable to the investigated sample.

The method typically yields an error $\Delta\rho$ of the filling factor in between 10–20 % as calculated by gaussian error propagation

$$\Delta\rho = \left|\frac{d_\mathrm{s}}{I_\mathrm{s}\, d_\mathrm{c}}\right| \Delta I_\mathrm{f} + \left|\frac{I_\mathrm{f}}{I_\mathrm{s}\, d_\mathrm{c}}\right| \Delta d_\mathrm{s} + \left|\frac{d_\mathrm{s}\, I_\mathrm{f}}{I_\mathrm{s}^2\, d_\mathrm{c}}\right| \Delta I_\mathrm{s} + \left|\frac{d_\mathrm{s}\, I_\mathrm{f}}{I_\mathrm{s}\, d_\mathrm{c}^2}\right| \Delta d_\mathrm{c} \quad . \tag{2.38}$$

2.5.2 Transmission Electron Microscopy

In transmission electron microscopy the short wavelengths of electrons resulting from high acceleration voltages are exploited to obtain imaging resolution down to the atomic scale. A detailed discussion of the TEM technique can be found for example in the textbook by Williams and Carter[153].

As de Broglie found, a wavelength $\lambda = h/p$ can be related to an electron of momentum p. Considering relativistic effects at high energies above approximately 100 keV, one obtains for the electron wavelength

$$\lambda = \frac{h}{\left(2m_0 eU\left(1+\frac{eU}{2m_0c^2}\right)\right)^{1/2}} \tag{2.39}$$

where U is the acceleration voltage, m_0 the electron's rest mass and h Planck's constant. For $eU = 300\,\mathrm{keV}$, Equation (2.39) yields an electron wavelength of $\lambda \approx 2\,\mathrm{pm}$, motivating the minimal-resolvable distances TEM can achieve. In addition to real-space imaging, the short wavelength allows for crystallographic investigations by electron diffraction. An advantage of TEM compared to other diffraction techniques like XRD is the ability to probe a specimen's crystallography locally, down to the nanometer range. Accordingly, one refers to selected area electron diffraction (SAED). The same advantage holds for nanoprobe EDX which can be performed by TEM with lateral resolution in the nm-range. Exploiting the characteristic x-rays which are emitted from an ionized atom during de-excitation, elemental maps can be acquired.

While TEM represents a very versatile and powerful tool for nanoscale science, some experimental considerations have to be taken into account.

Obviously, specimens have to be thin enough to allow for transmittance of electrons. While the electron transparency is a function of electron energy and atomic number of the sample, the latter is typically required to be thinner than 100 nm. For atomic resolution imaging, a specimen thickness even below 10 nm might be necessary. The thinning can be conducted with different procedures like mechanical or focused ion beam (FIB) milling. Depending on the sample and thinning technique, the resulting specimen might be altered in the course of the preparation process.

Furthermore, the highly energetic electron beam might damage the sample. While this is true especially for polymers and biological samples, even inorganic specimens might be affected for example by induced crystallization. Among other techniques, sample cooling and scanning of the electron beam (STEM), are ways to avoid or minimize electron beam damage.

For the interpretation of TEM micrographs one has to be aware of the three-dimensional character of particulate nanocomposites. As illustrated in Fig. 2.16, the apparent particle distribution might differ in a top or cross-sectional view from the actual particle spacing since several particle layers contribute to the image.

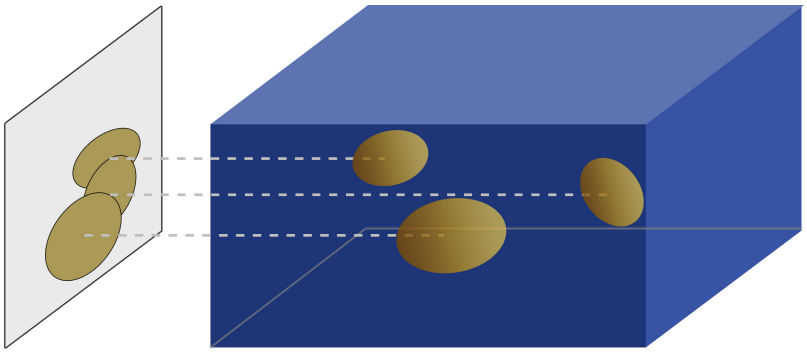

FIG. 2.16: Schematic of a 0-3 nanocomposite. Particles might appear connected in TEM micrographs while they actually are not.

The comparatively new TEM technique of electron tomography can overcome this obstacle by providing three-dimensional images of a specimen. This is achieved by combination of several TEM images taken at different sample tilts. However, as the technique is quite elaborate and time-consuming, it is not used for routine characterization.

2.5.3 X-ray Diffraction

The constructive interference of x-rays scattered by periodically arranged atoms is called *x-ray diffraction* (XRD). Diffraction thus represents a special kind of scattering which occurs only in certain directions with regard to the incident beam and atom lattice. An excellent introduction to XRD can be found in the textbook by Cullity[154].

Consider an incident x-ray beam at angle θ to the surface of a periodic lattice of atoms with lattice plane separation a as depicted in Fig. 2.17(a). From geometrical considerations it follows that constructive interference will occur upon satisfaction of Bragg's law

$$n\lambda = 2a \sin \theta_{\mathrm{B}} \tag{2.40}$$

where a is the distance between lattice planes, λ the x-ray wavelength, $n \in \mathbb{N}$ and θ_{B} the *Bragg angle*. From the requirement $\lambda < 2a$ follows the suitability of x-rays with typical $\lambda \approx 1.5\,\text{Å}$ for the investigation of crystal structures, having plane separations in the order of $a \approx 3\,\text{Å}$. As shown in Fig. 2.17(a) the *diffraction angle* between incident and diffracted beam is 2θ. The latter is measured in XRD experiments and the measurement of diffraction intensity versus diffraction angle is accordingly referred to as 2θ-scan.

The scan mode called *rocking curve* can be used in order to investigate the quality of crystal texture. In this mode the diffraction angle between x-ray source and detector is kept constant at the Bragg angle $2\theta_{\mathrm{B}}$ as shown in Fig. 2.17(b). Subsequently, the diffraction intensity is measured with respect to the incident

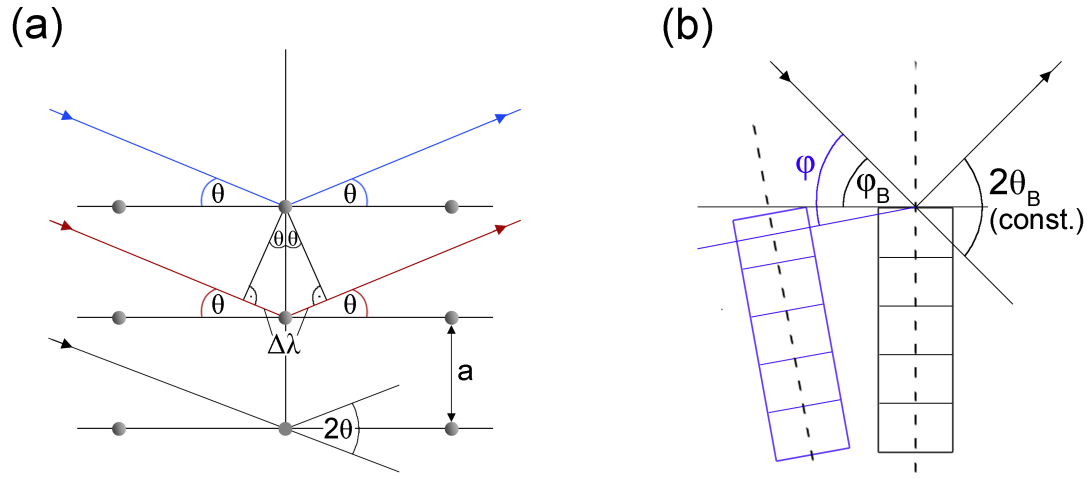

FIG. 2.17: (a) X-ray diffraction in a periodic lattice of atoms. (b) Illustration of rocking curve geometry.

angle φ. In this geometry, crystallites tilted from the preferred orientation contribute to diffraction intensity at $\varphi \neq \varphi_B$, leading to a broadening of the rocking curve. The rocking curve width is a measure of the piezoelectric effect in AlN as was discussed previously in chapter 2.3.1.

Since nanoparticles are studied, one has to take into account the effect of finite crystal size on x-ray diffraction. Consider an incident ray X at an angle slightly larger than the Bragg angle $\theta_1 = \theta_B + \delta\theta$. After l lattice planes the diffracted ray Y will have a phase difference of $(l+1)\lambda$ with respect to X. As a consequence, there exists a plane in between which results in a scattered ray Z with a phase $(k+1/2)\lambda$ ($k \in \mathbb{N}$) canceling out X. Thus, diffraction at the planes above Z cancels out with the planes below Z. The same is true at an angle $\theta_2 = \theta_B - \delta\theta$ slightly smaller than the Bragg angle. However, for the range of incident angles $S = \theta_1 - \theta_2$ destructive interference is incomplete and a non-zero intensity is observed although Equation (2.40) is not exactly satisfied. Considering a crystal of thickness D, the range of angles S increases with decreasing D. This is due to the fact that complete destructive interference is achieved with fewer crystal planes only for larger $\delta\theta$. The broadening β of a diffraction peak's FWHM due to finite crystal size D is expressed by the *Scherrer formula*

$$\beta = \frac{0.9\lambda}{D\,\cos\theta_B} \qquad (\beta \text{ in rad}). \tag{2.41}$$

2.5.4 Vibrating Sample Magnetometry

Vibrating sample magnetometry (VSM) is a standard technique for the characterization of ferromagnetic samples. Basically, VSM measures magnetic moment m by exploiting Faraday's law of induction.

A mechanical oscillator vibrates the sample at a defined frequency (typically 50–100 Hz) and a constant amplitude in a homogeneous magnetic field H generated by a pair of Helmholtz coils. Around the sample an additional pair of coils are arranged in which the changing magnetic flux induces a voltage $U = nA\dot{B}$, where n is the number of windings and A the coil surface. Since the applied magnetic field H generates a constant flux, that is $\dot{H} = 0$, it follows that

$$\dot{B} = \mu_0 \frac{\partial}{\partial t}(H + M) = \mu_0 \dot{M} \tag{2.42}$$

where the magnetization $M = dm/dV$ is the magnetic moment per unit volume of the sample. Thus, the induced voltage U is proportional to M and the applied magnetic field H does not contribute to U. Calibrating U to a standard of known magnetic moment allows the measurement of magnetic moment in absolute terms. Assuming homogeneous M, the magnetization can be calculated subsequently by $M = m/V$, if the magnetic volume V is known. Typically, VSM is able to measure magnetic moments in the μemu-range.

2.5.5 Double Beam Laser Interferometer

Displacement of a piezoelectric material can be measured with a double beam laser interferometer (DBLI) with an accuracy of several pm. It offers the possibility of contactless measurement making it suitable for thin-film characterization.[155] The double beam arrangement based on the Mach-Zehnder interferometer is capable of determining the actual thickness change of a piezoelectric film, rejecting the bending of the substrate due to in-plane stress of the deposit.[156] This is achieved by interference of laser beams reflected from both sides of the sample. The change in intensity of the resulting interference pattern serves as a measure of the path length difference of the two beams and thus represents the thickness change of the piezoelectric sample. Accordingly, double-side polished substrate has to be employed in order to provide the required reflectivity on the back of the sample.

Film clamping needs to be taken into account when interpreting the measured piezocoefficients. For a perfectly clamped film the in-plane strain components are $S_{1,2} = 0$ while the film is free to move in the out-of-plane direction. Accordingly $\sigma_1 = \sigma_2$ and $\sigma_3 = 0$ holds for the film in- and out-of-plane stress components, respectively. As a consequence, film clamping results in an effective piezoelectric coefficient[157,158]

$$d_{33,f} = \frac{S_3}{E_3} = d_{33} - \frac{2\, s_{13}^E}{s_{11}^E + s_{12}^E} \quad . \tag{2.43}$$

2.5.6 LCR Meter

Real electronic components contribute a mix of resistance R, capacitance C and inductance L. Depending on the frequency range, various measurement methods

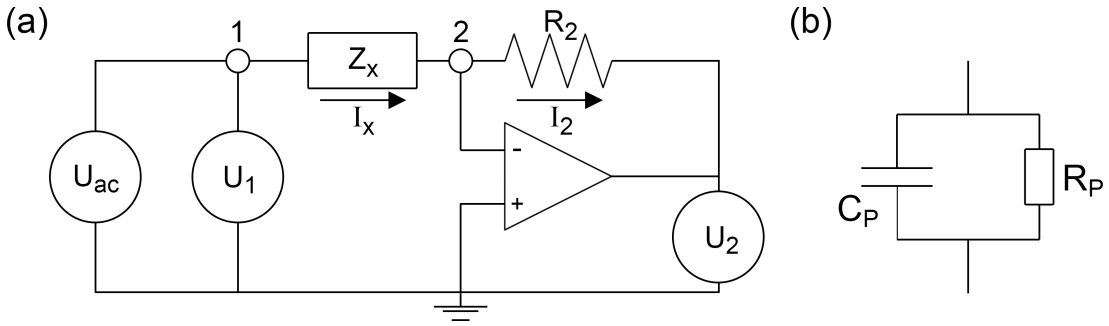

FIG. 2.18: (a) Principle circuit of an auto balancing LCR meter. (b) Parallel model of a non-ideal capacitor.

are available for the characterization of such electronic devices and the respective measurement equipment is referred to as *LCR-meters*. A commonly employed scheme in the range below 100 MHz is the auto balancing bridge illustrated in Fig. 2.18(a). In this setup the operational amplifier renders potential 2 a virtual ground and the current I_2 through R_2 balances with the current I_x through the investigated device Z_x. Hence $I_x = I_2$ and $U_2 = I_2 R_2$. The impedance Z_x can be determined by measuring U_1 and U_2 since

$$Z_x = \frac{U_1}{I_2} = \frac{U_1 R_2}{U_2} \quad . \tag{2.44}$$

For the properties of interest, the model of a lossy dielectric as a capacitor with capacitance C_p and parallel resistance R_p shown in Fig. 2.18 (b), yields

$$\tan\delta = \frac{1}{2\pi f C_\mathrm{p} R_\mathrm{p}} \tag{2.45}$$

$$\varepsilon_r = C_\mathrm{p} \frac{d}{\varepsilon_0 A} \tag{2.46}$$

where d is the thickness of the dielectric, A is the electrode area and ε_0 the vacuum permittivity. The error of ε_r resulting from geometric uncertainties in d and A is calculated by Gaussian error propagation.

2.5.7 Inductively Coupled Plasma - Mass Spectrometry

With inductively coupled plasma - mass spectrometry (ICP-MS) concentrations as low as $1 : 10^{12}$ of metals and various other elements can be determined. The sample usually consists of a solution which is nebulized into a reaction chamber. Within the latter an inductively coupled plasma ionizes the sample species. The inductive sustentation of the plasma offers the advantage that contamination of the electrodes is avoided as the latter can be arranged outside the reaction chamber. Subsequent to the ionization process the different ion species are separated

and detected by a mass spectrometer. Due to the high sensitivity of ICPMS care must be taken in the course of sample preparation. Already small contaminations of the used liquids or sample vessel might lead to erroneous results. In addition, the measuring device has to be calibrated in order to state correct concentration values in absolute terms.

2.5.8 Profilometer

Profilometry is a versatile method to characterize the surface of a sample. There are non-contact techniques which are mostly optical, and mechanical contact profilometers. The latter employ a stylus which scans the sample surface at a constant force thus retracing the topology. Contact profilometry offers the advantages of being independent of the optical properties of a sample and of directly imaging the surface without the need for subsequent modeling. For the characterization of deposits some area of the substrate should be left uncoated. This pristine part of the substrate provides a reference level on the one hand for the determination of the deposit's thickness and on the other hand for the removal of the macroscopic tilt of a sample (the *plane correction*).

2.5.9 Quartz Crystal Microbalance

A quartz crystal microbalance (QCM) exploits the resonance frequency shift of a quartz crystal upon addition of mass in order to determine and monitor deposition rates. The QCM concept was first introduced by Sauerbrey[159] in 1959. For mass detection, piezoelectric quartz crystals are driven by an electric field in a mechanical shear oscillation in the MHz-range. Deposited material shifts the crystal's resonance frequency by[159]

$$\Delta f = -C\,\Delta m \tag{2.47}$$

where C is the sensitivity factor of the crystal and Δm the change in mass per unit area. The frequency shift can be calibrated, for example with a profilometric measurement of a deposit, in order to represent the actual film thickness during deposition.

Chapter 3

Experimental setup

3.1 Design of new Deposition System

In the course of the presented work a high-vacuum (HV) system was designed and constructed[c] in order to enable highly flexible magnetron-based deposition of 0-3 nanocomposites.

As depicted in Fig. 3.1, the HV system consists basically of three independent chambers: the main deposition chamber, the gas aggregation cluster source (GAS) and a fast entry sample load lock. A detailed diagram of the system is given in appendix A.

The main chamber is pumped via a turbo molecular pump (TMU 521, Pfeiffer Vacuum) backed-up by an oil-free scroll pump (SH-110, Varian). The pressure within main chamber and load lock is measured by two full-range gauges (PKR 251, Pfeiffer Vacuum). The base pressure in the main chamber is $p_{\mathrm{base}} < 1 \times 10^{-5}$ Pa for all deposition experiments. The main chamber houses the sample holder and an elongated magnetron, the latter being mounted on an one-axis manipulator as depicted in Fig. 3.2.

The sample holder[d] is rotatable to ensure uniform deposition and it is mounted electrically disconnected to the chamber. Thus, deposition can be conducted with the sample being either on plasma floating potential, grounded or biased (cf. chapter 2). The substrate plate (35 mm diameter) made of Mo can be heated up to 1000 K by a resistively heated Ti filament.

Opposite the sample holder an elongated 2-inch planar magnetron (Thin Film Consulting) with a chimney ring is located for the deposition of the composite matrix. In case of the desired textured growth of AlN, this deposition geometry ensures the perpendicular orientation of the AlN c-axis with respect to the substrate plane. The magnetron is mounted on an one-axis manipulator (z-drive), which allows for variation of the target-substrate distance $d = 45$–95 mm, increas-

[c] in cooperation with S. Rehders
[d] design by S. Rehders

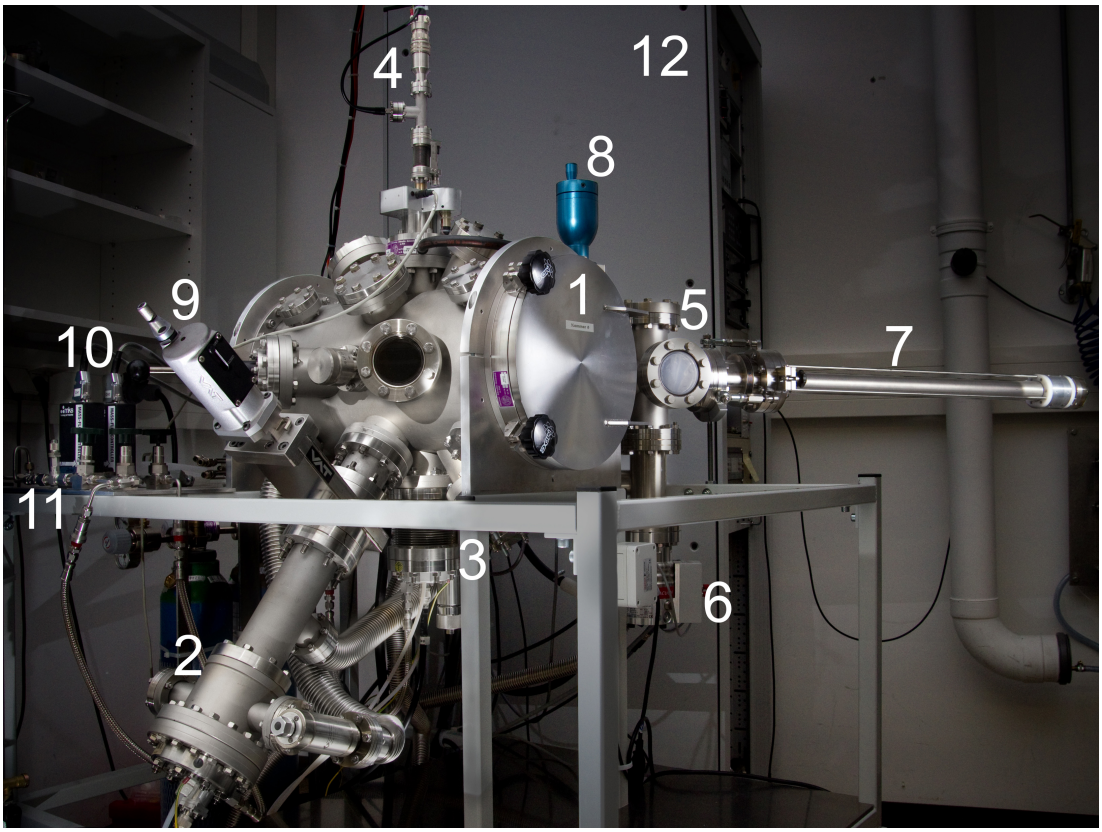

FIG. 3.1: Deposition system constructed in the course of the presented work.

1 - main chamber	5 - load lock (LL)	9 - gate valve
2 - cluster source (GAS)	6 - turbo pump LL	10 - gas flow controllers
3 - center magnetron	7 - magnetic transfer rod	11 - manual needle valve
4 - sample holder	8 - gate valve	12 - electronics rack

ing the flexibility of the system; in the case of AlN, d is critical for the textured growth of AlN (cf. chapter 4.1).

For the fabrication of AlN/Co composites a 10 mm wide slit was cut into the magnetron chimney ring, through which the cluster beam can reach the substrate. The process gases Ar and N_2 can be introduced into the magnetron via a four-channel gas flow controller (MKS) at flows of $\Phi_{\mathrm{Ar,\,N_2}} = 2$–$200$ SCCM. A dc power source (MDX 500, Advanced Energy) delivers up to 500 W continuous sputtering power. For the stable operation of the magnetron during reactive sputtering of AlN from a metallic Al target (99.999 % purity, Evochem), as discussed in chapter 2.4.1, the dc power is pulsed by a self-built switch[e] (MOSFET HTS31, Behlke). The switch is triggered via a square signal (5 V amplitude) from a frequency generator (PeakTech 4025) at frequencies typically between $f_{\mathrm{dc}} = 10$–70 kHz. During the deposition of composites the matrix magnetron is triggered additionally in

[e]design by R. Kloth

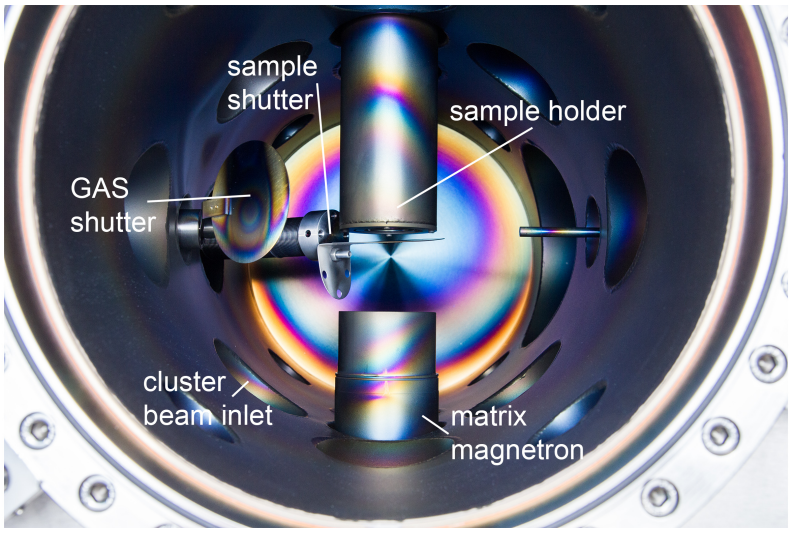

FIG. 3.2: Front view of the open main chamber.

low-frequency pulses in the order of $f_p = 0.1\,\mathrm{Hz}$, as part of the quasi-co-sputtering concept (cf. chapter 5.1). For the low-frequency pulsing, the MDX power unit is triggered in remote control by self-built electronics (cf. appendix A) and a second Peaktech 4025 frequency generator.

A fast entry sample load lock connected to the main chamber serves several purposes. The main vacuum needs not to be broken in the course of sample transfer, ensuring optimal HV deposition conditions. The pumping system of the load lock (HiPace 80 turbo molecular pump, Pfeiffer Vacuum, backed by a SH-110 scroll pump, Varian) allows for fast sample introduction with typical pumping times of $t \approx 20\,\mathrm{min}$ at a transfer pressure of $p_{\mathrm{LL}} \approx 5 \times 10^{-5}\,\mathrm{Pa}$. Apart from sample transfer, the load lock chamber can be used to monitor deposition experiments with a mass spectrometer (QME 200, Balzers). For this, the gate valve between main chamber and load lock is opened marginally, leading to a pressure in the order of $p_{\mathrm{LL}} = \mathcal{O}\,(10^{-3}\,\mathrm{Pa})$ in the load lock during deposition in the main chamber at $p_{\mathrm{main}} = \mathcal{O}\,(10^{-1}\,\mathrm{Pa})$. Finally, the load lock chamber supports the operation of the GAS in two respects. First, the load lock can be used to pump the gas escaping the GAS. This reduces the gas load of the main chamber during operation of the GAS, leading to a process pressure of $p_{\mathrm{main}} \approx 2 \times 10^{-1}\,\mathrm{Pa}$ compared to $p_{\mathrm{main}} \approx 6 \times 10^{-1}\,\mathrm{Pa}$ without the additional pumping. Second, the load lock allows venting of the GAS separately from the main chamber. This is especially important when working with thin ferromagnetic targets, like the utilized Co targets (0.5 mm thickness, 99.9 % purity, Goodfellow), since frequent replacement is required.

For the creation of nanoparticles a Haberland-type GAS was used. The source was developed in the working group as part of a research project by T. Peter in co-operation with V. Zaporojtchenko and S. Rehders. As illustrated in Fig. 3.3, the

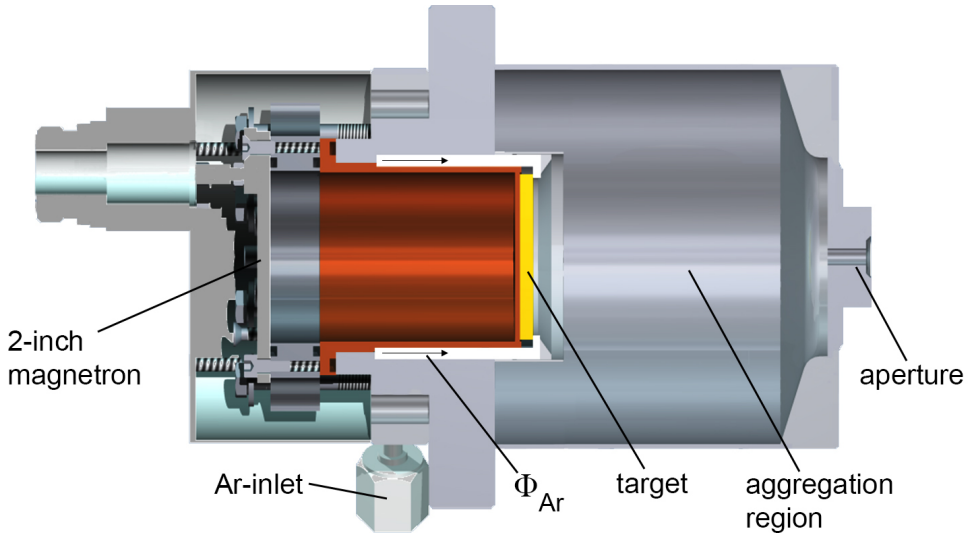

FIG. 3.3: Schematic of the Haberland-type self-built gas aggregation cluster source (design by S. Rehders). From Gojdka et al.[136].

GAS consists of a 2-inch planar magnetron which is mounted to a cylindrical vessel, providing the cluster aggregation region. The vessel is terminated by an aperture with a variable diameter (for all presented experiments a diameter of 3 mm was used). The design does not include any filtering system or cooling. Ar can be introduced via the magnetron at flow rates between $\Phi_{Ar,GAS}$ = 2–200 SCCM, controlled by a four-channel flow controller (MKS). An additional manual needle valve allows the introduction of N_2 with gas flows in the order of 0.1 SCCM for the investigation the influence of reactive gas on the cluster nucleation. During operation, gas flows of $\Phi_{Ar,GAS} \approx 120$ SCCM lead to pressure in the order of $p_{GAS} = 10^2$ Pa inside the aggregation vessel. Since the employed standard magnetron is specified for operation at $p \leq 10^0$ Pa this pressure can result in instable operation (cf. chapter 2.4.2); the magnetron is designed to work with targets of various thicknesses and thus incorporates a gap below the target cap as shown in Fig. 3.4(b). This geometry promotes an electrical breakdown since the electrode separation $d \approx 3$ mm shifts the breakdown voltage according to Paschen's law, Equation (2.36), toward it's minimum. Hence a ring is added to the magnetron as shown in Fig. 3.4(c) in order to decrease the electrode separation distance d. At the resulting distance $d \approx 1.5$ mm typical GAS operation yields $p\,d \approx 0.2$ Pa mm for which Paschen's law predicts a breakdown voltage of $V_B > 1$ kV. Accordingly, operation of the source is stable even at higher gas flow $\Phi_{Ar} \approx 200$ SCCM and power $P_{GAS} \approx 150$ W which would have resulted in arching inside the magnetron without the ring.

For the investigation of nanoparticle deposits without matrix, the GAS is mounted directly to the main chamber, resulting in an aperture-substrate distance of $d = 80$ mm. As for the deposition of nanocomposites, the setup aims at the

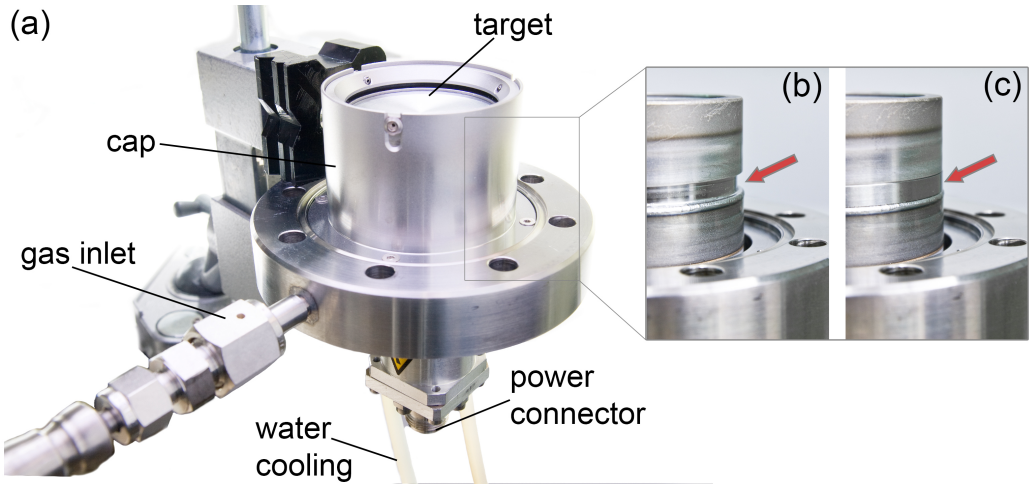

FIG. 3.4: (a) Photograph of a 2-inch magnetron employed in the cluster source and for matrix deposition. (b) The red arrow indicates the gap below the target fixture in the standard design. (c) Added steel ring to suppress arcing inside the magnetron during high-pressure operation of the cluster source.

separation of the cluster and matrix processes. Thus, it is desirable that the gas load of the cluster source is, at least partially, pumped before it enters the main chamber. To achieve this, the GAS is mounted to the main chamber via a DN63CF Tee, which is terminated by a blank flange with a drilled hole of 10 mm in diameter. This construction allows for differential pumping of the source via the fast entry lock as shown in Fig. 3.5(a). At a gas flow of $\Phi_{\mathrm{Ar,GAS}} = 120\,\mathrm{SCCM}$ from the source, a pressure of $p_{\mathrm{main}} = 2 \times 10^{-1}\,\mathrm{Pa}$ is reached in the main chamber. This is sufficiently low in order to control the process atmosphere for the AlN deposition. The high deposition rates of the GAS are matched to the rates of AlN by the large GAS aperture-substrate distance of $d = 450\,\mathrm{mm}$, which results from the introduction of a gate valve, the drilled blank flange and the Tee. For the preparation of different filling factors within one sample, a gas flow of 140 (SCCM) Ar is used in order to achieve a gradient of the Co filling factor via the focusing characteristic of the GAS (cf. chapter 4.2). Figure 3.5(b) illustrates the geometry for the deposition of nanocomposites by co-sputtering with the GAS and an elongated magnetron. The GAS can be baked out with an external heating belt ($T \approx 120\,^{\circ}\mathrm{C}$).

Optionally, a quartz crystal microbalance (QCM200 controller with QCM25-5 MHz crystal oscillator, Stanford Research Systems) can be positioned in the main chamber directly underneath the sample holder in order to monitor the nanoparticle deposition rate. The operation temperature of the QCM is stabilized by water cooling to prevent errors due to thermal drift of the oscillator's resonance frequency. Both magnetrons and the sample holder are water-cooled via an autonomous water-air chiller (UC007, Huber).

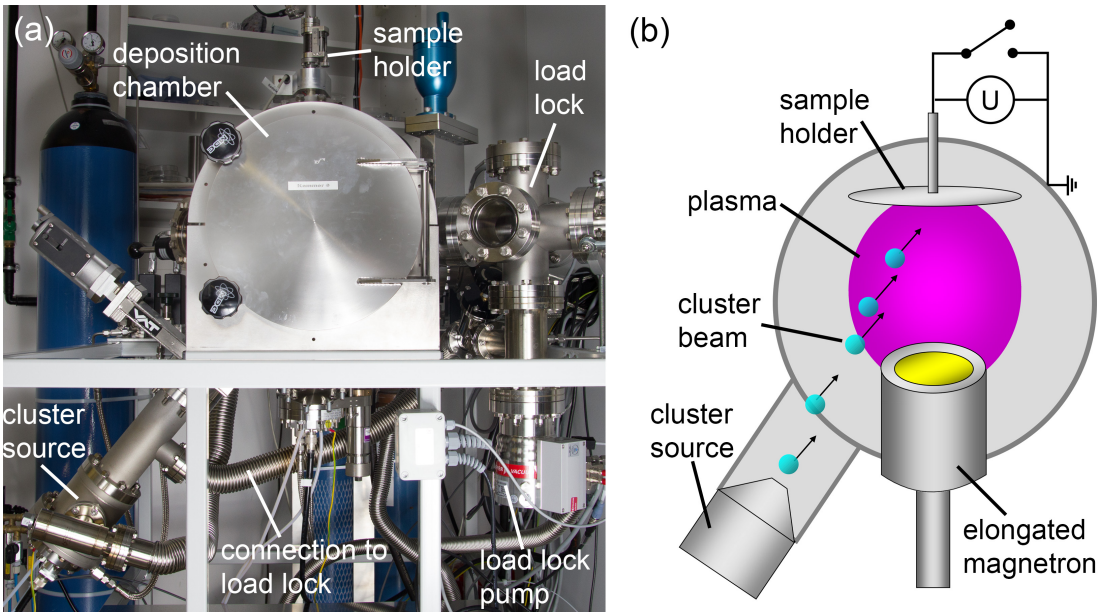

FIG. 3.5: (a) Front view of the deposition system, displaying the deposition geometry. (b) Respective schematic illustration.

3.2 Sample Characterization

Various measurement techniques were employed for sample characterization. Having summarized the respective theory previously in chapter 2.5, now the actual experimental procedures are addressed. Parts of the following discussion are excerpted from earlier publications by Gojdka et al.[55,136,160]

Crystallographic properties were investigated with a Seifert XRD 3003 in 2θ- and rocking curve mode. The x-ray source provides Cu-K_α radiation ($\lambda = 1.54$ Å) with an additional monochromator mounted in front of the detector in order to remove other wavelengths. For the direct comparison of different deposits (cf. chapter 5) identical Pt/Si substrates of $5 \times 5\,\mathrm{mm}^2$ were used. The intensive Si(400) and Pt(111) diffraction peaks of the highly oriented substrate were omitted in 2θ-scans if the detector limit of 1×10^5 cps was exceeded. The determination of miller indices for the observed diffraction peaks is based on the ICDD database PCDFWIN, v.2.1 (2000).

All TEM measurements and analyses presented in this thesis were performed by L. Kienle and V. Hrkac. The TEM investigations were conducted with a Tecnai F30 G^2 STwin. For the study of individual nanoparticles, carbon-coated Cu-microgrids (S160-3, Plano) were directly exposed to the cluster beam of the GAS for $t = 1$–8 s, depending on the GAS operation parameters. Several TEM micrographs were recorded at fixed magnification at random positions of the samples for statistical analysis of the particle's size distribution. Scanning (S)TEM images displaying atomic number dependent (Z)-contrast were recorded with a

high angle annular dark field detector. For cross-sectional TEM investigations lamellae specimens were prepared by focused ion beam (FIB) milling of deposits using a lift-out method with a FEI Helios Nanolab system. In addition, crystallography was probed locally by selected area electron diffraction (SAED). EDX nanoprobe analyses as part of the TEM examinations were performed using a Si/Li detector (EDAX System).

Morphology and chemical composition of deposits were investigated by SEM (Philips XL 30) with EDX detector (EDAX DX-4). In order to determine the Co content in AlN/Co composites, the Co-K net intensity recorded for the composite was compared to the Co-K net intensity of a standard sample. The latter consists of a (160 ± 10) nm thick Co layer, one third of which is blank, while the other 2 thirds are covered by 450 nm AlN and 900 nm AlN, respectively. Depending on the composite thickness and structure, the average of the measured Co-K net intensities from the different standard regions yields the nominal Co thickness of the AlN/Co composite within acceptable error limits (cf. chapter 2.5).

A DEKTAK 8000 profilometer was employed in order to determine the thickness and topology of deposits. During deposition part of the substrate was covered by an approximately 1 mm wide stripe of metal in order to provide a reference level for the measurements. For samples deposited at elevated temperatures, Ta was used for the cover, otherwise Al foil sufficed at room temperature. After the deposition, the blank parts of the substrate provided the zero-level for the thickness determination by profilometry.

The mass of porous Co nanoparticle films was determined via inductively coupled plasma mass spectrometry measured on an AGILENT 7500cs ICP-MS instrument. The respective deposits were dissolved in 10 ml of 6.5 % HNO_3. With all of the deposited Co in solution and the amount of solution known, the Co mass can be directly calculated from the concentration determined by ICP-MS. In order to calibrate the ICP-MS data, a dense Co deposit of known volume was dissolved as a concentration standard.

Magnetic properties were measured by a LakeShore 7300 vibrating sample magnetometer (VSM) at room temperature. The system provides large and small pick-up coils for the measurement of sample magnetic moment m with respect to applied external field H. Due to geometric constraints of the more sensitive smaller pick-up coils, VSM samples were prepared on $5 \times 5\,\mathrm{mm}^2$ substrates.

For the study of piezoelectric properties of the deposited AlN, a double beam laser interferometer (DBLI, aixacct) was employed. In order to provide the necessary reflectivity, double-side polished (DSP) substrate was used. The Pt seed-layer of the substrate serves as bottom electrode, while Au top electrodes were sputter-deposited ex-situ with a Balzers SCD 050 sputter coater. Since AlN exhibits a comparatively small $d_{33} \approx 5\,\mathrm{pm/V}$, 10 to 100 displacement-curves were averaged in order to reduce the error of the measurement.

Electric properties like relative dielectric permittivity ε_r and loss tangent $\tan\delta$ were determined in a two-contact arrangement with an HP 4284A LCR meter in

parallel resistance-capacitance ($R_\mathrm{P} - C_\mathrm{P}$) mode. The electrode arrangement is identical to the previously described sample design for DBLI.

Magnetoelectric measurements were conducted with a self-constructed device. Two pairs of Helmholtz-coils provide a magnetic bias field of $H_\mathrm{dc} \leq 5\,\mathrm{kOe}$ and an alternating field $H_\mathrm{ac} \approx 3\,\mathrm{Oe}$. Sweeping H_dc tunes the working point of the magnetostrictive phase in a ME composite while H_ac results in an alternating voltage U_ME according to Equation (2.25). The Pt bottom electrode of the substrate and Au top electrodes (cf. DBLI) were connected to a lock-in amplifier (7265 DSP, EG&G Instruments) in order to detect U_ME.

Chapter 4

Individual Composite Constituents

Prior to the investigation of 0-3 nanocomposites, deposition processes for the individual constituents had to be developed and the properties of the separate phases were characterized.

4.1 Deposition of high-quality AlN

A suitable deposition process had to be established in the course of this work in order to produce piezoelectric AlN, enabling an AlN/Co composite to potentially exhibit a ME effect. The process had to be developed entirely anew since on the one hand the deposition system was newly constructed as part of this thesis and on the other hand no experimental experience regarding AlN and piezoelectric ceramics in general existed in the working group.

The growth of AlN is influenced by a wide range of parameters. Thus, suitable deposition parameters had to be found in order to produce highly oriented, piezoelectric AlN. On the one hand a systematic variation of only one parameter at a time would not have been possible for reasons of time due to the large field of parameters. On the other hand various systematic studies already exist for reactive pulsed dc sputter deposition of AlN.[73,74,76,77,129,161,162] These reports provided a sound first set of parameters which was subsequently optimized under consideration of the influence of the individual deposition parameters on the physics of the deposition. Exclusive c-axis orientation provided the first criterion and was studied by XRD in 2θ- geometry. Subsequently, XRD rocking curves allowed quick assessment of the piezoelectric capabilities of a deposit with the FWHM being the figure of merit. If exclusive c-axis orientation and FWHM $< 3.5°$ were fulfilled, finally DBLI was employed to characterize piezoelectric properties of the AlN deposits. In addition to the desired material properties, the deposition process was developed in order to be compatible with co-deposition of composites. This boundary condition has been taken into account by introducing part of the process gas via the cluster source, as is the case during co-deposition.

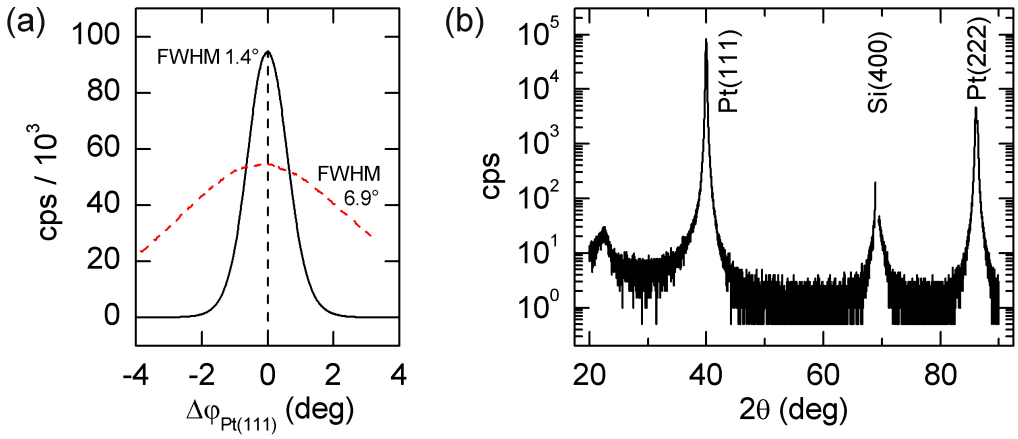

FIG. 4.1: (a) XRD rocking curves of the Pt(111) diffraction peak of self-sputtered[f] (black, solid) and commercial substrate (red, dashed), respectively. (b) XRD 2θ-scan of self-sputtered Pt(111)-Si substrate.

The establishment of a suitable deposition process for the growth of piezoelectric AlN posed a fundamental objective within the framework of the presented thesis. Thus the developed deposition procedure and the choices of parameters will be discussed in the following, complimented by experimental data. Finally, highly c-axis oriented, piezoelectric AlN deposits are characterized, proving the feasibility of the developed process.

First, the substrate was characterized as it represents the essential starting point for the growth of AlN. According to the discussion in chapter 2.3.1, the substrate consists of platinized Si. Commercial platinized Si-wafers (Inostek) were compared to substrate provided by a co-operating research group[f]. For the non-commercial substrate 150 nm Pt was sputter-deposited on 4-inch double-side polished (100)-Si prime-grade wafers. The latter were wet oxidized to form a 1 μm thick SiO_2 diffusion barrier layer prior to deposition. A 10 nm layer of Ti was added on top of the SiO_2 in order to promote adhesion. The Pt-coated wafers were post-annealed at 500 °C for 1 h in order to improve the Pt(111) texture. Figure 4.1(a) shows the XRD rocking curves of the commercial and the self-deposited substrate. A FWHM of 6.9° renders the commercial substrate unsuitable as a seed layer for highly oriented AlN. On the other hand, the self-sputtered substrate exhibits a small FWHM of 1.4°, offering good growth conditions. Exclusive Pt(111) texture is observed in the 2θ-scan shown in Fig. 4.1(b). In accordance with previous studies[74,77] $T_s \approx 300$ °C is used for the growth of AlN. Mortet et al.[161] reported improving c-axis orientation for decreasing target-substrate distances in the range of $d = 130 - 50$ mm. Thus, a target-substrate distance of $d = 55$ mm was chosen and adjusted with the one-axis manipulator (cf. chapter 3.1).

In the course of this thesis, pulsed dc power was used for the first time in the

[f] courtesy of A. Piorra and E. Quandt

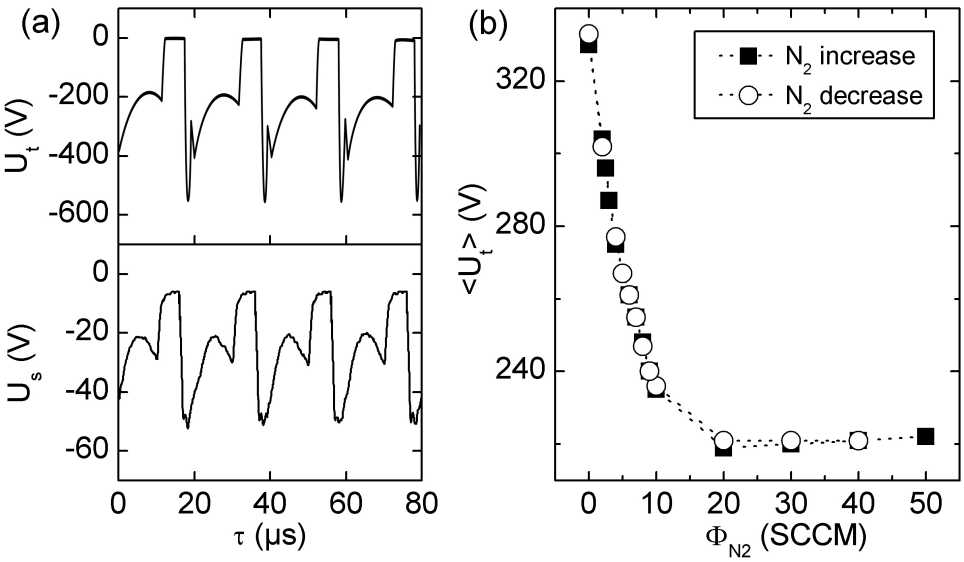

FIG. 4.2: (a) Top: pulsed target bias $U_\mathrm{t}(t)$ for $f_\mathrm{dc} = 50\,\mathrm{kHz}$, duty cycle 70 % and $P = 90\,\mathrm{W}$. Bottom: resulting self-bias $U_\mathrm{s}(t)$ of electrically floating substrate holder (note: the graph was extracted from an oscilloscope photograph by digital image processing). (b) Average target bias U_t versus Φ_{N_2}.

research group. Figure 4.2(a) shows typical $U_\mathrm{t}(t)$ for $f_\mathrm{dc} = 50\,\mathrm{kHz}$ and a duty cycle of 70 % at an average sputtering power of $P = 90\,\mathrm{W}$. As is usually observed for this mode of operation,[123] $U_\mathrm{t}(t)$ is not perfectly square but exhibits overshoots. Depending on the deposition parameters and the pulsing frequency f_dc, the target bias U_t reaches 0 V during the off-times and arc-free stable sputtering operation is achieved even if the process gas is pure N_2.

Subsequently, the dependence of average target bias $U_\mathrm{t} = \langle U_\mathrm{t}(t) \rangle$ provided by the power generator versus nitrogen flow $\Phi_{\mathrm{N}_2,\,0}$ was studied in order to characterize the target state during the reactive sputtering process (the index '0' denotes gas flows through the center magnetron). As shown in Fig. 4.2(b) a decrease of U_t is observed for increasing nitrogen flow (cf. chapter 2.4.1 for the algebraic sign convention). However, no hysteresis is observed, likely due to the comparatively small target area and high pumping speed as discussed in chapter 2.4.1. Mortet et al.[161] found exclusively c-axis orientated AlN for a nitrogen ratio of $R_{\mathrm{N}_2} = \Phi_{\mathrm{N}_2}/(\Phi_\mathrm{Ar} + \Phi_{\mathrm{N}_2}) > 25\,\%$. Considering a gas flow $\Phi_{\mathrm{Ar,\,GAS}} \approx 120\,\mathrm{SCCM}$ and additional $\Phi_{\mathrm{Ar},\,0} = 15\,\mathrm{SCCM}$ introduced through the center magnetron in order to prevent target poisoning, a nitrogen flow of $\Phi_{\mathrm{N}_2,\,0} = 65\,\mathrm{SCCM} \mathrel{\hat{=}} R_{\mathrm{N}_2} = 32.5\,\%$ was chosen. The resulting AlN deposit exhibits a stochiometry of 1:1 within the accuracy of EDX.

After the establishment of basic pulsed dc operation and a suitable process atmosphere, the pulsing frequency f_dc and respective duty cycle were chosen based on the resulting substrate bias voltage U_s. Figure 4.2(a) depicts the substrate bias

Parameter		Parameter	
dc power [W]	90	$\Phi_{\mathrm{Ar,\,0}}$ [SCCM]	15
f_{P} [kHz]	50	$\Phi_{\mathrm{N_2,\,0}}$ [SCCM]	65
$\mathrm{duty_P}$ [%]	70	$\Phi_{\mathrm{Ar,\,GAS}}$ [SCCM]	100-140
target-sample distance [mm]	55	substrate temperature [°C]	200-400

Table 4.1: Summary of deposition parameters for AlN. Index 0 in gas flows denote the center magnetron.

voltage which occurs on the electrically floating sample holder (with respect to chamber ground) due to the deposition plasma. It should be emphasized that this bias voltage U_{s} is not applied to the sample holder externally by means of an additional voltage supply but results directly from the deposition plasma. As Dubois and Muralt[77],[163] reported, the AlN film quality improves with substrate bias with best results for U_{s} in between $-40\,\mathrm{V}$ and $-50\,\mathrm{V}$. In addition Cherng and Chang[129] obtained best results for a pulsing frequency of $f_{\mathrm{dc}} = 50\,\mathrm{kHz}$. Accordingly, pulsing parameters of $f_{\mathrm{dc}} = 50\,\mathrm{kHz}$ and a duty cycle of 70 % were chosen, resulting in a substrate peak bias of $U_{\mathrm{s}} \approx -45\,\mathrm{V}$.

Table 4.1 summarizes the parameters which were also used for the fabrication of AlN/Co nanocomposites in chapter 5. Since the process has been newly developed in the course of this work, the deposition procedure is detailed in appendix B.

The process yields exclusively c-axis oriented AlN as shown in Fig. 4.3(a) for a 400 nm thick deposit. Due to an XRD rocking curve FWHM of 1.8°, as shown in Fig. 4.3(b), the AlN deposit can be regarded highly c-axis oriented.[73,74] Figure 4.3(b) also includes data of AlN deposited at room temperature for reference. Under these conditions the intensity decreases fourfold while the FWHM widens to 3.9° demonstrating the feasibility of the chosen deposition parameters. As shown in Fig. 4.4(a) the deposit with FWHM = 1.8° yields a piezoelectric coefficient $d_{33,f} = (5.5 \pm 0.1)\,\mathrm{pm/V}$, which is comparable to the results of other reports as summarized in Table 4.2. A relative permittivity of $\varepsilon_r = 9.4 \pm 0.1$ and dielectric loss $\tan\delta = (4.5 \pm 0.1) \times 10^{-3}$ for $f = 10^3$–$10^5\,\mathrm{Hz}$, Fig. 4.4(b), are also in good agreement with reported values for high-quality AlN (cf. Table 4.2).

Reference	$d_{33,f}$ (pm/V)	ε_r	$\tan\delta\,(10^{-3})$
Marauska et al.[74]	4.7–5.2	10.2–10.7	1–5
Martin et al.[73]	4.6–5.2	≈ 10	≈ 5
Lanz et al.[164]	5.1–5.7	10.1	3
this work	5.4–5.6	9.3–10.5	4.4–4.6

Table 4.2: Comparison of AlN properties measured in this work and reported in other investigations.

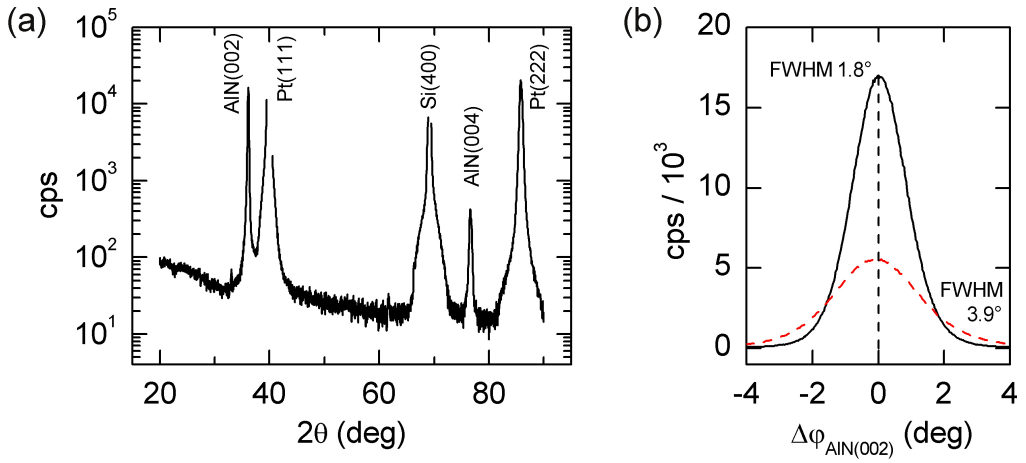

FIG. 4.3: (a) XRD 2θ-scan of 400 nm AlN on Pt(111)-Si substrate. (b) XRD rocking curves of the AlN(002) diffraction peak of 400 nm AlN deposited with the parameters of Table 4.1 at $T_s = 300\,^{\circ}\mathrm{C}$ (black, solid) and at room temperature (red, dashed).

In summary, a pulsed dc reactive sputtering deposition process has been established which yields highly c-axis oriented, piezoelectric AlN with good electric properties. The parameters of the process were chosen in order to be compatible with the simultaneous operation of a gas aggregation cluster source for the co-deposition of preformed nanoparticles. The latter will be investigated in the following chapter.

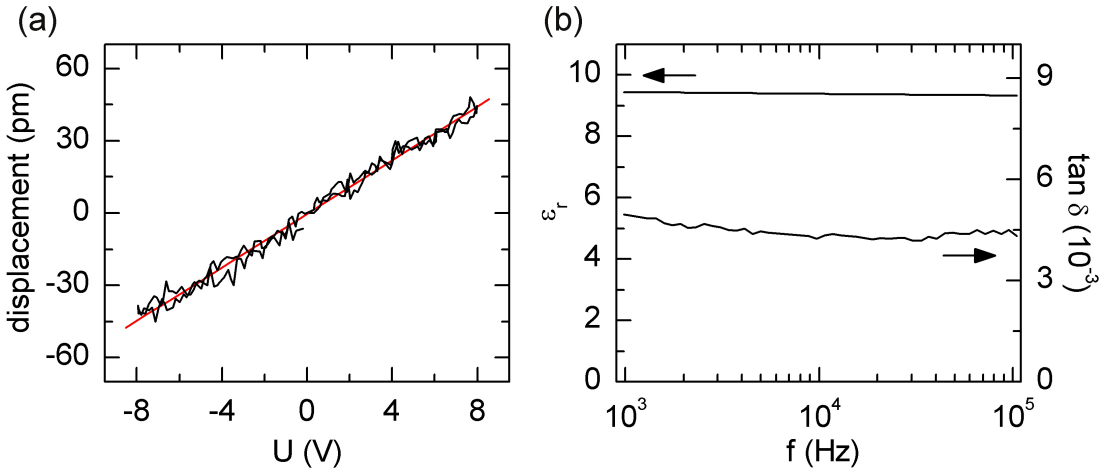

FIG. 4.4: (a) Displacement of a piezoelectric AlN deposit (400 nm) versus applied voltage. (b) Relative permittivity ε_r and dielectric loss $\tan\delta$ for $f = 10^3$–10^5 Hz and a small signal amplitude of $V_{\mathrm{rms}} = 100$ mV.

4.2 Study of Magnetic Co-Nanoparticles

In order to characterize the particle output of the self-constructed GAS, individual nanoparticles were prepared and characterized. Subsequently, particle films of several hundreds of nanometers thickness were deposited with the GAS. The films were investigated regarding their morphology, magnetic properties and magnetic aging behavior. Most of the following results are excerpted from a respective publication by Gojdka et al.[136].

In order to study individual clusters before agglomeration and coalescence, a coverage well below one monolayer was prepared with deposition times in the order of a few seconds. A respective overview is shown in the TEM micrograph of Fig. 4.5(a). The cluster size distribution was evaluated for different deposition parameters from TEM bright-field images as shown in Fig. 4.5(b). For every sample several micrographs at random positions were evaluated in order to determine the respective size distribution.

As displayed in Fig. 4.6 statistical analysis yields a virtually constant average cluster diameter of $D = 4.6$–$5.4\,\mathrm{nm}$ and a very narrow size distribution with a standard deviation of $\sigma = 0.6$–$0.8\,\mathrm{nm}$ within the investigated field of parameters ($P = 70$–$130\,\mathrm{W}$, $\Phi_{\mathrm{Ar,GAS}} = 50$–$100\,\mathrm{SCCM}$). The observed size distribution fits well to a lognormal distribution, in accordance with previous reports.[165] In addition, He et al.[166] found the size distribution of Ag clusters to be independent of the deposited amount of clusters if the clusters do not coalesce due to low surface mobility. A comparison of Figs. 4.5(a) and 4.7(a) with the results of He et al.[166] evidences that one can assume the non-coalescing case for the investigated system, rendering the observed size distributions independent of deposited mass.

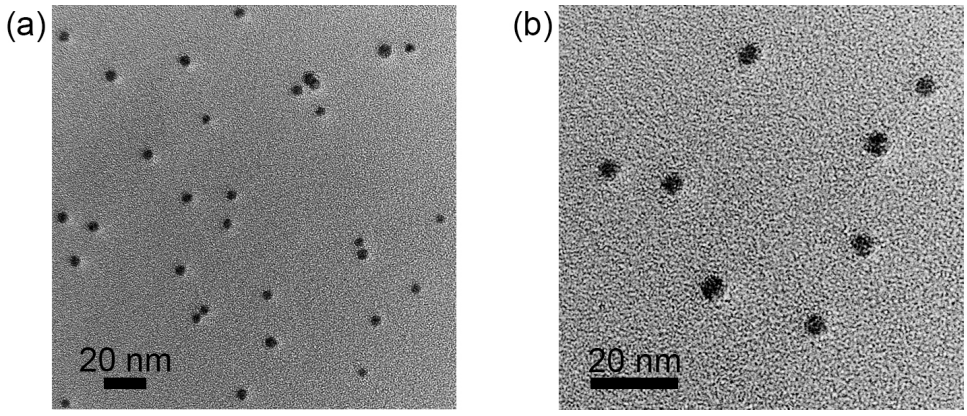

FIG. 4.5: (a) TEM-image of separated Co nanoparticles created with the gas aggregation source ($P = 130\,\mathrm{W}$, $\Phi_{\mathrm{Ar,GAS}} = 100\,\mathrm{SCCM}$, $t < 1\,\mathrm{s}$). (b) Typical TEM-image of individual spherical Co nanoparticles used for the evaluation of the size distribution. From Gojdka et al.[136].

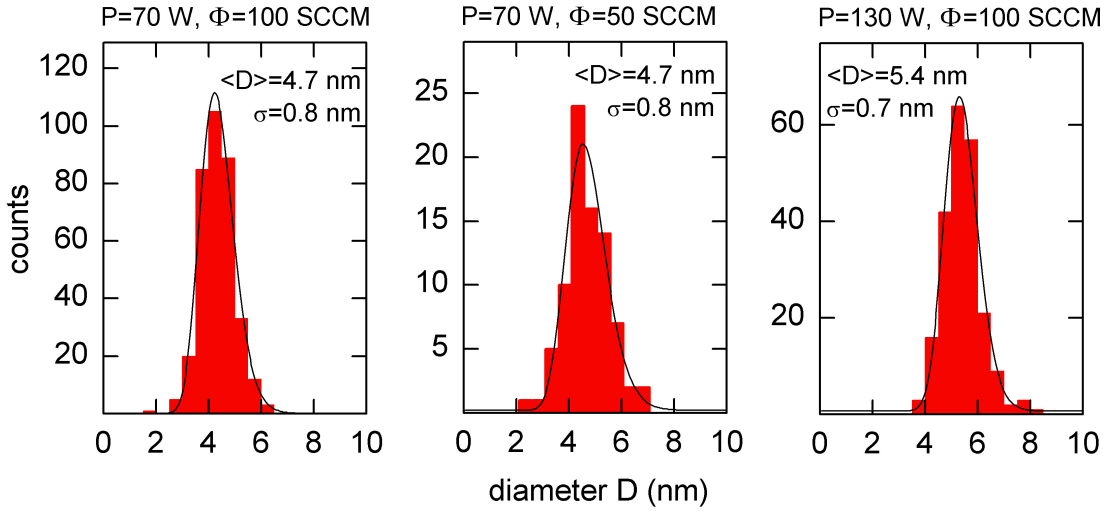

FIG. 4.6: Size distribution of as-deposited clusters for different values of dc power and deposition pressure following a lognormal distribution (black line). The histograms were extracted from TEM micrographs at random sample positions. From Gojdka et al.[136].

The growth of the film was investigated at different growth stages. As shown previously in Fig. 4.5, the clusters arrive at the substrate individually and not agglomerated. At a higher substrate coverage, displayed in Fig. 4.7(a), the clusters start to agglomerate on the surface and form percolated networks. The chemical investigation of an agglomerate of nanoparticles, shown in Fig. 4.7(b), reveals a core of metallic Co, Fig. 4.7(c), with an oxidic shell, Fig. 4.7(d). In accordance with these findings Bødker et al.[167] reported that Co nanoparticles form a passivating layer of CoO when oxidizing at room temperature. Since the CoO shell encompasses the cluster agglomerate and no shell is observed around individual clusters inside the agglomerate, the oxidation likely occurred upon exposure of the particles to ambient conditions. This indicates that during the deposition metallic particles are produced and no contamination of the Co takes place within

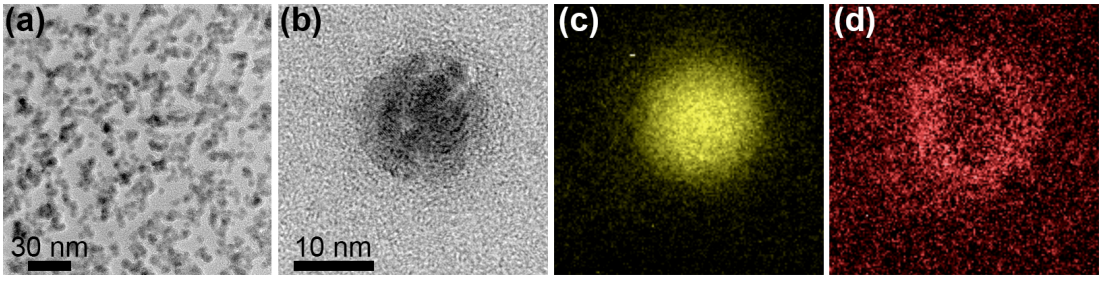

FIG. 4.7: (a) TEM bright-field image of a percolating cluster film exhibiting local agglomeration. (b) HRTEM micrograph of a cluster agglomerate. (c) and (d) Elemental (EFTEM) maps of (b) for Co and O, respectively, revealing a Co-CoO core-shell structure of the agglomerate. From Gojdka et al.[136].

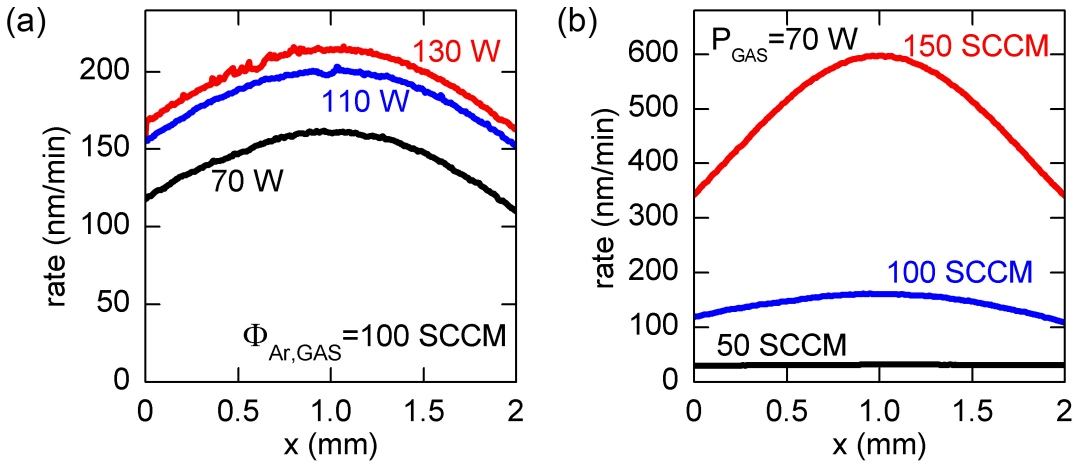

FIG. 4.8: Lateral deposition rate characteristic of the cluster source determined by profilometry. (a) Constant pressure ($p_{GAS} = 100\,Pa$) and (b) constant power ($P_{GAS} = 70\,W$). From Gojdka et al.[136].

the deposition system. Magnetic measurements presented later in this chapter agree with the contamination-free deposition of metallic Co nanoparticles.

Films with a thickness of several hundreds of nanometers were prepared with the gas aggregation source at deposition times of $t = 3$–$5\,min$. The deposition rates r and film profiles, shown in Fig. 4.8, are investigated for several sets of deposition parameters. Within the investigated field of parameters, average deposition peak rates up to $r = 600\,nm/min$ were achieved. Since this rate was observed at a moderate sputtering power of $P_{GAS} = 70\,W$ higher rates are achievable with the studied GAS. A variation of the sputtering power does not influence the cluster beam spread and the rate is approximately $r \propto \sqrt{P_{GAS}}$ as shown in Fig. 4.8(a). In contrast, the lateral deposition profile of the cluster beam is strongly influenced by the pressure inside the cluster source. The cluster beam is focused at the 3 mm wide aperture by the flow of the gas leaving the source,[168,169] thus strongly affecting the deposition profile. On changing the Ar gas flow $\Phi_{Ar,GAS}$ from 50 SCCM to 150 SCCM, the maximum deposition rate increases by a factor of 15 as depicted in Fig. 4.8(b). The high rates could be interesting for technical applications. A functional coating on large areas may for example be realized with a parallel arrangement of several sources and/or a scanning substrate.

At a later stage of growth highly porous films evolve, Fig. 4.9(a), as is typical for soft-landing clusters[144,170] and predicted by Monte-Carlo simulations[170]. In order to determine the mass of the porous and inhomogeneously shaped films, ICP-MS was employed rather than a quartz microbalance. The latter requires a homogeneous deposition of a rigid film on the quartz crystal.[159] Both requirements are not fulfilled in case of the porous nanoparticle films and an independent calibration of the microbalance response in terms of absolute deposited mass would be necessary. Hence the deposited mass of the nanoparticle films was de-

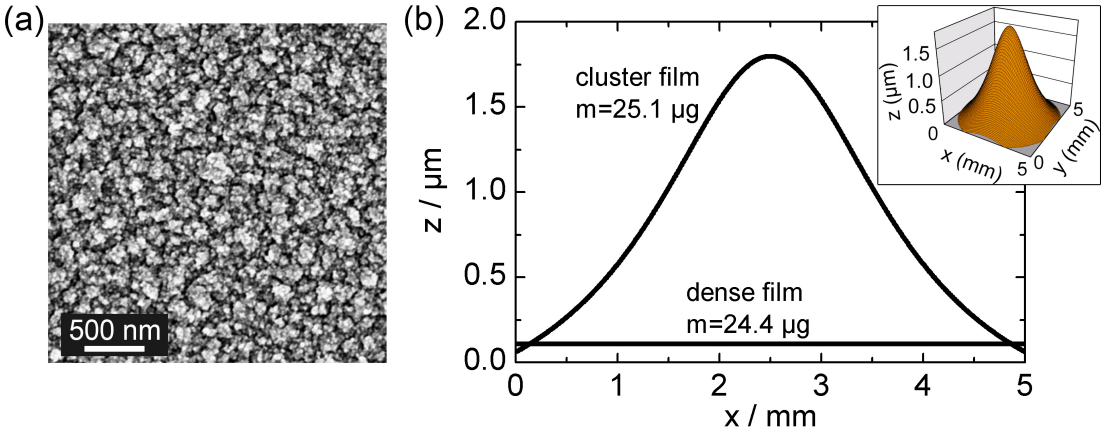

FIG. 4.9: (a) SEM micrograph of porous nanoparticle film with an average thickness of 900 nm. (b) Profiles of a conventionally dc sputter-deposited Co film (24.4 μg) and a porous nanoparticle film (25.1 μg) on a $5 \times 5\,\mathrm{mm}^2$ Si-substrate, yielding a porosity of the nanoparticle film of 74 % compared to the dense film. Inset: 3D-model of the topology of the nanoparticle film. From Gojdka et al.[136].

termined via ICP-MS after dissolution of the samples in HNO_3. The cluster films are compared to a conventionally dc-sputtered Co film with a thickness of 110 nm. While both films are of similar mass with $m = 25.1\,\mu$g for the porous sample and $m = 24.4\,\mu$g for the dense film, respectively, their topology significantly differs. Figure 4.9 depicts the thickness profiles of both deposits on a $5 \times 5\,\mathrm{mm}^2$ substrate. To determine the porosity of the nanoparticle film, the volume is calculated from the measured profiles. This leads to a porosity of 74 % for the nanoparticle film compared to the dense, conventionally sputter-deposited film. The result is in good agreement with previous reports on similar nanoparticle deposits[171]. Both the high porosity of the nanoparticle films and the narrow size distribution of the individual clusters are potentially useful for example in catalytic applications.[27,172]

XRD investigations were conducted on nanoparticle films in order to determine the crystallinity of the deposits and as a reference for the characterization of AlN/Co nanocomposites in the following chapter. Figure 4.10 shows the XRD 2θ-scans of a several μm thick nanoparticle film compared to a 0.5 mm thick piece of 99.9 % pure foil from a Co target. The three strongest powder diffraction peaks belonging to the (101), (002) and (100) planes are clearly observed for the Co foil with a (101) intensity of 300 cps. However, using the same scan parameters (slits, x-ray current and voltage), no peaks occur for the nanoparticle film. Assuming an x-ray coherence length $D_x < 5$ nm in a nanoparticle of 5 nm diameter due to crystal defects and grain boundaries (cf. Fig. 4.7(b)), Equation (2.41) yields a peak width of $\beta \approx 5°$. Considering the peak broadening on the one hand and on the other hand the peak intensity of 300 cps of the 0.5 mm thick Co-foil as an upper intensity limit for the micron-thick nanoparticle film, the Co diffraction

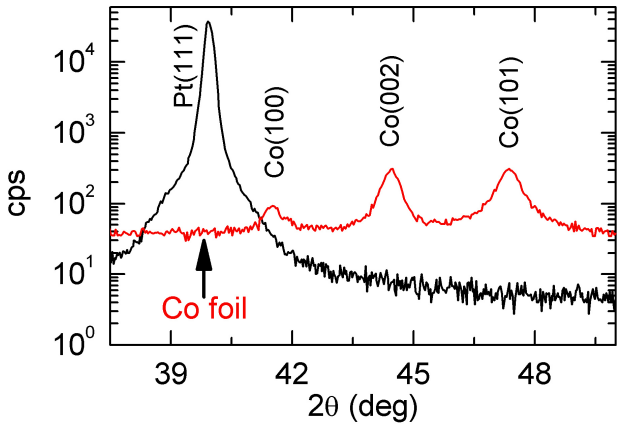

FIG. 4.10: XRD 2θ-scan of a several μm thick Co nanoparticulate deposit and a 0.5 mm thick Co foil for reference.

pattern of the cluster film can be regarded within the XRD noise floor. Thus, the absence of Co diffraction peaks does not indicate an absence of Co nanoparticles. This finding is confirmed by the subsequently presented magnetic properties of the Co nanoparticle deposits and by EFTEM studies of AlN/Co nanocomposites in chapter 5.2.

VSM measurements establish that the nanoparticle films are ferromagnetic at room temperature as shown in Fig. 4.11. No in-plane anisotropy was observed, indicating no preferred particle orientation. The coercivity of the nanoparticle films is 4.5 times higher than that of a conventionally dc-sputtered Co film. Gangopadhyay et al.[173], for example, observed for Co nanoparticles at cryogenic temperatures an enhanced coercivity due to exchange coupling between the metallic Co core and an antiferromagnetic CoO shell. However, although the Néel temperature of bulk CoO is $T_N = 270\,K$[85], Gangopadhyay et al.[173] found the exchange coupling to vanish already at $T > 150\,K$ for Co-CoO core-shell nanoparticles. Thus antiferromagnetic pinning has not to be taken into account here. The individual Co nanoparticles of 5 nm diameter are expected to be single-domain particles approximately at the superparamagnetic limit (cf. chapter 2.3.2). Former investigations of isolated Co particles and two-dimensional networks of 5 nm Co particles yielded blocking temperatures of $T_B = 58\,K$[174] and 63 K[175], respectively. However, ferromagnetic behavior at room temperature has already been observed for films consisting of Co particles with a mean diameter of 6 nm.[176] The observation of ferromagnetism at room temperature of the nanoparticle films is due to interparticle interaction (cf. chapter 2.1.3) and has been experimentally observed and investigated for similar Co, Fe and Ni deposits[176–178]. Furthermore, Peng et al.[176] report that deposits consisting of $D = 6\,nm$ Co particles, which were deliberately oxidized to form Co-CoO core-shell clusters prior to deposition, do not exhibit ferromagnetism at room temperature. They argue that the oxide layer in between the metallic cores suppress the particle interaction, leading to

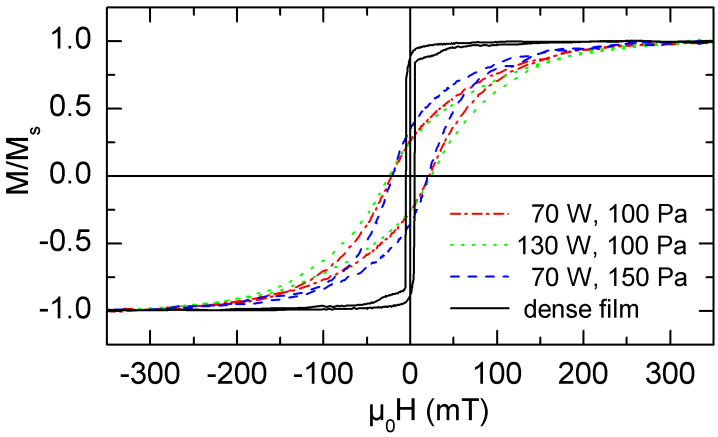

FIG. 4.11: Hysteresis loops at room temperature of three Co nanoparticle films and a conventionally sputtered film for reference. The cluster films are magnetically harder than the dense film with $H_{\mathrm{C,cluster}} = 4.5 H_{\mathrm{C,dense}}$. From Gojdka et al.[136].

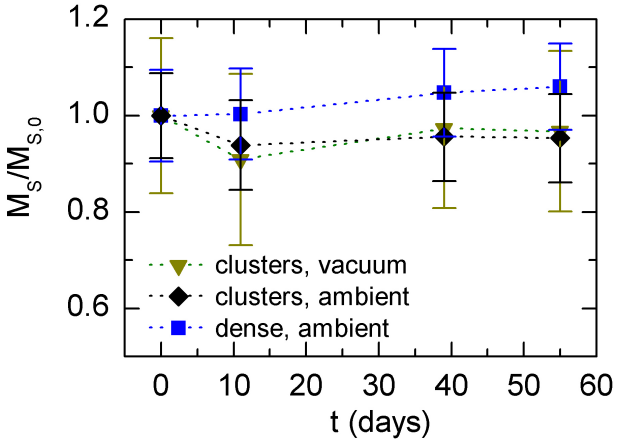

FIG. 4.12: Evolution of saturation magnetization M_{S} for two Co nanoparticle deposits and a dense Co film. $M_{\mathrm{S,0}}$ denotes M_{S} of each sample at the start of the measurement series. From Gojdka et al.[136].

superparamagnetism. Thus, in the present work, the presence of ferromagnetism in cluster films at room temperature is strong evidence that the CoO layer forms at the point of exposure to ambient conditions and not during the deposition process. This is in accordance with the TEM study of a particle agglomerate in Fig. 4.7.

The measured coercivity is constant for different deposition parameters as depicted in Fig. 4.11. This reflects the nearly identical size-distributions of the individual particles for different deposition conditions, since similar particle ensembles will form microstructures with similar interparticle coupling.

Finally, the long-term stability of the saturation magnetization of the nanoparticle films under ambient conditions was studied due to its importance for possible technical applications. Between the different VSM measurements one sample was stored in vacuum below 1×10^{-5} Pa. The second sample was stored under ambient conditions ($T \approx 293$ K, approximately 40 % relative humidity), accompanied by a dense Co film for reference. As shown in Fig. 4.12 a drop of 5–10 % in saturation magnetization M_S - still within error margins - is observed for both cluster films compared to the dense film during the first 10 days. No further decrease of M_S was observed within the measurement accuracy in the course of two months, demonstrating the chemical stability of the nanoparticle films under ambient conditions.

Since in the following chapter AlN/Co nanocomposites are produced with deposition durations of $t = 20$–70 min, the stability of the GAS deposition rate is investigated. The evolution of the deposition rate without prior bake-out of the GAS is depicted in Fig. 4.13(a). As can clearly be seen, the rate decreases with time. To gain further insight into this effect, the experiment was repeated with a baked-out GAS (14 hrs, $T = 120\,^{\circ}$C). In this case, only for approximately 30 s a non-zero deposition rate is observed and no further rate is detected as shown in Fig. 4.13(b). Upon the addition of minute amounts of N_2 into the GAS, the rate significantly increases. The deposition rate reaches its maximum at $\Phi_{N_2,GAS} = 0.2$ SCCM which, at an Ar flow of $\Phi_{Ar,GAS} = 100$ SCCM, corresponds to only 0.2 % of the total process gas flow. The same trends have been observed for Ti and O_2 admixture in a different study conducted within the working group, evidencing rather a general mechanism than a peculiarity of Co.[179]

The observations in Fig. 4.13 suggest that small amounts of reactive gas are necessary for cluster formation of transition metals in a GAS. In the case of the non-baked-out GAS, O_2 is provided for a certain time during GAS operation by plasma assisted desorption of H_2O from the GAS walls. For the baked-out GAS, this reservoir is not available. However, the surface of a new Co target incorporates a natural oxide layer. This layer provides reactive species during sputtering for a short period of time, explaining the initial deposition burst observed for the baked-out GAS. A possible explanation of the observations is found in Equation (2.33) which describes the bottleneck of cluster growth by the formation of nucleation centers. Both Co-O and Co-N bonds are stronger than Co-Co, as sum-

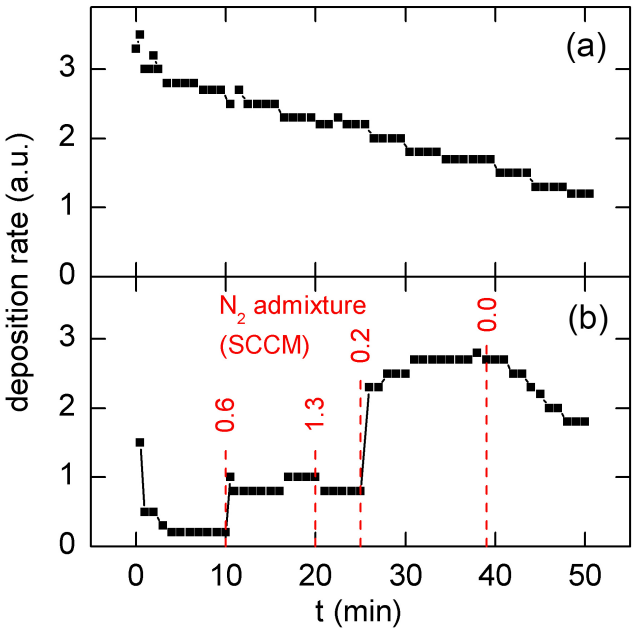

FIG. 4.13: Evolution of GAS deposition rate with time for a new Co target and (a) without bake-out of the GAS, (b) with bake-out prior to deposition and various N_2 admixtures. From Peter et al.[179].

marized in Table 4.3. The same is true for Ti-O and Ti-Ti, respectively. Thus, the compounds can provide stable nucleation sites for the subsequent growth of nanoparticles while the metallic dimers are prone to dissociation in the energetic plasma environment. In accordance with this model, Cu exhibits in other studies a stable GAS deposition rate[180] with the Cu-Cu dissociation energy of 2.083 eV[181] being comparable to 2.168 eV[182] of Co-N. For a detailed investigation of the influence of reactive gas admixture on the cluster formation rate in a GAS refer to Peter et al.[179].

In consideration of the above results, a small admixture $\Phi_{N_2,GAS} \approx 0.2\,\mathrm{SCCM}$ of N_2 was introduced in the GAS during the deposition of AlN/Co nanocomposites in the following chapter. However, considering $\Phi_{N_2,GAS}/\Phi_{Ar,GAS} < 0.2\,\%$ the fraction of CoN in the nanoparticles is expected to be negligible, since only CoN dimers are necessary in order to provide nucleation centers for cluster growth. This expectation is evidenced, on the one hand, by the observed presence of a

Compound	Binding Energy [eV]	Compound	Binding Energy [eV]
Co-Co	<1.316[181]	Ti-Ti	1.219[181]
Co-O	4.118[181]	Ti-O	6.908[181]
Co-N	2.168[182]	Cu-Cu	2.083[181]

Table 4.3: Binding energies of various dimers.

metallic core in Fig. 4.7 for the Co particles deposited without prior bake-out of the GAS. On the other hand, the magnetic properties shown in Fig. 4.11 of Co nanoparticle films indicate that the oxide shell is formed after the deposition of the clusters as has been previously discussed. This indicates that the influence of the low amount of necessary reactive gas in the GAS is negligible regarding the metallic character of the particles. Further proof for the negligibility of the N_2 admixture on the chemical composition of the particles will be established in the following chapter by the magnetic properties of AlN/Co nanocomposites.

In summary, a suitable process for the fabrication of magnetic Co nanoparticles with a GAS was established. An average peak deposition rate of up to 600 nm/min was observed within the investigated field of parameters, mainly influenced by the gas pressure in the cluster source during deposition. It was found that the lateral homogeneity of the deposition rate can be adjusted by the flow of the process gas. The morphology, chemical composition and magnetic properties of individual particles and particle ensembles were investigated. The spherical particles exhibited a narrow size distribution centered at $D \approx 4.8\,\mathrm{nm}$. The narrow size distribution of the individual particles and the high porosity of the nanoparticle films of 74% are potentially interesting properties for technical applications like catalysis and sensors. The nanoparticle films exhibited ferromagnetic behavior at room temperature and are chemically stable under ambient conditions.

With the deposition properties of the GAS characterized and a suitable deposition process for the AlN matrix established, the following chapter explores the fabrication and properties of AlN/Co 0-3 nanocomposites.

Chapter 5

Study of AlN/Co Nanocomposites

The deposition processes of the individual composite constituents were established and the physical properties of the respective deposits were characterized in chapters 4.1 and 4.2. In the first part of this chapter, the combination of the individual deposition processes for the design of 0-3 nanocomposites is studied. The resulting quasi-co-sputtering concept is subsequently used to deposit AlN/Co 0-3 nanocomposites. The investigation of the latter is subject of the second part of this chapter.

5.1 Versatile Deposition Concept for 0-3 Nanocomposites

In the following, a deposition concept is presented which combines the advanced particle control of a cluster source with the versatility of conventional magnetron sputtering. The concept has been published in an article by Gojdka et al.[160] and passages of this section 5.1 are excerpts thereof.

On the one hand, a GAS provides advanced control on cluster formation, delivering a defined size distribution which is independent of the surface energy and deposition parameters of the matrix. The separation of the process atmospheres for nanoparticle formation and matrix deposition is advantageous for reactive nanoparticle materials like magnetic metals and alloys. In addition the filling factor and the filling factor gradient can be adjusted with a GAS via the lateral focusing effect of the gas flow as investigated in chapter 4.2. Thus, the separation of the cluster formation process and matrix deposition provides precise process control.

For the matrix, on the other hand, conventional magnetron sputtering is a well established technique capable of depositing metals, oxides, nitrides and polymers. Thus, a combination of GAS and conventional magnetron sputtering potentially enables the tailoring of a wide range of 0-3 nanocomposites.

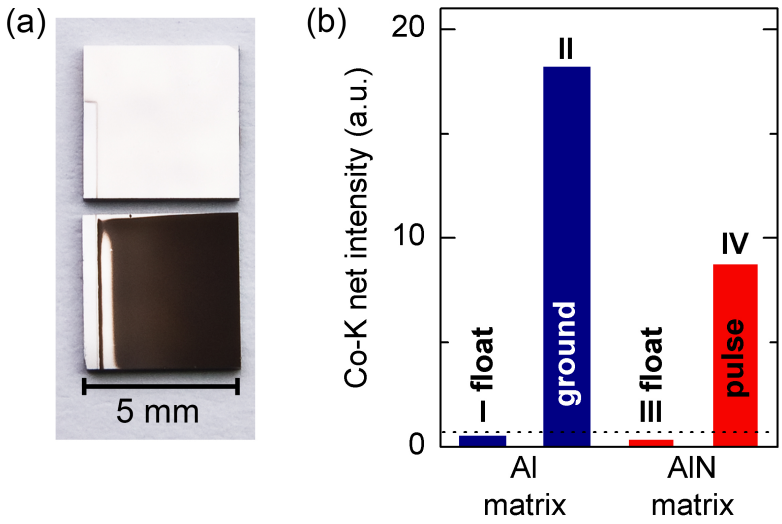

FIG. 5.1: (a) Photographs of identical pieces of platinized Si substrate, attached directly adjacent on the sample holder during deposition of Al/Co composite. Top: sample floating, bottom: sample grounded. (b) EDX net intensity of the Co-K line. Al/Co (blue) with sample floating (I) and grounded (II), respectively, and AlN/Co (red) floating (III) and quasi-co-sputtered (IV). Dotted line: Co-K intensity of pristine substrate for reference. From Gojdka et al.[160].

To demonstrate the functionality of the concept, 0-3 nanocomposites consisting of a reactively sputtered dielectric matrix of aluminum nitride (AlN) and magnetic cobalt (Co) nanoparticles were deposited and characterized. The suitability of the materials for the proof-of-principle investigation was discussed in chapter 2.3.3.

Since the cluster beam passes the plasma of the matrix deposition, the influence of electrical charging on the process was investigated. First, Co nanoparticles were simultaneously co-deposited with Al in order to ensure electrical conductivity throughout the deposit. One piece of substrate was electrically connected to the grounded substrate holder. Directly adjacent, an identical piece was attached electrically insulated to the holder. Hence, during the deposition one composite film was permanently on ground potential, while the other one was on floating potential $U_{\mathrm{fl}} \approx -21\,\mathrm{V}$ with respect to ground. The resulting deposits displayed in Fig. 5.1(a) clearly differ even to the naked eye: the floating one appears to be pure Al while the grounded one incorporates Co clusters which appear dark. Accordingly, the floating sample exhibits no increase of the EDX Co-K signal in Fig. 5.1(b),I relative to the pristine substrate, confirming that no Co was deposited. On the other hand, EDX clearly indicates the presence of Co in the electrically grounded sample (Fig. 5.1(b),II) which was prepared under otherwise identical conditions. This observation corroborates that the incoming Co nanoparticles are repelled from the sample surface due to electrical charging. As described in chapter 2.4.1, the Co particles charge electrically as they enter the

plasma in front of the sample. If the substrate, too, is on floating potential, the charged particles are repelled and hence do not reach the substrate surface. This holds as well for pulsed dc magnetron operation; considering a distance of approximately 5 cm from plasma entry to substrate and a cluster speed of 30–200 m/s[143,149] the time-of-flight of the particles within the plasma region is in the order of 1 ms. Considering further pulsed dc magnetron sputtering with $f_{dc} \approx 50$ kHz and 70 % duty cycle, the off-times of the matrix deposition plasma is in the order of 1 μs.

Thus, composites cannot be fabricated by co-sputtering with preformed clusters if a self-biasing of the film due to the presence of a plasma cannot be avoided. Examples are a highly insulating composite or desired application of a rf-bias[164] which requires the substrate holder to float electrically. For demonstration, the co-deposition of an AlN matrix and Co nanoparticles on an electrically floating substrate was attempted. Again, EDX confirms the absence of Co in the sample as shown in Fig. 5.1(b),III.

Hence a quasi-co-sputtering concept is established in the course of this work in order to benefit from the GAS for the fabrication of composites even when the deposit is electrically floating. To avoid repulsion of the incoming clusters, the sputter-deposition of the matrix is periodically interrupted in low-frequency pulses f_p while the cluster source is operating continuously. During the off-times of the matrix deposition, neither substrate nor nanoparticles are being charged by a plasma, allowing the clusters to reach the substrate. The amount of clusters arriving at the substrate, and hence the filling factor of the composite, can be adjusted via the duty cycle of the low frequency pulsing. In addition, the spatial homogeneity of the film can be tuned by the interruption frequency f_p of the matrix deposition: if f_p is low so that on- and off-times are long compared to the deposition rate of the matrix, a more laminar composite structure is generated. Accordingly, comparatively high values of f_p result in a homogeneous particle distribution.

In the following, the proposed concept of quasi-co-sputtering is demonstrated experimentally for the system AlN/Co. The composite was deposited with identical operation parameters as were used for the AlN/Co composite in which no Co was found previously (Fig. 5.1(b),III). However, the AlN matrix was not deposited continuously but pulsed at $f_p = 0.3$ Hz and 50 % duty cycle according to the proposed scheme. As shown in Fig. 5.1(b),IV EDX verifies the presence of Co in this deposit. The EDX Co-K net intensity of the AlN/Co composite ($I_{AlN/Co} = 8.9$ a.u.) corresponds to about half of the intensity of the grounded Al/Co composite ($I_{Al/Co} = 18.3$ a.u.), in good agreement with the pulsing duty cycle of 50 % used for the quasi-co-sputtering deposition of the AlN/Co sample. Thus, the filling factor of the composite can be adjusted via the duty cycle of the matrix deposition without the need to change any other deposition parameter. In former investigations of co-sputtered AlN/Co composites, without a cluster source, no ferromagnetism could be observed in the as-prepared films

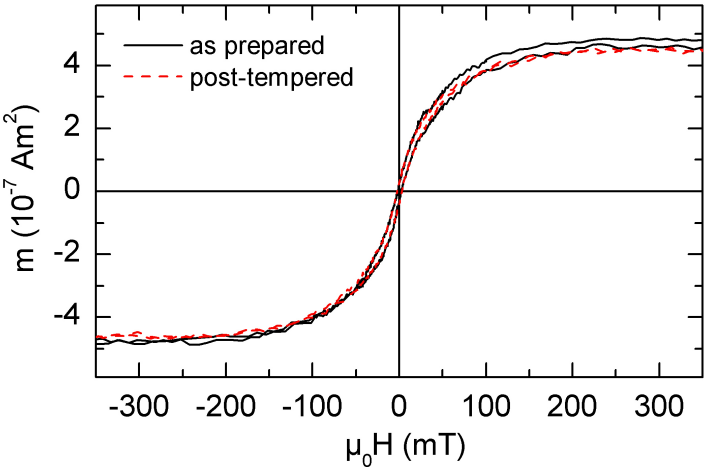

FIG. 5.2: Hysteresis loop of AlN/Co 0-3 nanocomposites prepared by quasi-co-sputtering. As-deposited and post-tempered samples exhibit virtually identical loops. Magnetic moment m is used instead of magnetization M in order to avoid the uncertainty in magnetic volume. From Gojdka et al.[160].

due to the formation of CoN in the reactive process atmosphere.[43,183] In contrast, already the as-prepared AlN/Co 0-3 nanocomposites produced by quasi-co-sputtering with a GAS exhibit ferromagnetism as shown in Fig. 5.2. *In-situ* tempering of the composites for 1 hr at 500 °C does not influence the hysteresis loop. This indicates that the embedded Co nanoparticles are metallic at least for the most part, since Co_xN_y would have been reduced to Co during the tempering process (cf. chapter 2.3.3).[43,93] This demonstrates the advantage of the established deposition concept with preformed magnetic nanoparticles in a reactive process atmosphere. The AlN/Co composites exhibit a saturation magnetization $M_S/M_{S,bulk} = 0.5 \pm 0.2$. While the determination of the absolute saturation magnetization is limited by the uncertainty of the magnetic volume and the VSM instrument calibration, the finding is in good agreement with other reports on M_S of Co nanoparticles.[39] The coercive field of $H_C = (25 \pm 5)$ Oe is 4.8 times lower than H_C previously observed for the nanoparticulate films without matrix (cf. chapter 4.2). The decrease indicates a reduced interparticle interaction due to the separating matrix. Accordingly, the magnetic behavior shifts closer to superparamagnetism as is expected for Co particles of 5 nm diameter at room temperature (cf. chapters 2.1.3 and 2.3.2).

The morphology and chemical composition of quasi-co-sputtered composites was investigated by TEM. First, only AlN was deposited (300 nm) then quasi-co-sputtering was applied in order to produce AlN/Co nanocomposite (450 nm). Finally, only AlN was sputtered again (150 nm). In Fig. 5.3(a) the HAADF STEM Z-contrast image of a cross sectional view confirms that the composite region is uniformly nanogranular, demonstrating the capability of the concept to produce homogeneous nanocomposites. At higher magnification, displayed in Fig. 5.3(b),

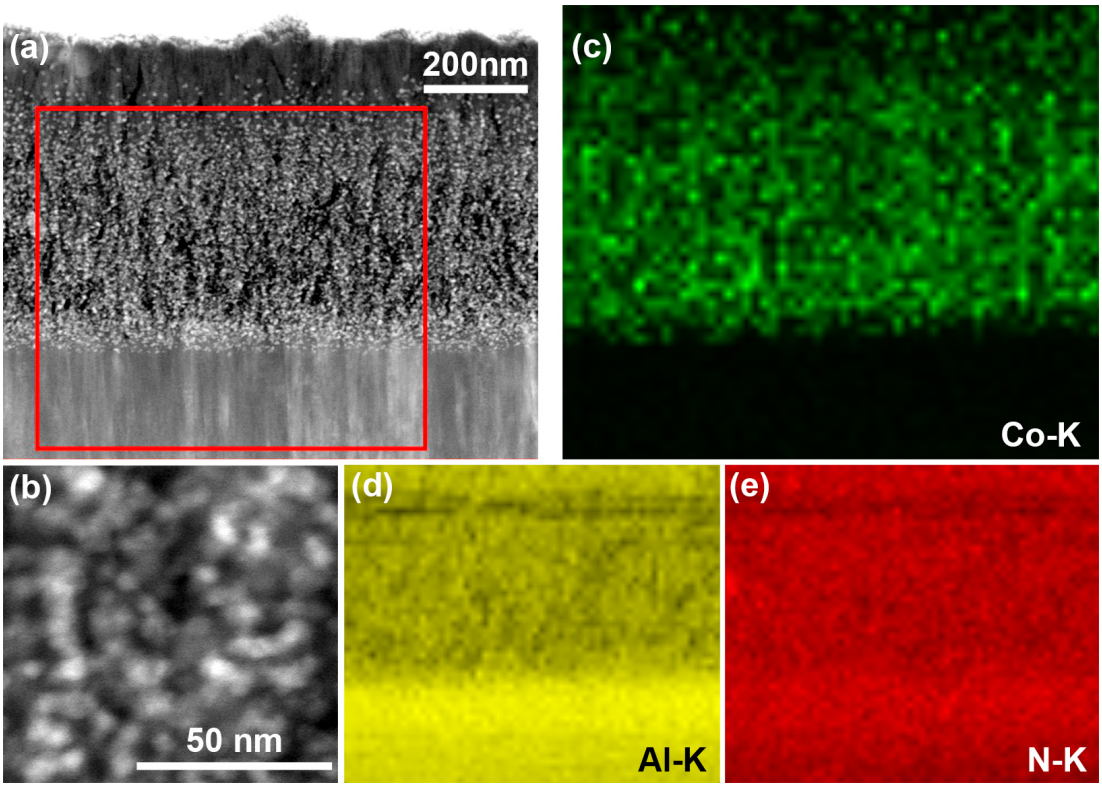

FIG. 5.3: (a) Cross-section HAADF STEM Z-contrast image of AlN/Co composite deposited by quasi-co-sputtering. After initial deposition of pure AlN (bottom), quasi-co-sputtering is applied, resulting in a homogeneous distribution of Co nanoparticles in the AlN matrix. Red frame: area of EDX maps (c)-(e), which correspond to the Co-K, Al-K and N-K lines, respectively. From Gojdka et al.[160].

the diameter of the individual Co nanoparticles can be estimated at about 5 nm. This is in good agreement with the particle characterization of chapter 4.2.

Chemical analysis performed via STEM-EDX of the marked area in Fig. 5.3(a) reveals that the bright contrast spots are indeed Co nanoparticles (Fig. 5.3(c)) embedded within an AlN matrix (Fig. 5.3(d) and (e)). Analyses of individual Co particles confirm their metallic character and exclude the presence of oxygen as shown in Fig. 5.4.

It was demonstrated that Co nanoparticles formed in a GAS do not reach the substrate during the co-sputtering of composites if the substrate is on floating potential. This effect has been discussed in terms of electrical charging of the particles and the substrate in the plasma in front of the substrate surface. The concept of quasi-co-sputtering was proposed and demonstrated for a nanogranular composite consisting of a dielectric AlN matrix with embedded magnetic Co nanoparticles. The structure of the composite was investigated and a homogeneous distribution of the Co nanoparticles was verified. The filling factor of the composite could be adjusted via the duty cycle of the matrix deposition. In ad-

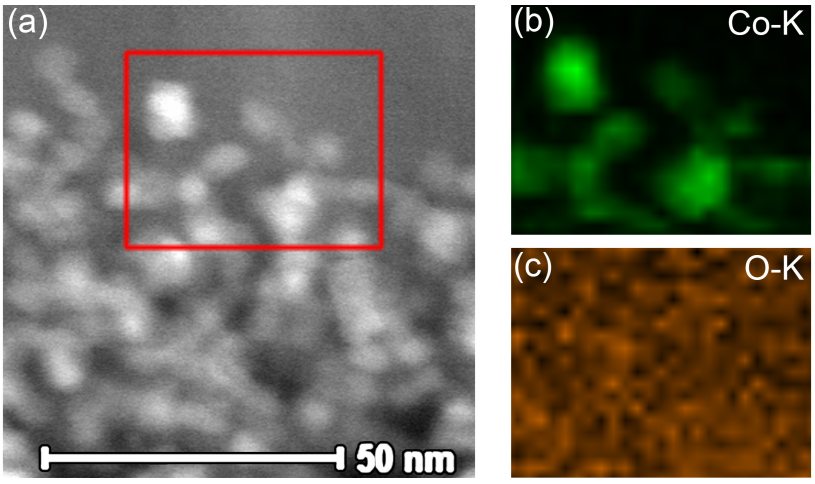

FIG. 5.4: (a) STEM Z-contrast image of individual clusters in the composite. (b), (c) Elemental maps of the area in (a) corresponding to the Co-K and O-K lines, respectively. From Gojdka et al.[160].

dition, already the as-prepared composites exhibited ferromagnetism, evidencing a higher robustness of preformed nanoparticles in reactive process atmospheres. Thus, the concept of quasi-co-sputtering with a cluster source opens up a versatile route for the precise tailoring of a wide range of functional nanocomposites.

5.2 Investigation of AlN/Co Composites

With the concept of quasi-co-sputtering, AlN/Co 0-3 nanocomposites were deposited and characterized regarding their suitability as ME and high-k materials. Passages of this section 5.2 are excerpted from a respective publication by Gojdka et al.[55].

5.2.1 Morphology

First, the influence of embedded nanoparticles on the matrix orientation is investigated. Pure AlN films, examined in chapter 4.1, serve as a benchmark system for the AlN/Co composites. As was summarized in Table 4.2, the pure AlN films exhibit a piezoelectric coefficient $d_{33} \approx 5\,\mathrm{pm/V}$ and a relative permittivity of $\varepsilon_r = 10 \pm 0.6$ in good accordance with typical values for high-quality AlN.[73,74] In the following, the influence of additionally embedded nanoparticles on the structure of the AlN matrix is studied.

Upon deposition of pure AlN, c-axis orientation is achieved already at the beginning of the growth on the Pt/Si substrate as observed in the TEM investigations in Fig. 5.5. Furthermore, the XRD results in Fig. 5.6(a) confirm exclusive c-axis orientation of the pure AlN deposit, with a rocking curve FWHM

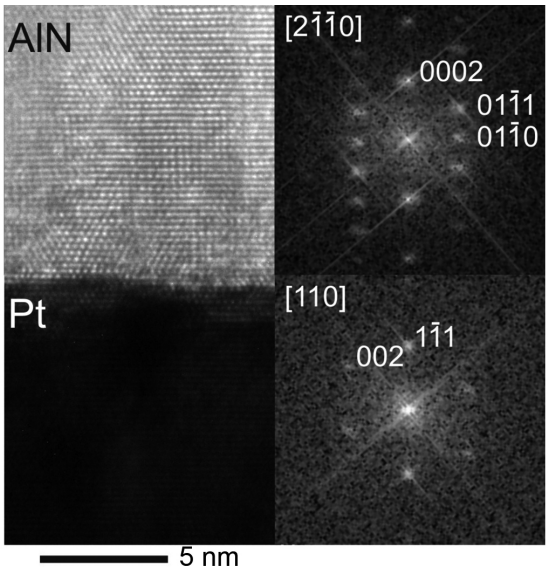

FIG. 5.5: (a) HRTEM micrograph and (b) respective Fourier transforms of AlN on Pt, exhibiting immediate c-axis orientation of the AlN deposit. From Gojdka et al.[55].

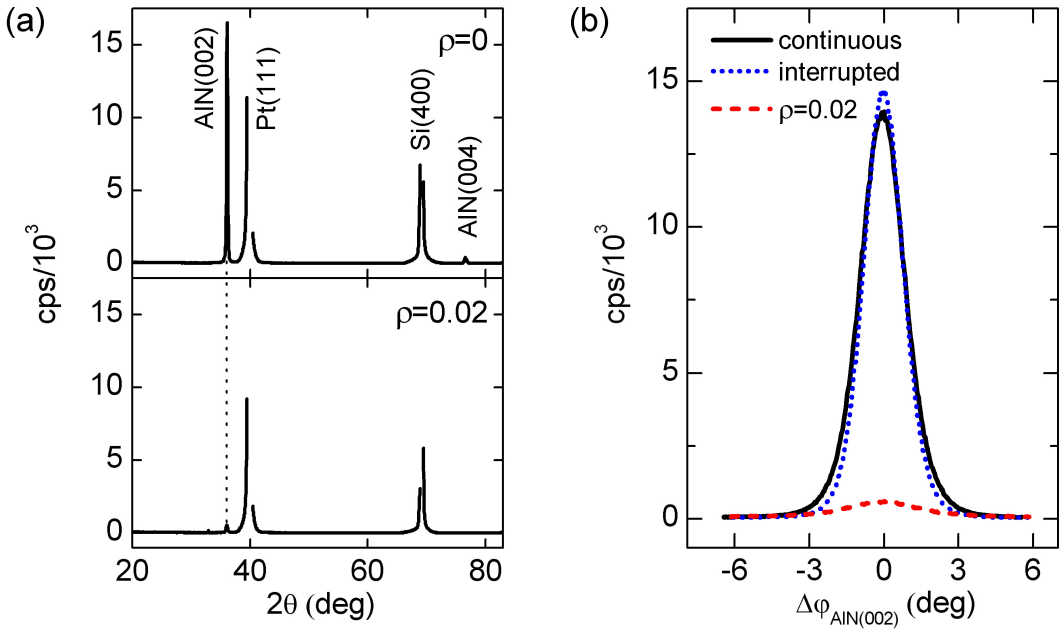

FIG. 5.6: (a) Top: XRD 2θ-scan of exclusively c-axis oriented pure AlN (substrate peaks are omitted due to detector limitations), bottom: AlN/Co composite with $\rho = 0.02$, prepared with the same procedure as the pure AlN deposit. (b) XRD rocking curves of AlN deposited continuously (black, solid), periodically interrupted (dotted, blue) and with embedded Co particles, $\rho = 0.02$ (dashed, red). From Gojdka et al.[55].

of 2° as shown in Fig. 5.6(b). In a next step the matrix deposition is periodically interrupted as part of the quasi-co-sputtering scheme described in the previous section. Pure AlN deposited in this manner exhibits values of d_{33}, ε_r and FWHM, cf. Fig. 5.6(b), comparable to the continuously sputtered AlN film. Thus, the interruptions of the quasi-co-sputtering concept do not degrade the matrix quality.

Subsequently, the very same deposition procedure is conducted with operating GAS, adding Co nanoparticles to the matrix. A 15 nm thick seed layer of pure AlN is deposited prior to the introduction of the Co clusters to ensure optimal growth conditions for the composite. Already for a Co filling factor $\rho = 0.02$ the AlN c-axis orientation, which directly correlates with the piezoelectric properties,[73] vanishes as depicted in Figs. 5.6(b) and (c). The residual intensity of 500 cps observed at the AlN(002) position for the AlN/Co sample corresponds to 1/30 of the intensity of the pure AlN film and thus originates from the AlN seed layer which accounts for 1/30 of the film thickness. No Co diffraction peaks are observed in Fig. 5.6(c) due to the nanoparticle size as was already discussed in chapter 4.2.

The influence of the particles on the matrix crystallinity was further investi-

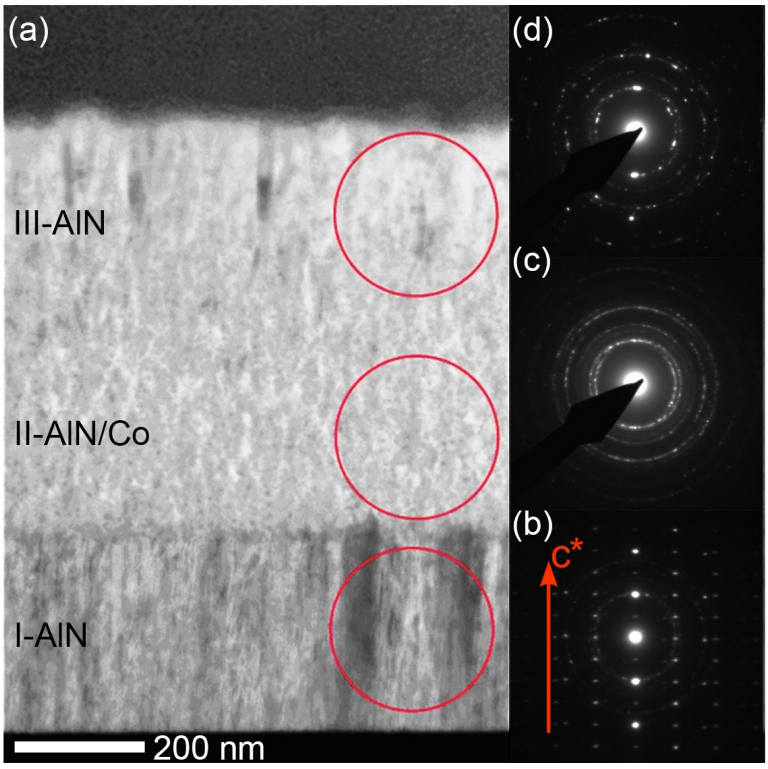

FIG. 5.7: (a) TEM bright field image recorded on a cross-section of an AlN/Co trilayer consisting of 300 nm AlN - 450 nm [AlN/Co] - 150 nm AlN deposited on Pt(111). (b)–(d) respective SAED patterns from the circled areas of (a), see text for details. From Gojdka et al.[55].

gated in detail in the trilayered system, the chemical composition of which was studied in the previous section (cf. Fig. 5.3). The different sample layers are shown in the cross-sectional view of Fig. 5.7(a). In Fig. 5.7(b)–(d) selected area electron diffraction (SAED) patterns corresponding to the different regions reveal the local sample morphology.[g] The SAED pattern in Fig. 5.7(b) confirms the strict c-axis orientation of the pure AlN in region I, in accordance with the previously discussed XRD data. As soon as Co clusters are incorporated (region II) the AlN matrix exhibits an almost total loss of the texture and shows polycrystalline character in the SAED pattern of Fig. 5.7(c). Upon deposition of pure AlN in region III, the matrix regains a stronger (002) texture, as indicated by the strong intensity peaks along c* in Fig. 5.7(d), although to a much lower extent compared to region I. The imperfect orientation of the AlN grains in region III likely results from the fact that the prior AlN/Co deposit is not as good a seed layer as the initial Pt(111) substrate. Variation of deposition parameters does not improve the AlN matrix orientation. It also seems unlikely that a different choice of substrate would improve the structural properties of the AlN/Co composites since the Pt-Si substrate offers excellent growth conditions, yielding highly c-axis oriented pure AlN films. To conclude, the morphological study evidences that the embedded nanoparticles strongly perturb the oriented growth of the matrix and result in an almost total loss of matrix texture.

5.2.2 Electrical Properties

In the following the dielectric properties of the AlN/Co 0-3 nanocomposites relevant for high-k and ME materials are characterized with respect to the Co filling factor ρ.

Figure 5.8 depicts ε_r of AlN/Co composite versus Co volume fraction ρ exhibiting a pronounced increase of $\varepsilon_r(0.15)/\varepsilon_r(0) = 32$. A curve fit according to Equation (2.16) with a percolation threshold of $\rho_C = 0.16$ yields $q = 1.2$ which is in good agreement with classical percolation theory[49] and former reports on ceramic/metal 0-3 high-k materials[53].

Apart from ε_r, a pronounced increase of $\tan\delta$ with ρ is observed in Fig. 5.9 over several orders of magnitude. Starting at $\tan\delta = 4.5 \times 10^{-3}$ for pure AlN, losses reach $\tan\delta > 1$ for $\rho \to \rho_C \approx 0.16$. In contrast, works on bulk 0-3 high-k cermets with larger metallic particles report only a moderate increase of $\tan\delta$ below one order of magnitude.[8,47,53] Smaller grains introduce more grain boundaries which can result in higher dielectric relaxation losses (cf. chapter 2.2.1).[47] In addition, small nanoparticles might be disadvantageous for a composite with respect to $\tan\delta$ as smaller distances between nanoparticles might promote interparticle electron tunneling, in turn resulting in higher dielectric losses.[8] Panda et al.[185] compared percolative 0-3 composites consisting of a PVDF matrix and

[g] A detailed discussion of the SAED data is given in the PhD thesis of Hrkac[184]

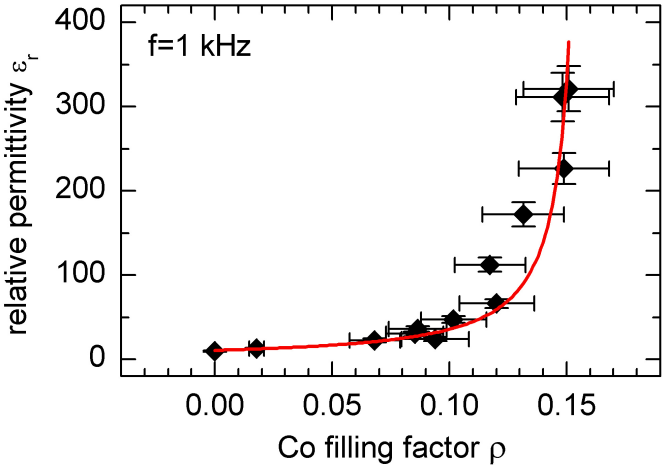

FIG. 5.8: Increase of ε_r with Co content of nanogranular AlN/Co composite. Red line: fit of ε_r according to Equation (2.16). From Gojdka et al.[55].

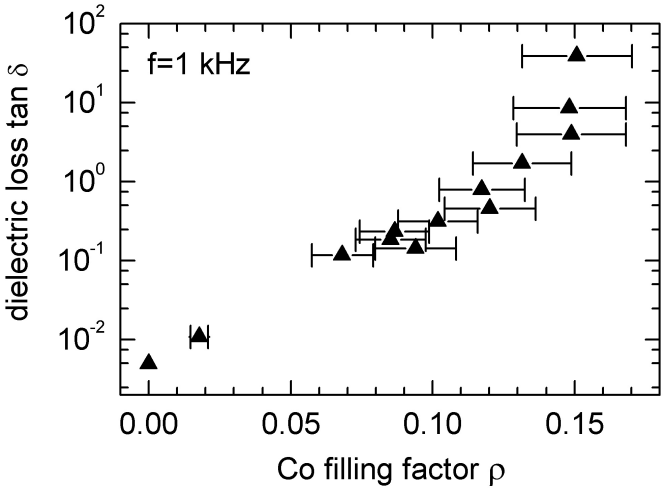

FIG. 5.9: Dielectric loss $\tan\delta$ of AlN/Co composite versus Co filling factor. From Gojdka et al.[55].

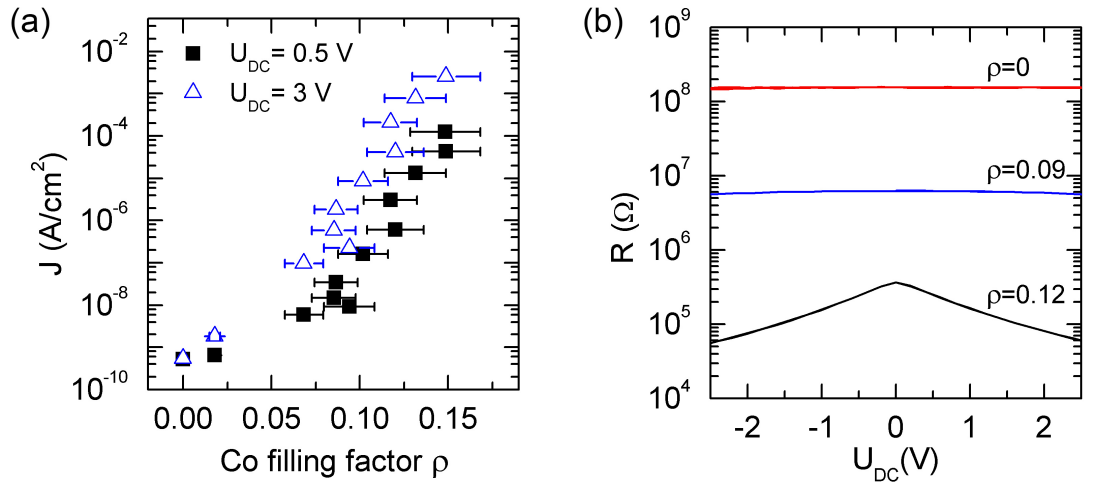

FIG. 5.10: (a) Leakage current density J versus filling factor ρ for $U_{\mathrm{dc}} = 0.5\,\mathrm{V}$ (black squares) and 3 V (blue triangles), respectively. (b) Composite resistance R with respect to U_{dc} for different filling factors.

Ni particles of $D = 20\,\mu\mathrm{m}$ and $D \approx 20\,\mathrm{nm}$ diameter, respectively. In accordance with the above discussion, they reported increased leakage currents for the smaller particles which they as well attributed to increased tunneling probability. On the other hand, they found an increased enhancement of $\varepsilon_r(20\,\mathrm{nm})/\varepsilon_r(20\,\mu\mathrm{m}) \approx 2$ in the low-frequency regime and reasoned that the larger interface area between matrix and smaller particles gives rise to the more pronounced raise of ε_r. Thus, there seems to exist an optimum particle size in the nanometer regime which balances the detrimental increase of tunneling leakage and the advantageous increase of particle/matrix interface area.

Leakage current density J increases with filling factor as shown in Fig. 5.10(a) for static voltages of $U_{\mathrm{dc}} = 0.5\,\mathrm{V}$ and 3 V, respectively. Below the percolation threshold, that is $\rho < \rho_{\mathrm{C}} \approx 0.16$, the conductivity of the composite is governed by tunneling between the individual particles which are separated by layers of insulating matrix.[8,186] Accordingly, at higher ρ, an applied bias U_{dc} results in a pronounced increase of tunneling current as displayed in Fig. 5.10(b).

In addition to the experimental investigation of the composite film as a whole, a cooperating research group, headed by M. Gerken, modeled the influence of the conductivity of an individual magnetostrictive particle on the local electric potential of the surrounding matrix by three-dimensional finite element simulations.[55] The electric potential of the matrix, induced via strain by a magnetostrictive sphere upon application of an external magnetic field was studied for two cases as shown in Fig. 5.11. In the first case, the sphere is conductive, with typical parameters of Terfenol-D.[187] In this unit cell, depicted in Fig. 5.11(a), the simulation yields a maximum voltage of $U_{\mathrm{max,cond.}} = 0.48\,\mathrm{a.u.}$ between top and bottom cell surfaces. For the second case, however, the sphere is assumed to be

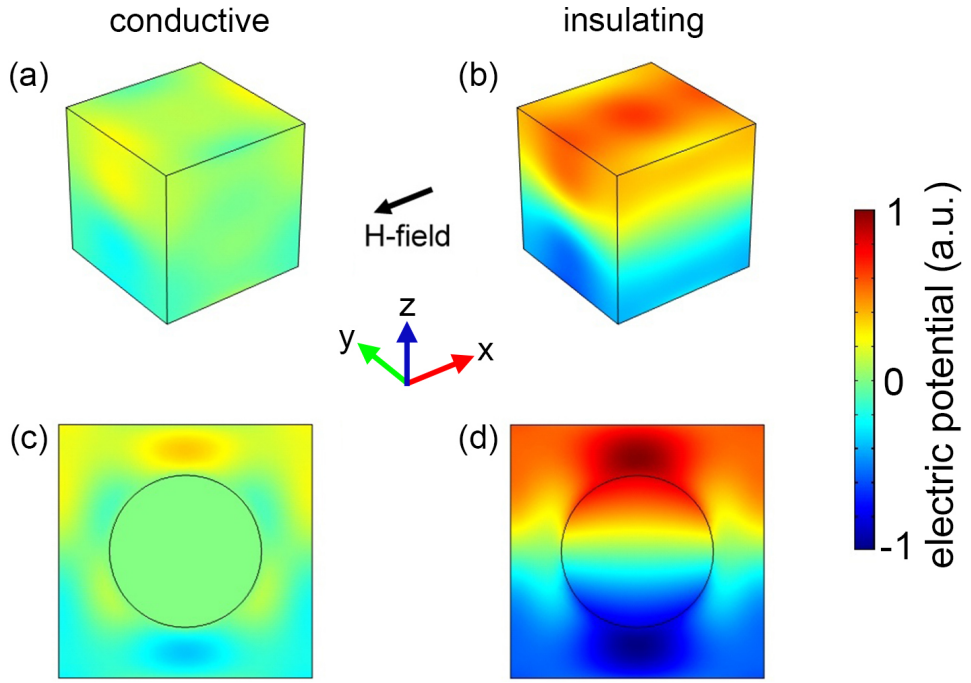

FIG. 5.11: Simulation of the electric potential in a PZT cell containing a Terfenol-D sphere upon application of an external magnetic field for a conductive (a) and an insulating (b) particle. (c), (d) xz-plane cross-sections of (a) and (b), respectively. All graphs are presented in the same scale. After M. Gerken in Gojdka et al.[55].

ideally insulating, with otherwise identical Terfenol-D properties, Fig. 5.11(b). This situation yields a surface potential difference of $U_{\mathrm{max,ins.}} = 1.68\,\mathrm{a.u.}$. Thus the simulation reveals a locally reduced polarization of the matrix in the presence of a conductive, that is metallic, particle. In direct comparison, the voltage drop across the unit cell is $U_{\mathrm{max,ins.}}/U_{\mathrm{max,cond.}} = 3.5$ times higher if the sphere was non-conductive, assuming otherwise identical material properties. Further insight on this effect is provided by cross-sectional views of the xz-plane along the center of the unit cell. Due to the conductivity of the sphere, charges balance within the matrix, resulting in a reduced matrix polarization, Fig. 5.11(c). In the case of an insulating particle, Fig. 5.11(d), a voltage builds up throughout the entire unit cell.

5.2.3 Discussion of Applicability

Magnetoelectric Effect

Considering the dependence of ME output voltage on ε_r, cf. Equation (2.26), the enhancement of ε_r due to the inclusion of metallic particles should be regarded a severe inherent drawback of the 0-3 approach for ME films with metallic particles. Research on 0-3 ME composites has been focused so far mainly on the prevention

of leakage currents for example by fabrication of core-shell nanoparticles with isolating shell.[59,188,189] However, for metallic nanoparticles the core-shell approach cannot suppress the increase of ε_r of the composite with ρ; for example, Xu and Wong[190] embedded self-passivated Al/Al_2O_3 core-shell particles and found a drastic increase of ε_r. Especially when considering the aspect of performance in applications like magnetic field sensors, the increase of $\tan\delta$ with ρ has to be regarded an inherent challenge of the 0-3 approach to ME films with metallic particles. The simulation results evidence that local short circuiting of the matrix, leading to local suppression of matrix polarization, presents a further drawback of the 0-3 approach for ME composites with metallic particles. Finally, the morphological investigations indicate severe degradation of the matrix orientation upon embedding of nanoparticles, diminishing the piezoelectric effect. As a consequence, the calculated optimal filling factor of $\rho = 0.6$[60,62] for ME composites appears not to be feasible from an experimental point of view. In accordance with the presented findings, no ME effect could be measured for various AlN/Co samples.

In the face of the presented results, one might question the ME coefficient presented by Park et al.[68] in the order of $\alpha_{\mathrm{ME}} \approx 150\,\mathrm{mV/(cm\,Oe)}$ for a BTO/Co nanocomposite. Although other works on magnetoelectric effects in 0-3 nanocomposite films with metallic particles exist,[191,192] only Park et al.[68] state a ME voltage coefficient α_{ME} for this class of nanocomposite. As described by Equation (2.25), α_{ME} vanishes for magnetic fields $H > H_{\mathrm{S}}$ above saturation of the magnetostrictive phase since in this case $\partial\lambda/\partial H = 0$. However, according to the data presented by Park et al.[68], the magnetostrictive phase saturates at approximately $H_{\mathrm{S}} \approx 2\,\mathrm{kOe}$ while $\alpha_{\mathrm{ME}} \approx const.$ for $0\,\mathrm{kOe} < H < 6\,\mathrm{kOe}$. In addition, the presented α_{ME} increases monotonously with increasing magnetic field frequency over the whole depicted range from 0 to 100 kHz. Both, dc and ac behavior of α_{ME} suggest that the ME coefficients reported by Park et al.[68] are in fact a measuring artifact at least in big parts (namely the presented α_{ME} for $H > H_{\mathrm{S}}$), likely caused by induction.

In summary, it is questionable whether the 0-3 approach with metallic particles is suitable to produce nanocomposite films with large ME effect.

Percolative High-k 0-3 Nanocomposite

The observed relative increase of $\varepsilon_r(0.15)/\varepsilon_r(0) = 32$ is comparable to works on bulk high-k materials. Existing studies report solely on sintered percolative 0-3 high-k cermets. The presented findings proof the feasibility of PVD-based production of percolative 0-3 high-k nanocomposite films by application of the quasi-co-sputtering concept developed in the course of this thesis. The highest measured absolute value of $\varepsilon_r(0.15) \approx 300$ is orders of magnitude lower than values reported for percolative BTO-based composites which can reach $\varepsilon_r = 10^4$–10^5. Taking into account Equation (2.16), the modest absolute value of $\varepsilon_r(0.15)$ re-

sults from $\varepsilon_r(0) \approx 10$ for the pure AlN matrix. However, as discussed in chapter 2.2.1, already a moderate relative increase leading to comparatively low absolute $\varepsilon_r = 10^1$–10^2 can be of high technological relevance for example in microelectronics.[44,90]

As expected, the dielectric leakage increases with filling factor. In order to further improve the composites, the approach of core-shell particles, as demonstrated for example by Xu and Wong[190] for Al/Al_2O_3 nanoparticles, offers the possibility to suppress leakage currents in a refined 0-3 nanocomposite design. In addition, Xu and Wong[190] found smaller ($D = 40\,\mathrm{nm}$) Al/Al_2O_3 core-shell particles to perform better than larger ones ($D \geq 3\,\mu\mathrm{m}$) in percolative 0-3 high-k nanocomposites. They explained this finding by the formation of a thinner Al_2O_3 shell in smaller particles, allowing the composite geometry to more closely approach the percolation threshold. Taking furthermore into account that Panda et al.[185] found leakage current and ε_r to increase for $D = 20\,\mathrm{nm}$ particles compared to $D = 20\,\mu\mathrm{m}$, a particle size in the nanometer regime seems to exist at which an optimum trade-off between tunneling leakage and increased surface area is achieved. Considering the sparse existing literature on the influence of particle size in 0-3 percolative high-k composites, future studies of the size dependence are definitely required.

The pronounced increase of $\tan\delta$ with ρ certainly poses a challenge for the quality of the investigated AlN/Co deposits as high-k materials. Considering the positive results of other reports on bulk 0-3 high-k cermets, $\tan\delta$ of the deposits can likely be improved by increasing the grain size of the matrix. This should be possible by increasing the nanoparticle size on the one hand and fine adjustment of the deposition parameters on the other hand. Appropriate measures might include the use of core-shell nanoparticles, application of rf-bias and *in-situ* post-tempering of the deposits. An increased grain size of the matrix should effectively reduce relaxation losses at grain boundaries. It should be emphasized that in the case of high-k materials no piezoelectricity and thus no matrix texture is necessary, unlike in ME composites. In addition, no magnetic materials have to be used for the metallic phase. Considering these less strict boundary conditions, the improvement of $\tan\delta$ in sputter-deposited high-k 0-3 nanocomposite films appears feasible.

Part I - Summary and Outlook

In Part I of this work a versatile deposition concept for the precise tailoring of 0-3 nanocomposites was developed. The resulting AlN/Co nanocomposites were investigated regarding their suitability as high-k and magnetoelectric material. Prior to the development of the concept, a new high-vacuum deposition system was designed and constructed in order to meet the experimental needs of the project. The system allows for co-deposition of a wide range of nanocomposites including reactive species like most magnetic materials. The process atmospheres for matrix deposition and cluster formation can be separated by a gas aggregation cluster source (GAS). The various adjustable deposition parameters like sample temperature RT $\leq T_{sample} \leq$ 1000K, electrically floating or grounded sample, variable sample-magnetron distance and various process gas mixtures render the system highly flexible. A load lock enables fast sample transfer and target change at the GAS without the need to break the main vacuum. The high flexibility and capability of the new deposition machine render it suitable for a multitude of future research projects related to nanoparticles and nanocomposites. A promising task would be the refinement of PVD-prepared percolative high-k 0-3 composites. The measures discussed below for optimization of such materials require the precise process control offered by the new PVD system.

Separately deposited AlN films and Co nanoparticles were investigated in order to characterize the individual constituents of the aspired 0-3 nanocomposites. For the composite matrix, a deposition process was established in order to produce exclusively (002)-oriented, piezoelectric AlN. On Pt(111)/Si substrate a FWHM as low as 1.8° was achieved. A piezoelectric coefficient of $d_{33} \approx 5\,\mathrm{pm/V}$ and a relative dielectric permittivity of $\varepsilon_r = 10$ were observed, which are typical values for c-axis oriented AlN of high quality. As this is the first piezoelectric ceramic deposited in the involved research group, the developed process opens up new possibilities for future research projects. For instance, an advanced design of the sensor system presented in Part II of this thesis could include a piezoelectric AlN read-out layer to allow for full integrability.

In order to fabricate magnetic Co nanoparticles in a process atmosphere independent of the main deposition chamber, a self-constructed (GAS) was established and characterized. A highly variable rate up to 600 nm/min and a tunable deposition profile make the GAS a versatile tool for the fabrication of nanoparti-

cles and nanocomposites. TEM studies of the GAS output revealed a mean particle diameter of $\langle D \rangle_{Co} \approx 5\,\mathrm{nm}$ with a very narrow size distribution $\sigma = 0.6$–$0.8\,\mathrm{nm}$. Individual particles exposed to ambient conditions exhibited a core-shell Co-CoO morphology. Nanoparticulate films of several hundred nm thickness exhibited high porosity and ferromagnetic hysteresis at room temperature. The output characteristic and the flexibility of the GAS make it a valuable and versatile tool for the involved research group. Furthermore, Sawa et al.[193] demonstrated the possibility to produce well-dispersed multicomponent nanoparticulate composites with two independent GAS. Thus, considering the well-defined particle size, the high porosity and the compositional flexibility of GAS deposits, the latter could be investigated in prospective research projects regarding their suitability for sensors and catalysis.

After the characterization of the individual components, nanocomposites were deposited by a combination of the individual deposition processes. It was found that the nanoparticles did not reach the substrate surface if the matrix magnetron operated continuously. This observation could be explained by the charging of substrate surface and nanoparticles by the plasma of the matrix magnetron. Thus, in the newly developed scheme of quasi-co-sputtering, the matrix deposition was pulsed in a low-frequency regime of $f_\mathrm{p} \approx 0.3\,\mathrm{Hz}$. This concept of quasi-co-sputtering enabled the successful deposition of magnetic AlN/Co nanocomposites. These were investigated towards their applicability as high-k and magnetoelectric materials.

An increase of ε_r by up to a factor of 30 upon incorporation of the metallic nanoparticles indicates the potential suitability of the concept for the design of high-k materials. In addition, the spherical character of the particles provided by the GAS adds to the reproducibility of the composite properties since irregularities in particle shape are minimized. A challenge is posed by the simultaneous increase of dielectric loss $\tan\delta$. In future works, the 0-3 nanocomposites might be optimized by the use of core-shell nanoparticles in order to suppress leakage currents. Further improvement of $\tan\delta$ should be achievable by a refinement of the matrix microstructure for example by application of a rf-bias during deposition or post-tempering of the composite. So far, granular high-k cermets have been prepared exclusively by sintering of bulk samples. A reproducible, dry and low-temperature PVD thin-film preparation would significantly add to the relevance of high-k cermets for technological application. Thus, upon further refinement, the demonstrated process represents a promising route for the preparation of thin-film high-k cermets.

Regarding the applicability of the AlN/Co composites as magnetoelectric (ME) materials several inherent challenges of the 0-3 approach to ME materials with metallic particles were identified. In addition to the detrimental increase of $\tan\delta$, the observed increase of ε_r as well poses a severe drawback in the context of the ME effect. Even the use of core-shell particles, which are discussed in literature for the inhibition of leakage currents in ME composites, cannot sup-

press the detrimental increase of ε_r. Thus, the latter has to be regarded a severe inherent drawback of the 0-3 approach with metallic particles to ME nanocomposites. Furthermore, finite element simulations indicate a local short-circuiting of the matrix due to the conductivity of a metallic particle. As the simulations evidence, the local electric polarization of the matrix is reduced, leading to a 3.5 times smaller ME voltage in the case of a conductive particle. Apart from the electrical properties, a strong degradation of the matrix orientation was observed with respect to Co filling factor. Already at a filling factor of $\rho = 0.02$ virtually no c-axis orientation of the AlN could be detected anymore, thus frustrating the piezoelectric properties of the matrix. In the face of the presented evidence, the 0-3 nanocomposite approach with metallic particles appears not to be suitable for the design of high-performance ME materials. Accordingly, the ME coefficients reported by Park et al.[68] for a BTO/Co composite are most likely a measuring artifact as experimental contradictions in their report suggest.

The ME study was performed within the framework of the SFB (Collaborative Research Center) 855, which investigates the potential of ME materials for highly sensitive magnetic field sensors especially for the use in biomagnetic applications. Apart from material development, the SFB 855 pursues a multidisciplinary approach in order to improve magnetic field sensing technology. Accordingly, new concepts for ME magnetic field sensors are being explored. Thus, in the context of the SFB 855, a new concept based on a laminar geometry was developed in the course this PhD project. This concept of a novel MEMS magnetic field sensor is subject of the following Part II.

Part II

Novel Magnetic Field Sensor

Chapter 6

Part II - Introduction

Medical applications like magnetocardiography (MCG), magnetoencephalography (MEG), advanced drug delivery and *in-vivo* imaging would significantly profit if the technical requirements of novel magnetic field sensors were less demanding compared to existing systems. Presently, high-sensitivity magnetic field measurements are performed with superconducting quantum interference devices (SQUID)[194,195] which require cooling by liquid helium. The cooling significantly contributes to operational costs and thus impedes the broader medical use of the technique. On the other hand, low-cost room-temperature operation of suitable magnetic field sensors would be of great advantage in numerous medical applications from brain-computer interfaces to improved diagnosis and therapy.[195–197] MCG[198] and MEG[199] measurements were recently demonstrated with chip-scale atomic magnetometers. The SFB 855 "*Magnetoelectric Composites - Future Biomagnetic Interfaces*" pursues a different approach based on ME composite materials. Apart from the design of suitable ME materials, new sensor concepts are developed in multidisciplinary collaborations as part of the SFB 855.

The most advanced ME sensors produced in the SFB 855 are based on a laminar (2-2) cantilever geometry.[200] While the devices achieve in resonance sensitivities unprecedented by other ME sensors, their response drops drastically if the magnetic field frequency does not match the sensor's eigenfrequency.

A novel concept was elaborated in the course of this work[h] in order to enable magnetic field sensing in the whole biomagnetically relevant frequency regime at room-temperature based on a laminar sensor geometry. Using microelectromechanical systems (MEMS), the concept exploits the frequency shift of a mechanically excited cantilever due to the change of Young's modulus of a functional coating upon application of a magnetic field.

Part II is organized as follows. In chapter 7 fundamental theoretical aspects of the novel concept are addressed and related existing concepts for magnetic field sensing are discussed. Subsequently, the experimental setup of the demonstrator

[h] in cooperation with R. Jahns and K. Meurisch

is described in chapter 8. Finally, the experimental proof-of-principle is presented in chapter 9. The concept and its experimental demonstration has been published by Gojdka et al.[201], and passages of Part II are adapted from the respective publication. Furthermore, the work was presented by the journal *Nature* as a research highlight.[202]

Chapter 7

Theory

7.1 Delta-E Effect

The delta-E effect as a consequence of magnetostriction represents a special kind of modulus defect. It describes the dependence of Young's modulus E on the magnetization state of a magnetic material.[203] At fixed magnetization, Young's modulus depends solely on elastic strain

$$E^{\mathrm{M}} = \frac{\sigma}{S_{\mathrm{e}}} \tag{7.1}$$

where superscript M denotes fixed magnetization, σ stress and S_{e} elastic strain. However, a material appears more compliant due to a magnetoelastic contribution S_{m} to strain, leading to an effective modulus

$$E_{\mathrm{eff}} = \frac{\sigma}{S_{\mathrm{e}} + S_{\mathrm{m}}} \tag{7.2}$$

as depicted in Fig. 7.1(a). The resulting delta-E effect

$$\frac{\Delta E}{E} \equiv \frac{E^{\mathrm{M}} - E_{\mathrm{eff}}}{E^{\mathrm{M}}} = \frac{S_{\mathrm{m}}}{S_{\mathrm{e}}} \tag{7.3}$$

can reach several hundred per cent in the small stress regime.[203]

As illustrated in Fig. 7.1(b), Ludwig and Quandt[204] reported for field-annealed amorphous $(Fe_{90}Co_{10})_{78}\,Si_{12}B_{10}$ thin films a change of Young's modulus up to 50 GPa corresponding to approximately $\Delta E/E \approx 30\,\%$. They pointed out that the different contributions to anisotropy K (crystalline K_{c}, shape K_{s}, stress K_σ and induced K_{i}) have to be controlled in order to optimize the delta-E effect since[204,205]

$$\frac{\Delta E}{E} \propto \frac{\lambda_{\mathrm{s}}^2}{K} E^{\mathrm{M}} \qquad \text{, with} \quad K = K_{\mathrm{c}} + K_{\mathrm{s}} + K_\sigma + K_{\mathrm{i}} \qquad . \tag{7.4}$$

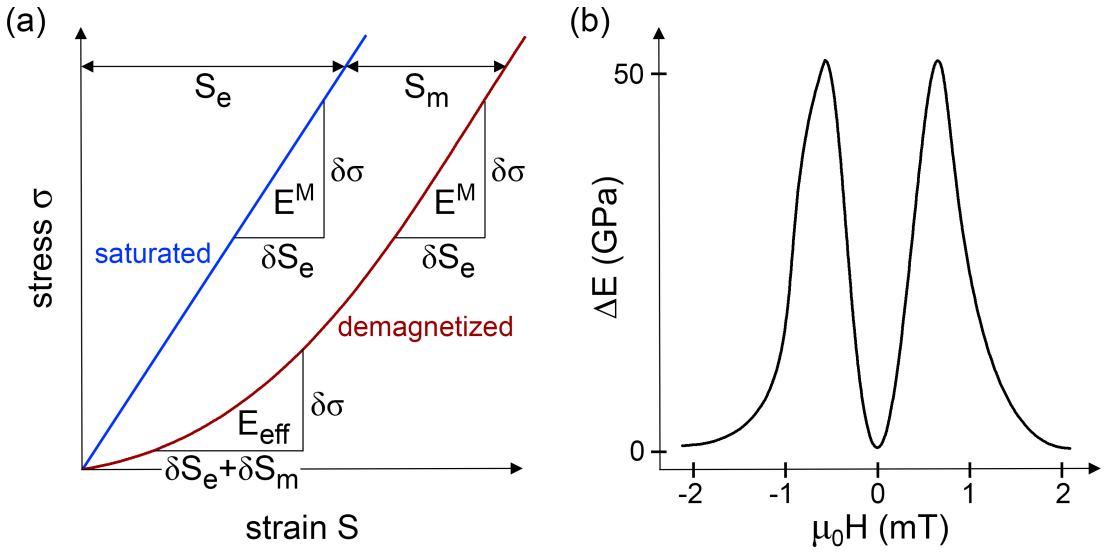

FIG. 7.1: (a) Schematic stress-strain curve for a specimen in magnetic saturation and a demagnetized one. The latter exhibits a modulus defect due to magnetoelastic strain contribution. (b) Generic ΔE curve based on data by Ludwig and Quandt[204] for amorphous $(Fe_{90}Co_{10})_{78}\,Si_{12}B_{10}$ thin films.

Furthermore, a high value of λ_S implies a high magnetoelastic anisotropy since $K_\sigma = 3/2\,\lambda\sigma$.[20] Consequently, post-annealing can increase the delta-E effect of a thin film by optimizing the stress state of the latter. Ludwig and Quandt[204] found annealing-induced tensile stress to enhance the delta-E effect of FeCoSiB thin films.

Apart from stress-optimization, a magnetic field, applied during the annealing and subsequent cool-down, can introduce a uniaxial anisotropy as was first reported by Jones[206]. The resulting magnetic easy axis is oriented parallel to the applied annealing field. The effect was first explained for crystalline alloys by the concept of *directional order*[207] which was later extended to amorphous alloys[208]. During annealing below the Curie temperature, neighboring atoms prefer to orient in the direction of the magnetization, leading to the development of a uniaxial anisotropy as illustrated in Fig. 7.2(a).[209] However, this effect must not be confused with crystallization or clustering, both of which would correspond to a decrease in compositional randomness. Although the pairs of atoms statistically favor the annealing field direction, no long-range order is established by directional order.[210] If the introduced easy axis promotes 90° domain wall motion, magnetostriction λ and as a consequence the delta-E effect is increased compared to the as-deposited state. At the same time the effect is decreased for fields applied in the direction of the induced easy axis (resulting in 180° domain wall motion).

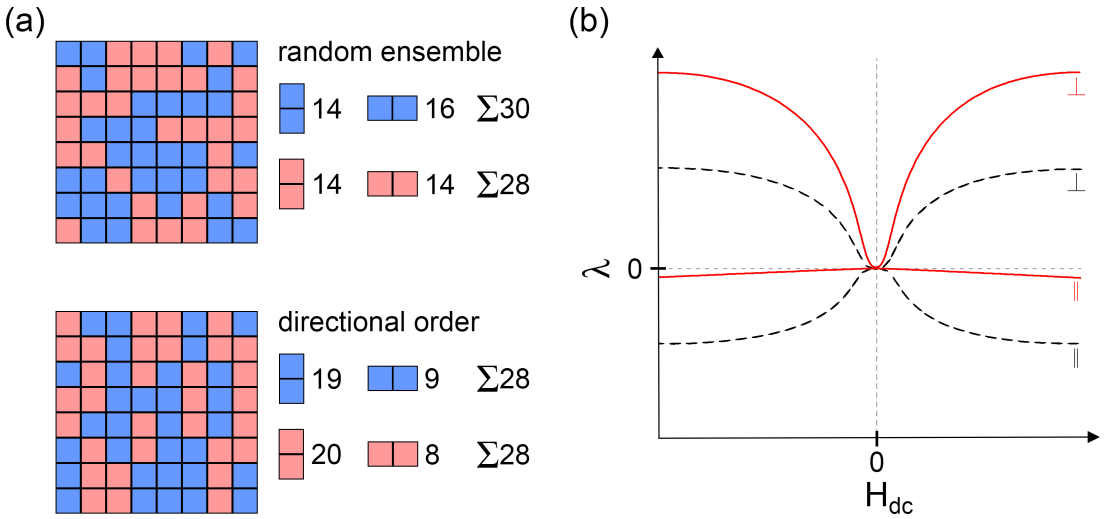

FIG. 7.2: (a) Illustration of directional order in a structure composed of two species of atoms. As the sum of similar neighboring pairs does not change significantly, directional order does not correspond to long-range crystal order or clustering. After Cullity and Graham[211]. (b) Influence of field-annealing on magnetostriction of a FeCoSiB coating on a cantilever beam (generic curve based on data by Greve et al.[200]). Dashed, black: as-deposited; solid, red: after field-annealing. Parallel and perpendicular directions refer to the orientation of the magnetic test field H_{dc} with respect to the induced anisotropy axis.

Thus, by annealing the delta-E effect can on the one hand be increased and on the other hand be made more sensitive to the direction of a magnetic field as illustrated in Fig. 7.2(b). This feature can be exploited to realize vector-field capability in magnetic field sensors.[200]

7.2 MEMS Sensors

In the 1990's the new technology of microelectromechanical systems (MEMS) emerged, based on subsequently developed micromachining techniques.[212] Since then MEMS have been employed in a vast range of applications like pressure sensing[213], flow control[214] and chemical and biological detection[215]. A technically highly relevant subcategory of MEMS are so-called MagMEMS which incorporate magnetic components.[216]

MEMS-based sensors often include a micro-oscillator, the resonance frequency of which is sensitive to the quantity of interest. Accordingly, a change of the latter leads to a shift in resonance frequency of the MEMS oscillator. Readily available micro-cantilevers represent a typical resonant structure for MEMS-sensors. Well-established Si etching techniques offer a precise and low-cost route for the production of such cantilever probes with well-defined spring constant k_0 and

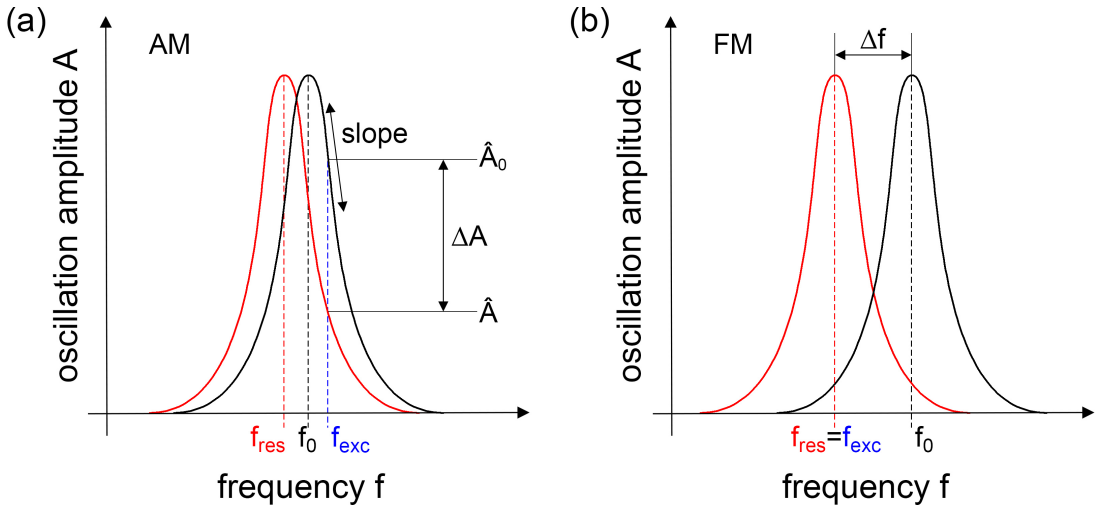

FIG. 7.3: (a) Amplitude modulation (AM) detection scheme. (b) Frequency modulation (FM) detection scheme. Refer to text for details.

resonance frequency f_0. By coating such cantilevers with a functional thin-film, resonant MEMS-based chemical[217–219], biological[220,221] and magnetic[222] sensors have been realized. Commonly, the resonance shift of a microcantilever is detected in two different schemes.[223]

In the *amplitude modulation* (AM) scheme (also referred to as *slope detection*) the oscillator is driven with constant excitation amplitude and frequency $X(t) = \hat{X}\ \sin(2\pi\ f_{\mathrm{exc}}t)$ close to (but not at) its unperturbed resonance frequency f_0, resulting in an oscillation amplitude $\hat{A}_0$ as depicted in Fig. 7.3(a). Consequently, a shift of resonance frequency $f_{\mathrm{res}} = f_0 + \Delta f$ leads to a change in oscillation amplitude $\Delta A = \hat{A} - \hat{A}_0$. Thus, ΔA is a measure of the frequency shift Δf. An important property of an oscillator is its quality factor Q defined as $Q = f_0/df_{\mathrm{FWHM}}$ where df_{FWHM} is the FWHM of the resonance curve $A(f_{\mathrm{exc}})$. High Q-factors correspond to steep resonance curves and thus result in increased sensitivity in the AM scheme. On the other hand the sensor bandwidth is reduced, in the case of very high $Q > 10^4$ to usually unacceptable values.[223] This is a consequence of a slower oscillation adaption to an altered resonance frequency at higher Q-factors.

The second scheme, used for optimized atomic force microscopy[223], locks the excitation frequency to the oscillator's resonance frequency as illustrated in Fig. 7.3(b). Accordingly, this scheme is referred to as *frequency modulation* (FM). A phase-locked-loop (PLL) constantly re-adjusts the excitation frequency to the oscillator's resonance frequency $f_{\mathrm{exc}} = f_{\mathrm{res}}$. Comparison of f_{res} with f_0 directly yields the resonance shift of the oscillator. In the FM-scheme no bandwidth limitations occur due to increasing Q-factor.[223]

Considering the cantilever as a harmonic oscillator, its unperturbed fundamental resonance frequency is given by[224]

$$f_{\mathrm{res}} = \frac{1}{2\pi}\sqrt{\frac{k}{m_{\mathrm{eff}}}} = \frac{1}{2\pi}\sqrt{\frac{1}{m_{\mathrm{eff}}}\frac{b}{4}\left(\frac{h}{L}\right)^3 E_{\mathrm{eff}}} \propto \sqrt{E_{\mathrm{eff}}} \tag{7.5}$$

where b, h and L denote the cantilever width, thickness and length, respectively, k is the effective spring constant ("flexural stiffness") and E_{eff} the effective Young's modulus of the coated cantilever. m_{eff} represents the effective mass of the cantilever which is for the first resonance frequency given by

$$m_{\mathrm{eff}} = \frac{3}{\lambda^4}\left(\rho_1 h_1 b_1 L_1 + \rho_2 h_2 b_1 L_1\right) \tag{7.6}$$

with subscript 1 denoting the cantilever beam and 2 the functional coating. Considering a one-sidedly clamped cantilever, $\lambda \approx 1.875$ holds for the first resonance frequency.[224]

As expressed by Equation (7.5) a variation of E_{eff} shifts f_{res}.[225] Thus an external magnetic field H can be detected by a shift of f_0 exploiting the delta-E effect (cf. chapter 7.1) in a functional magnetostrictive coating of a cantilever.

Yoshizawa et al.[226] reported on an oscillating magnetic field sensor consisting of a quartz resonator with attached FeCoB amorphous ribbons. They deduced for the resonance shift

$$\frac{\Delta f}{f_0} = \frac{1}{2}\frac{d_{\mathrm{m}}}{d_{\mathrm{s}}}\left(3\frac{\Delta E_{\mathrm{m}} + E_{\mathrm{m}}}{E_{\mathrm{s}}} - \frac{\rho_{\mathrm{m}}}{\rho_{\mathrm{s}}}\right) \tag{7.7}$$

where d is the thickness, E Young's modulus and ρ the density of the magnetostrictive phase (subscript m) and substrate (subscript s), respectively. While the sensor was sensitive enough to detect earth's magnetic field, the macroscopic production route was not integrable. Yoshizawa et al.[226] concluded that better results could be expected for a sensor fabricated with thin-film deposition techniques.

A resonant magnetic field sensor design proposed by Osiander et al.[222] features a MEMS cantilever coated with a layer of Terfenol-D. The oscillation of the cantilever is excited by an external magnetic ac field. In their work, the frequency shift of the oscillation is exploited to determine the field strength of static (dc) magnetic fields. However, this approach is not fully integrable due to the required magnetic driving field for the excitation of the oscillation. In addition, the external magnetic excitation field would likely introduce crosstalk in a sensor array for vector field measurements.

The most sensitive ME sensors, developed in the SFB 855[200], exhibit a remarkable sensitivity of $5.4\,\mathrm{pT}/\sqrt{\mathrm{Hz}}$[61] when they are excited by the measured magnetic field itself at their resonance frequency. However, if the frequency of the magnetic field does not match the mechanical eigenfrequency of the oscillator,

the sensitivity decreases by orders of magnitude. Thus, this scheme is restricted to very narrow bandwidth. In addition, the lowest detectable frequency is limited by the mechanical resonance frequency of the cantilever. However, especially low-frequency fields in the range of 0.1–1000 Hz are interesting, for example, in biomagnetic applications[227] or for positioning devices[228]. While a recently proposed modulation technique[229], introducing additional ac magnetic fields, might represent a work-around for the previously mentioned limitations, a different approach is pursued in the following.

In the concept presented in this work, the sensing oscillator is driven mechanically by piezoelectric actuation. Changes in Young's modulus $E(t)$ upon application of measuring fields $H_{\mathrm{ac}} = \hat{H}_{\mathrm{ac}} \sin(2\pi\, f_{\mathrm{H}} t)$ lead to a shift of the resonance frequency f_{res}. Thus, an applied ac magnetic field is transduced in a modulation of the mechanical resonance amplitude of the cantilever and can be detected either in AM or FM mode. Resonators with an unperturbed resonance frequency $f_0 = \mathcal{O}\,(10^2)$ kHz well above the frequency of the measured field enable the oscillation amplitude $\hat{A}$ in the AM scheme to follow the signal. In addition, mechanical noise with typical $f < 5\,\mathrm{kHz} \ll f_0$[230] is rejected due to the high quality factor of the oscillators. This aspect poses a major advantage for the measurement of biomagnetic signals since the latter are in the frequency range $f_{\mathrm{bio}} = 0.1$–$1000\,\mathrm{Hz}$ at which most environmental mechanical noise occurs as well. Due to the sensitivity in the low-frequency regime the concept accesses the whole biomagnetically relevant frequency range and it is potentially fully integrable as there is no need for an external magnetic driving field (in contrast to the design proposed by Osiander et al.[222]). In addition, the concept does not require cooling and possesses vector field capability.

Chapter 8

Experimental Setup

Commercial tipless Si-cantilevers (Nanosensors, TL-NCH) with $f_0 \approx 320\,\mathrm{kHz}$ and $k_0 \approx 42\,\mathrm{N/m}$ were coated with 500 nm of amorphous $(Fe_{90}Co_{10})_{12}Si_{12}B_{10}$ by rf-magnetron sputtering (200 W, 2×10^{-1} Pa Ar) in a commercial sputtering system (Von Ardenne CS 730 S, coating courtesy of H. Greve and E. Quandt). In order to relax film stress the probes were subsequently tempered in vacuum ($p = 10^{-3}$ Pa) at 550 K for 60 min) During the annealing a magnetic field of $\mu_0 H = 0.2\,\mathrm{T}$ was applied to induce an in-plane anisotropy parallel to the long axis of the cantilever. The coated cantilevers were mounted in the standard probe holder of a commercial AFM system (Aist-NT, SmartSPM 1000, provided

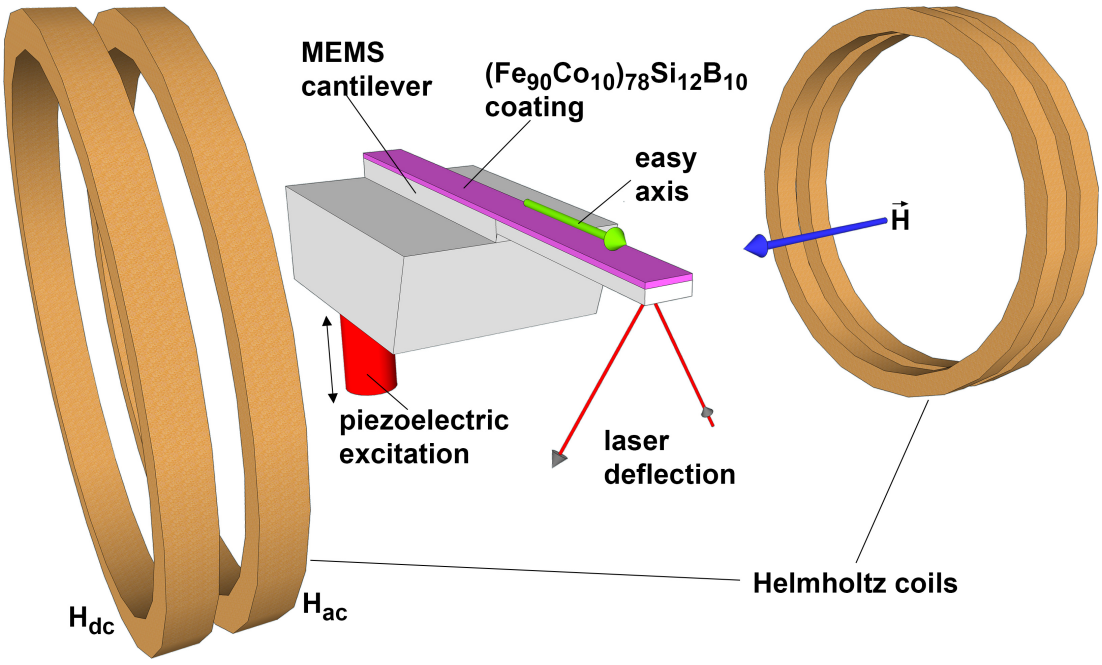

FIG. 8.1: Experimental demonstrator setup based on a MEMS cantilever oscillator coated with 500 nm of amorphous $(Fe_{90}Co_{10})_{78}Si_{12}B_{10}$. See text for details.

by courtesy of H. Kohlstedt). The setup is illustrated in Fig. 8.1.

A pair of Helmholtz coils was arranged within the AFM head around the cantilever to provide an in-plane magnetic test field H_{ac} perpendicular to the long axis of the cantilever. Optionally, an additional magnetic bias field H_{dc} could be applied in order to tune the working point of the magnetostrictive functional layer. The oscillation of the cantilever was excited mechanically via the piezoelectric actuation provided by the AFM system. For the proof-of-principle demonstration the AM detection scheme was chosen since the existing AFM-system supported the respective measurements without any modifications. Accordingly, excitation amplitude and excitation frequency were held constant throughout the experiment. Thus, without an applied magnetic field the cantilever oscillated at a constant amplitude $\hat{A}(t) = \hat{A}_0$. The oscillation was monitored with the laser beam deflection system (PSD) of the AFM.

Chapter 9

Demonstration of Novel Magnetic Field Sensor

The mechanical stress state of the coated and subsequently post-annealed cantilevers was assessed by SEM. A respective image is shown in Fig. 9.1. The coated and post-annealed cantilevers did not exhibit any distortion. The absence of the latter evidences that the FeCoSiB layer is in a low-stress state which is favorable since Ludwig and Quandt[204] found the induced uniaxial anisotropy to vanish for too high stresses. The unbent shape of the beam indicates that the functionalization is not detrimental to the oscillatory properties of the cantilever. Accordingly, the resonance curves of the mechanically excited cantilevers still exhibit a sharp resonance peak within the manufacturers specifications as shown in Fig. 9.2(a) and (b) for an oscillator with an unperturbed resonance frequency of $f_0 = 324.2\,\mathrm{kHz}$ and $Q \approx 230$. In order to exploit the slope of the resonance curve in the AM detection scheme, an excitation frequency $f_{\mathrm{exc}} = 324.8\,\mathrm{kHz} = f_0 + 600\,\mathrm{Hz}$ was chosen for the probe of Fig. 9.2. The unperturbed oscillation amplitude $\hat{A}_0 = const.$ marks the reference level at which $\Delta A = 0$, Fig. 9.3. Upon application of an external magnetic field H_{ac}, the os-

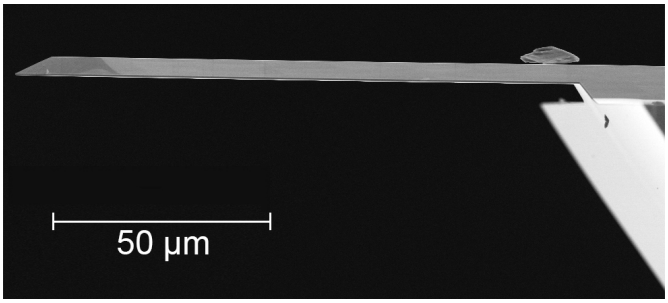

FIG. 9.1: SEM image of a coated and post-annealed MEMS cantilever. The beam exhibits no distortion, evidencing a low-stress state of the FeCoSiB layer. From Gojdka et al.[201].

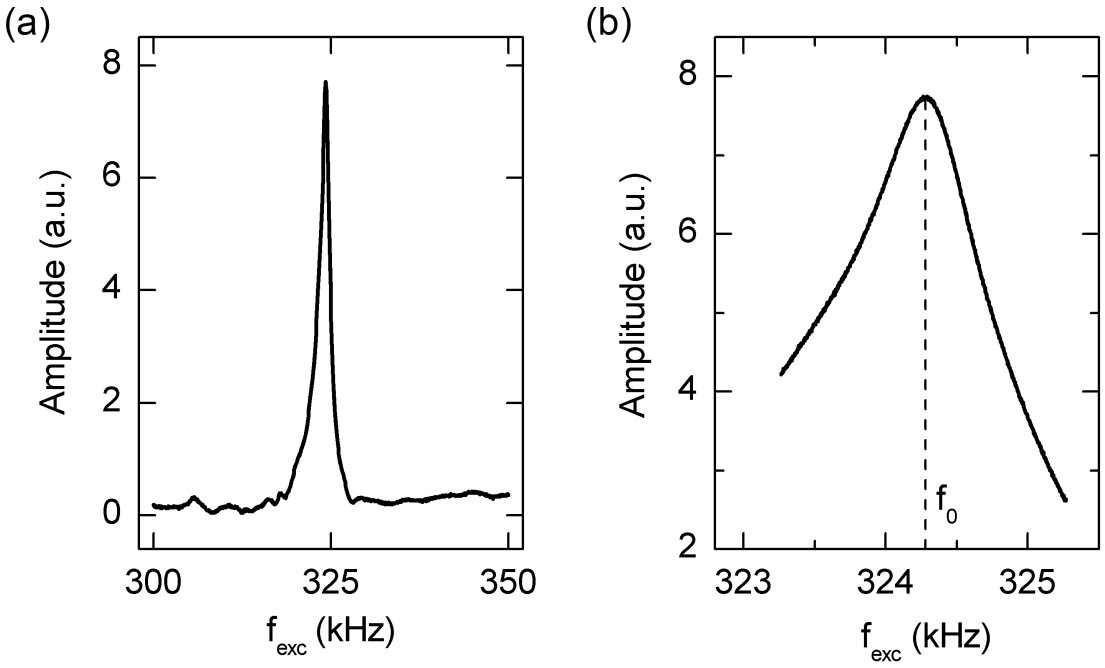

FIG. 9.2: (a) Resonance curve of a prepared cantilever probe. Albeit a coating of 500 nm FeCoSiB the oscillator exhibits a sharp resonance peak. (b) Magnification of the resonance peak.

cillation amplitude of the cantilever is being modulated, leading to $\Delta A(t) \neq 0$. Figure 9.3(a) shows $\Delta A(t)$ for a field $\mu_0 H_{\mathrm{ac}} = 100\,\mu\mathrm{T}$ and $f_{\mathrm{H}} = 15\,\mathrm{Hz}$. If H_{ac} is applied perpendicular to the induced easy axis (EA), maximum 90° domain wall motion is provoked, leading to a significantly larger effect than for application of H_{ac} parallel to the EA. This demonstrates the vector field capability of the presented concept since the sensor output is sensitive to the orientation of applied magnetic fields. However, for a perfect alignment of the magnetic domains along the EA, no modulation should occur if $H_{\mathrm{ac}} \parallel$ EA since in this case only 180° domain wall motion occurs. Thus, future refinement of the sensor design might include optimization of the magnetic domain structure.

The sensor reaches maximum sensitivity when it operates at $\partial E_{\mathrm{eff}}/\partial H = max$, as expressed by Equation (7.5). Ludwig and Quandt[204] reported maximum $\partial E_{\mathrm{eff}}/\partial H$ for $(\mathrm{Fe_{90}Co_{10}})_{78}\,\mathrm{Si_{12}B_{10}}$ thin films at a magnetic field of some $\mu_0 H_{\mathrm{dc}} = 100\,\mu\mathrm{T}$. In good agreement, a magnetic dc bias field $\mu_0 H_{\mathrm{dc}} = 353\,\mu\mathrm{T}$ enhances the sensitivity by up to one order of magnitude, Fig. 9.3(b). The effect does not further increase for $\mu_0 H_{\mathrm{dc}} > 353\,\mu\mathrm{T}$ since maximum $\partial E_{\mathrm{eff}}/\partial H$ is already reached at these fields. Accordingly, for the subsequent experiments a constant bias field of $\mu_0 H_{\mathrm{dc}} = 353\,\mu\mathrm{T}$ is applied. However, it should be noted that H_{dc} is optional and is not a prerequisite for the functionality of the concept. Unlike the design proposed by Osiander et al.[222] no magnetic auxiliary fields are required in the presented concept. In addition, an advanced design of the sensor could be based

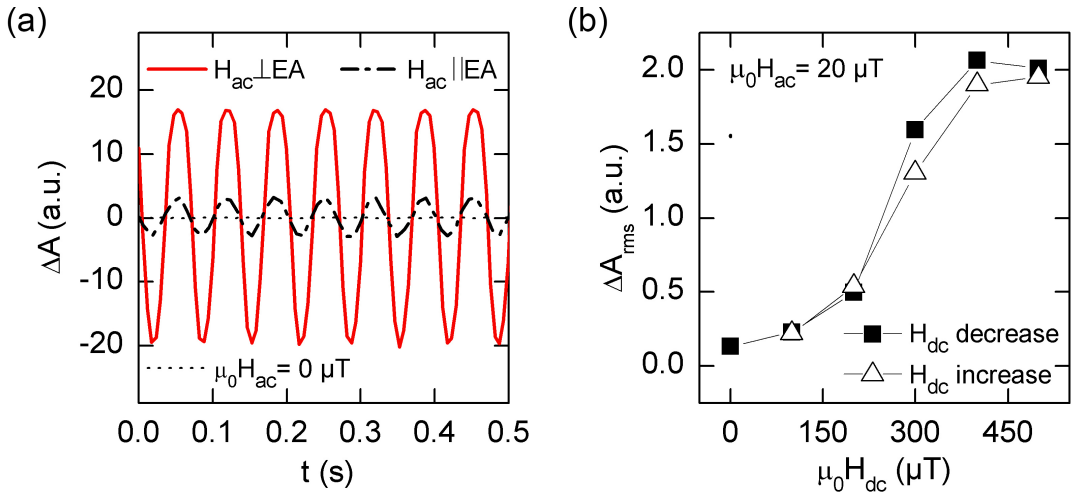

FIG. 9.3: (a) Dotted, black: unperturbed oscillation amplitude at $\mu_0 H_{\mathrm{ac}} = 0\,\mu\mathrm{T}$, marking the reference level $\Delta A = 0$. Modulated amplitude upon application of $\mu_0 H_{\mathrm{ac}} = 100\,\mu\mathrm{T}$ perpendicular (solid, red) and parallel (dashed, black) to the induced easy axis. (b) Variation of the amplitude modulation to a constant test field $\mu_0 H_{\mathrm{ac}} = 20\,\mu\mathrm{T}$ due to tuning of the FeCoSiB working point with a bias field H_{dc}.

on a self-biased sensing layer, with maximum sensitivity at zero bias field.[231,232] For example, Lage et al.[233] reported on a ME cantilever sensor, in which self-biasing was realized by antiferromagnetic exchange coupling in a laminate system. The sensor exhibited maximum sensitivity at $\mu_0 H_{\mathrm{dc}} = 0\,\mu\mathrm{T}$ due to the intrinsic self-bias.

To demonstrate the sensor concept, the rms value of the oscillation modulation ΔA_{rms} is used as a measure for the magnetic field amplitude and recorded for 5 s for every datapoint. The magnetic test field amplitude $\mu_0 H_{\mathrm{ac}}$ is first decreased from 100 μT to 400 nT and subsequently increased again. The field is applied perpendicular to the EA and the field frequency $f_{\mathrm{H}} = 15\,\mathrm{Hz}$ is within the biomedically relevant range[234,235]. A corresponding measurement is presented in Fig. 9.4, confirming a linear and hysteresis-free response of the sensor to external magnetic fields. Considering the lowest detectable field of 400 nT of the proof-of-principle demonstrator, biomedical applications require an increase of sensitivity of several orders of magnitude. However, while related macroscopic ME sensors achieved a sensitivity up to $5.4\,\mathrm{pT}/\sqrt{\mathrm{Hz}}$,[200] so far they do not access the required frequency regime due to their passive resonant design. On the other hand the presented sensor design responds throughout the biomedically interesting frequency range as demonstrated in the following. In addition, Marauska et al.[236] detected fields as low as 100 pT with a passive MEMS-based ME sensor, proving the capability of accessing the sub-nT regime with microcantilever-sensors. Measures for the improvement of the sensitivity in future sensor designs based on the presented concept will be suggested in the outlook of Part II.

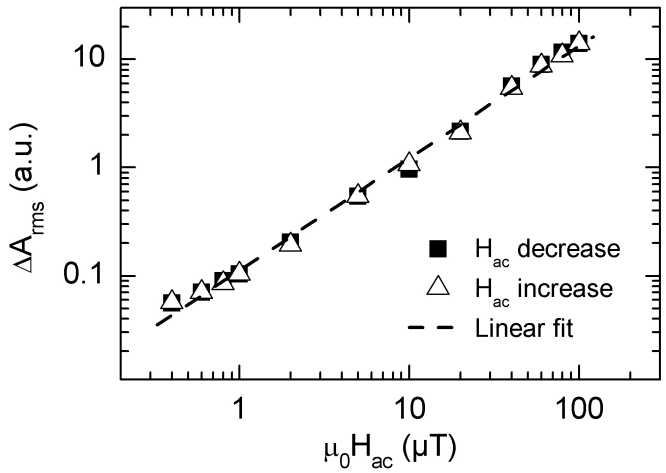

FIG. 9.4: rms value of the amplitude modulation for applied test fields H_{ac} with $f_{\mathrm{H}} = 15\,\mathrm{Hz}$ and a constant bias field of $\mu_0 H_{\mathrm{dc}} = 353\,\mu\mathrm{T}$. From Gojdka et al.[201].

In order to determine the frequency of magnetic test fields, the mechanical oscillation of the cantilever sensor is Fourier transformed. Figure 9.5 depicts the Fourier transforms for magnetic test fields with $\mu_0 H_{\mathrm{ac}} = 20\,\mu\mathrm{T}$ and frequencies of $f_{\mathrm{H}} = 10\,\mathrm{Hz}$, 100 Hz and 1000 Hz, respectively. The magnetic field frequency f_{H} is in all three cases clearly identifiable. Such separation and identification of magnetic field frequencies is paramount in biomagnetic applications since individual frequency components can be related to specific diagnoses.[196] As is shown in Fig. 9.5 virtually no higher-order harmonics are present in the Fourier transforms of the different magnetic test fields. Since the individual frequency components are independent of each other in the Fourier transform, the presented concept allows for straightforward frequency analysis of complex magnetic fields.

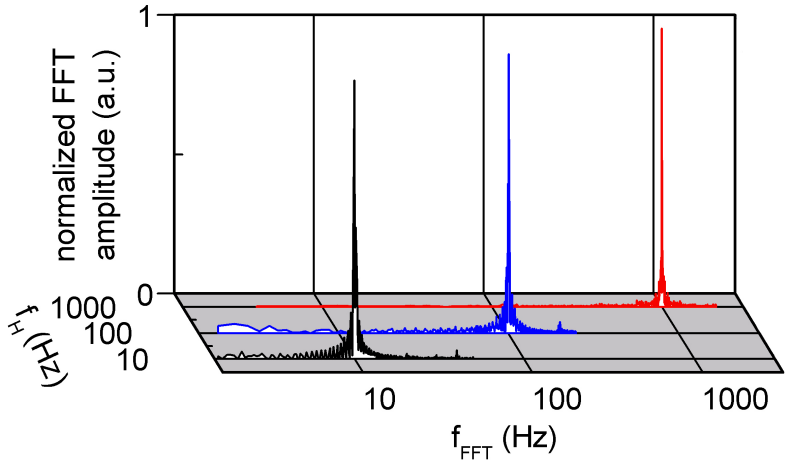

FIG. 9.5: Fourier transforms of the amplitude modulation $\hat{A}(t)$ upon application of $\mu_0 H_{\mathrm{ac}} = 20\,\mu\mathrm{T}$ with $f_{\mathrm{H}} = 10$, 100 and 1000 Hz, respectively. From Gojdka et al.[201].

Part II - Summary and Outlook

The functionality of a potentially fully integrable MagMEMS magnetic field sensor concept based on the delta-E effect has been demonstrated. The prototype sensor consisted of a commercial tipless AFM cantilever functionalized with a layer of 500 nm of amorphous $(Fe_{90}Co_{10})_{78}Si_{12}B_{10}$. The shift of the resonance frequency of the mechanically driven oscillator due to the delta-E effect of the FeCoSiB layer enabled the measurement of magnetic field amplitudes as low as 400 nT by amplitude modulation. A major advantage of the concept is the mechanical excitation of the oscillation without the need for magnetic driving fields, making it potentially fully integrable. The concept is sensitive especially in the biomedically relevant low-frequency regime $f < 1\,\mathrm{kHz}$ and offers a larger bandwidth compared to related passive ME sensing concepts.

For biomagnetic applications, however, the sensitivity will have to be increased in future designs. Just recently in 2011, Lassagne et al.[237] reported of a novel nanoelectromechanical (NEMS) magnetometer, demonstrating the general groundbreaking potential of future resonant magnetic field sensors. In the case of the presented design, several measures appear promising in order to improve the sensitivity.

The sensitivity of both amplitude and frequency detection scheme can be improved by an increase of the resonator's Q-factor by driving it in vacuum and by optimizing the oscillator itself.[238] In this way sensitivity should be increased by 1 to 2 orders of magnitude[223,239,240] with respective vacuum encapsulation of MEMS systems being present-day state of the art.[238,240,241] Furthermore, the FeCoSiB coating thickness can be optimized with respect to the cantilever dimension by thinning the Si beam on the one hand[236] and adjustment of the deposition on the other hand, cf. Equation (7.7) as a starting point. However, upon increasing the coating-to-substrate ratio one has to take into account a possible decrease of the Q-factor. For example, Marauska et al.[236] found $Q \approx 70$ under ambient conditions for a passive MEMS-based ME cantilever sensor which incorporated only 650 nm SiO_2 substrate as compared to a functional coating of 2.2 μm FeCoSiB and 1.0 μm AlN. Nonetheless, already in coarse vacuum ($p \approx 10\,\mathrm{Pa}$) the sensor exhibits $Q \approx 200$[238] and reaches a minimum detectable field of $\mu_0 H \approx 100\,\mathrm{pT}$ under ambient conditions[236], demonstrating the ability of MEMS-based approaches to access the pT-regime.

An optimized geometric design might further promote the frequency shift response of the oscillator to a change of Young's modulus of the functional layer. As a counterexample consider a quartz microbalance coated with a functional delta-E layer. Even if the coating changes E, no frequency shift will occur at the quartz oscillator since the oscillation frequency is sensitive only to a change in mass as a consequence of the geometry. Accordingly, future MEMS geometries might be optimized in order efficiently transduce the change in E into a frequency shift. Finally, in an advanced design the frequency shift can be detected directly in the FM scheme using a phase-locked-loop (PLL). The sensitivity of AM and FM detection is theoretically similar under identical operation conditions.[223] However, AFM-related investigations demonstrated better performance of FM mode compared to AM.[223] FM detection especially circumvents restriction of bandwidth at high Q-factors.

Taking into account all suggested measures, a sensitivity in the order of or below 100 pT appears achievable for future sensor designs based on the demonstrated concept. While this would not suffice for MEG[194], such sensitivity and its availability in the frequency regime $f < 200\,\mathrm{Hz}$, would for example enable basic MCG[198]. The improved sensitivity of an advanced sensor design should indeed allow for the clinically relevant measurement of brain ($f =$ 5–15 Hz and 100–200 Hz)[242] and heart ($f \approx 1\,\mathrm{Hz}$)[196] pacemakers. Especially the relevant low frequencies represent no obstacle for the presented concept while posing a challenge for passive ME sensor designs. Furthermore, a refined system might contribute to the control of advanced drug delivery[197,243,244] and *in-vivo* medical imaging[195,245]. Assuming a future sensitivity of 100 pT of the system, one can estimate how many nanoparticles are necessary in order to create a detectable magnetic field. Considering for the sake of simplicity only the z-component of the field, one obtains[195]

$$B_z = (\mu_0)/(2\pi)(\mu/z^3) \tag{9.1}$$

where μ_0 permeability of free space, μ magnetic moment and z distance between source and sensor. The total magnetic moment is the sum of the z-projections of the N individual nanoparticles $\mu = N\mu_\mathrm{P}$ with

$$\mu_\mathrm{P} = M_\mathrm{S}(4/3)\pi(D/2)^3 \quad . \tag{9.2}$$

Assuming $M_\mathrm{S} = 4.7 \times 10^5\,\mathrm{A/m}$[195] for medically relevant Fe_3O_4 magnetite particles, $D = 40\,\mathrm{nm}$ and $z = 4\,\mathrm{cm}$, Equations (9.1) and (9.2) yield approximately $N = \mathcal{O}(10^9)$ particles necessary for detectable fields of 100 pT. As Flynn and Bryant[195] pointed out, such particle amounts can be realistically expected in tumors due to the high density of antibody binding sites on cancer cells and Lewin et al.[245] found $N \approx 10^7$ particles per cell. Hence, the sensors system might well be applicable to drug delivery and *in-vivo* imaging once a sensitivity of 100 pT is reached.

With respect to integrability, the optical read-out could be replaced in a future design by a piezoelectric layer as is used in other ME sensors.[200] Advantageously, in FM detection the magnetic field information is extracted solely from the frequency (shift) of the oscillation. Thus, even if the amplitude signal from a piezoelectric layer was inferior to the optical read-out scheme the overall sensor performance would not necessarily be deteriorated. A further step towards integration can be achieved by replacing the external dc magnetic field which tunes the working point of the FeCoSiB layer by an internal bias. The principle has already been demonstrated by Lage et al.[233] for a ME sensor in which antiferromagnetic exchange coupling in a multi-layered system was exploited in order to achieve maximum $\partial\lambda/\partial H$ at zero external bias field.

The potential integrability of the presented concept and its compatibility with existing MEMS technology render it interesting not only for biomagnetic applications but also for the integration in existing microelectronics. Due to the presented characteristics, the sensor concept yields application potential whenever magnetic fields with frequencies from quasi-static up to some kHz have to be measured under the consideration of costs, space and compatibility with established micromachining techniques.

Acknowledgments

I would like to thank Prof. Dr. Franz Faupel for giving me the opportunity to work under his experienced guidance. I express my heartfelt gratitude for the trust he has had in me and the freedom with which he allowed me to pursue my research. I am especially thankful for his sympathetic attitude towards personal matters and the very enjoyable collaboration we have had in the past three years. It has been a great pleasure to be a member of his working group!

I will always remember my supervisor Dr. Vladimir Zaporojtchenko who left us much too early. He was an excellent scientist who generously shared his experience and ideas. But more than that, he always offered comfort and advise both in professional and private matters. His inspiring influence on my personality has become a part of me and I am grateful for having had the honor to meet Vladimir. We all miss him dearly.

I am much obliged to Dr. Thomas Strunskus for supervising me and for our numerous fruitful discussions. When things got stuck, his ideas and counsel always yielded a solution. To share the office with him was an enjoyment. I owe him my special thanks for proof-reading of this thesis.

Prof. Dr. Klaus Rätzke has always been a source of wise counsel whether in professional or private matters. I will never forget our great sailing trips and I express my gratitude for all his help and encouragement especially when the going got tough.

The elaborate TEM studies presented in this work were conducted by Prof. Dr. Lorenz Kienle and Viktor Hrkac and I would like to thank them for the very rewarding and pleasant cooperation.

Many thanks to Prof. Dr. Hermann Kohlstedt for the permission to conduct unusual experiments even with brand-new equipment and for all the valuable discussions. I am indebted to Dr. Adrian Petraru for his patience and all the competent help he kindly offered whenever needed.

Furthermore, I am thankful for the collaboration with Prof. Dr. Reinhard Knöchel and Robert Jahns which lead to the development of the presented magnetic field sensor.

I heartily thank Prof. Dr. Rainer Adelung, Prof. Dr. Jeffrey McCord, Prof. Dr. Martina Gerken and Dr. Dirk Meyners for all the fruitful discussions and for supporting my research by sharing their immense expertise with me.

I am indebted to Prof. Dr. Paul Muralt from the École polytechnique fédérale de Lausanne for admitting me to join his team as a guest scientist. I am most thankful for his exceptional generosity in letting me benefit from his experience, knowledge and ideas.

The presented work would not have been possible without the SFB 855 "*Mag-*

netoelectric Composites - Future Biomagnetic Interfaces" headed by Prof. Dr. Eckhard Quandt. I kindly acknowledge the funding of the project by the German Research Foundation (DFG).

The deposition system would not exist in its present form without the outstanding constructional skills of Stefan Rehders. In addition, I am thankful for having learned a lot during the collaboration with him. Further technical assistance was provided by Christoph Ochmann and Alexander Vahl whom I express my gratitude for their absolute reliability and the fun it was to work with them. Also, the workshop of the Faculty of Engineering did an excellent job whenever needed. Thus, I would like to thank Berndt Neumann, Matthias Burmeister and all workshop staff.

Rainer Kloth supported the project with his distinct electronics skills. My thoughts are with him and his family and I wish him all the best for his recovery.

For having coped with the flood of orders I created during the construction of the deposition machine I would like to thank the office staff of the Multicomponent Materials group. Thank you for keeping things running!

The last three years would not have been the great time they were without my colleagues at the Faculty of Engineering. My special thanks to Tilo Peter, Kerstin Meurisch, Sören Kapps, Bodo Henkel, Viktor Hrkac, Robert Jahns, Tommi Hrkac, Christina Pakula, Sri Wahyuni Basuki, Dr. Sebastian Wille, Nisreen Alissawi, Dr. Ulrich Schürmann, Tönjes Koschine, Christian Ohrt, Dr. Amit Kulkarni, Viktor Schneider, Dr. Yogendra Kumar Mishra, Arnim Schuchardt, Jian Xiong and all the other colleagues who make the Institute for Material Science such a great place to be.

Finally, my very special thanks to my family. I cannot befittingly express my gratitude for their overwhelming backup and encouragement, for their confidence in me and for all their love.

Appendix A: Technical Documentation

Deposition Electronics

In order to realize the deposition processes necessary for the aims of this thesis, the commercial magnetron power supplies were extended with further electronics as described in the following.

Figure A.1 depicts the respective deposition-related circuitry. Two MDX 500 dc-generators (Advanced Energy) are operated in constant power mode for the operation of the gas aggregation cluster source (GAS) and the center magnetron, respectively. For all experiments of this thesis, straight dc power was applied to the magnetron of the GAS by directly connecting the MDX 500. In the case of the center magnetron, further electronics were introduced in order to allow for reactive sputtering with pulsed dc power on the one hand and low-frequency quasi-co-sputtering on the other hand. Standard dc powering of the center magnetron is obtained with a straight connection of the MDX 500 unit with the magnetron.

For pulsed dc power operation of the center magnetron, the MDX 500 output is connected to a self-constructed pulsing-box[i]. The latter chops the continuous dc input with a power MOSFET (HTS31 with cooling fins, Behlke) which is triggered by an external frequency generator (4025, Peaktech). The trigger amplitude is $\hat{U}_\mathrm{f} = 5\,\mathrm{V}$ with an offset of 2.5 V in order to provide a positive square signal $U_\mathrm{f} = 0$–$5\,\mathrm{V}$. It should be noted that the choice of duty cycle crucially influences the voltage provided by the MDX 500. In order to supply the time-averaged power defined by the user, higher voltages have to be applied if shorter duty cycles are chosen. Duty cycles between 50–100 % and frequencies $f_\mathrm{dc} = 15$–$70\,\mathrm{kHz}$ were found to provide stable operation conditions for pulsed dc deposition of AlN.

If additional low-frequency pulsing is desired for co-deposition by quasi-co-sputtering (cf. chapter 5.1), the MDX unit can be triggered by self-built electronics. By setting switch number 5 on the rear of the power generator to "up", the output control is transferred to remote control via the user port of the MDX unit.[246] Note that in this setting, the output can still be turned off via the front

[i] design by R. Kloth

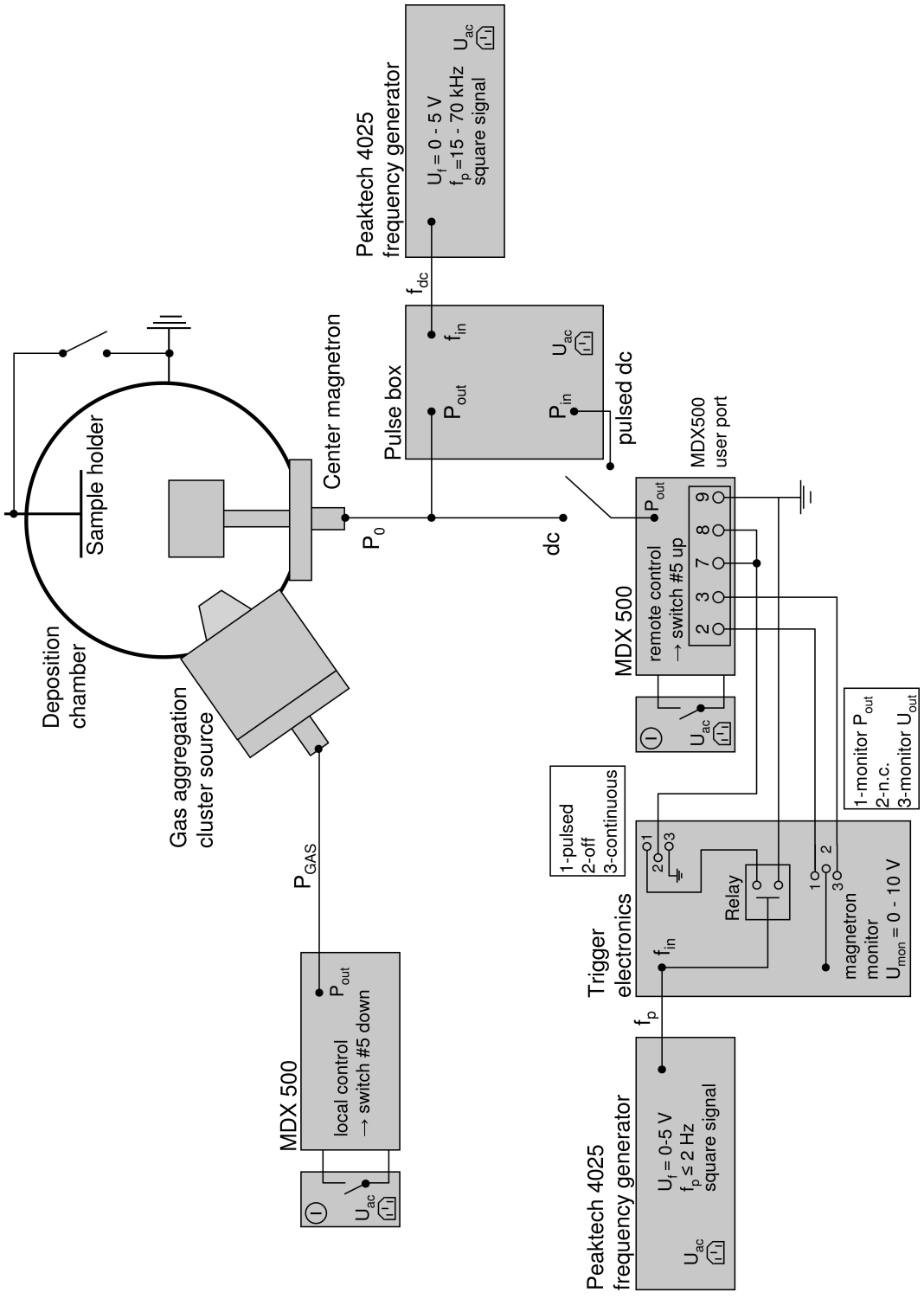

FIG. A.1: Schematic of the deposition-related electronics. Refer to text for details.

panel. However, in order to activate the output, pins 7 and 8 of the user port have to be connected to ground, pin 9.[247] The trigger electronics allow to either directly connect pins 7 and 8 to ground for continuous output or pulsed connection via a relay. It is important to notice that if pins 7 and 8 are continuously connected to ground via the trigger electronics, the "stop"-button of the MDX front panel is overridden. In this case the target bias voltage can be turned off only by setting the switch of the trigger electronics to the "off"-position. For pulsed operation, the relay is switched by another frequency generator (4025, Peaktech), again with a square signal of $\hat{U}_\mathrm{f} = 5\,\mathrm{V}$ amplitude. Due to the sluggish response of the MDX 500 unit and the plasma ignition, trigger frequencies above $f_\mathrm{p} = 2\,\mathrm{Hz}$ are not feasible (however, already $f_\mathrm{p} = 0.3\,\mathrm{Hz}$ results in homogeneous composites, cf. chapter 5.1). In addition to the pulsing control, the self-built electronics offer an output connection for monitoring the MDX 500 output. Depending on the position of the respective switch either the power or the voltage is monitored. The monitor voltage is in between $U_\mathrm{mon} = 0$–$10\,\mathrm{V}$ corresponding linearly to the full power or voltage output range of the MDX 500.

High-Vacuum Deposition System

As part of the presented thesis a new high-vacuum (HV) deposition machine was constructed, the schematic of which is shown in Fig. A.2. The system is divided into three parts which can be pumped and vented individually. In the main chamber (1) deposition takes places. Thanks to the transfer system, the main chamber ideally needs no venting, ensuring clean HV conditions for the deposition of high-quality thin films. However, depending on the amount of material deposited, the sample holder front piece has to be cleaned in intervals of typically $\approx 2\,\mathrm{months}$ in order to remove flakes of accumulated deposits.

Servicing of the vented main chamber is conducted via the front door (4). For the introduction or removal of samples, the transfer system (red) can be disconnected from the main chamber by valve (6) and from the gas aggregation cluster source (GAS, green) by valve (11). The fixation of the transfer rod (9) must not be loosened before venting of the transfer system is completed! Otherwise the lever of the transfer arm will open the load lock (8), leading to uncontrolled and potentially harmful venting. In addition, when rotating the transfer rod after venting, the magnetic sledge (10) must be fully retracted.

The GAS (green) can be (dis-)connected from the main chamber by valve (15). Accordingly, during operation of the GAS valve (15) is open, to introduce the generated particles into the main chamber. Valve (16) is used for venting and pumping of the GAS and has to be closed during operation of the GAS for the process gas to flow through the aperture (14). In order to pump part of the GAS process gas through the load lock, valve (11) is opened. If the GAS is to be serviced (e.g., for target replacement), it can be vented via the load lock by opening valves (11), (16) and closing valve (15).

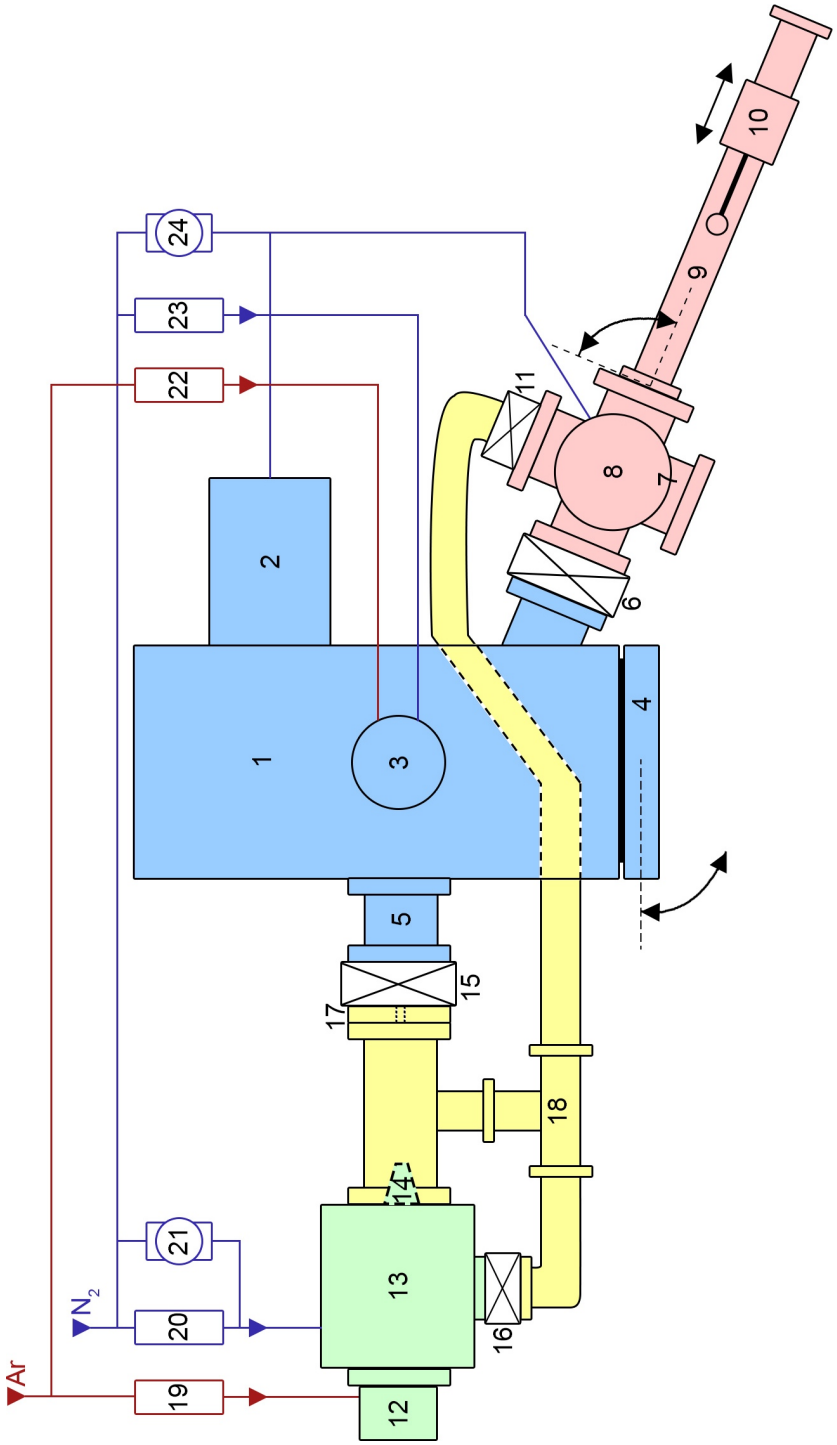

FIG. A.2: Schematic of the deposition system which was developed in the course of this work. Refer to text for details.

Appendix B: AlN/Co Deposition Process

In chapter 4.1 the development of the deposition process for c-axis oriented AlN is discussed followed by the quasi-co-sputtering concept for AlN/Co nanocomposites in chapter 5.1. In contrast, this appendix details the respective experimental procedure step-by-step. The initial state of the deposition system is as follows: The valves between load lock and main chamber, and GAS and main chamber are closed, respectively. The GAS is connected to and pumped via the load lock. With the z-drive of the Al-magnetron at the position of 10 mm, the target-substrate distance is $d = 55\,\mathrm{mm}$. The TMP of the main chamber is set to 80 %-standby and the TMP of the load lock to 66 % in order to reduce the working load of the pumps due to the process gas. The sample shutter is closed, shielding the sample from deposits prior to the deposition step.

1. substrate preparation
   The substrate, consisting of 150 nm Pt(111) - 10 nm Ti - 1000 nm SiO_2 on 525 μm (100)-Si prime grade wafers, is cleaned by application of 5 min ultrasonic bath in acetone, subsequent dip-rinsing in isopropanol and final drying in a flow of nitrogen gas. The ultrasonic bath should be applied only to one piece of substrate at a time since the Pt surface is prone to become degraded by scratches if multiple pieces are placed in the same beaker.

2. substrate heating
   After the substrate is transferred to the sample holder, a heating procedure can be applied if a deposition at elevated substrate temperature is desired. During the course of this work a substrate temperature of approximately 330 °C was obtained by following the heating ramp given in Table 1. To achieve a stable steady-state, some process gas $\Phi_{\mathrm{Ar},0} = 15\,\mathrm{SCCM}$ is already introduced into the main chamber at this point of time.

3. Al target cleaning
   To establish a well-defined state of the target surface, the latter is clean sputtered for $t = 20\,\mathrm{min}$ at $P_{\mathrm{dc},0} = 90\,\mathrm{W}$ and $\Phi_{\mathrm{Ar},0} = 50\,\mathrm{SCCM}$. After the cleaning the sputtering power is turned off since at this time the dc pulsing unit is in-

Heating current	[A]	1.5	2.5	3.5	4.0
Resulting voltage	[V]	1.2	2.5	3.6	4.2
Resting time	[min]	5	10	20	20

Table 1: Summary of heating ramp for a substrate temperature of $T_s \approx 330\,^{\circ}\mathrm{C}$.

terconnected between center magnetron and power supply in order to prepare the next process step.

4. AlN target conditioning, GAS conditioning
   The conditioning step aims at the establishment of steady-state conditions prior to the deposition. First, working gas is also injected through the GAS. Reactive gas admixture can be introduced via the manual leakage valve at this point of time. Typical argon flow for GAS operation are $\Phi_{\mathrm{Ar,GAS}} = 100$–$140\,\mathrm{SCCM}$. Once the process gas flows are enabled in the GAS, the valve connecting GAS to main chamber is opened. The center magnetron flow is reduced to $\Phi_{\mathrm{Ar},0} = 15\,\mathrm{SCCM}$ as the GAS provides sufficient argon for the center discharge.

   With the process atmosphere established, conditioning of the targets can begin. The pulse box is switched on, triggered by an external frequency generator at $f_{\mathrm{dc}} = 50\,\mathrm{kHz}$ and 70 % duty cycle. The center discharge is initiated at $P_{\mathrm{dc},0} = 90\,\mathrm{W}$ with pure argon and nitrogen $\Phi_{\mathrm{N}_2,0} = 65\,\mathrm{SCCM}$ is added to the plasma. After $t = 15\,\mathrm{min}$ the target is considered conditioned and the discharge operates in steady-state.

   During the last 5 min of the AlN conditioning, the operation of the GAS is started at typical powers (for Co) of $P_{\mathrm{GAS}} = 100$–$140\,\mathrm{W}$. This ensures that target oxidation is removed and the cluster rate stabilizes prior to deposition.

5. continuous or pulsed deposition
   To start the deposition the sample shutter is opened, allowing deposits to reach the substrate. With the sample shutter open, the substrate bias voltage U_s due to the deposition plasma can be monitored. If pure AlN is deposited, the process can be conducted continuously. However, for the inclusion of nanoparticles from the GAS, the AlN deposition is pulsed at $f_p \approx 0.3\,\mathrm{Hz}$ for quasi-co-sputtering (cf. chapter 5.1). Continuous or pulsed AlN deposition is selected by a self-built controller, which is connected to the control port of the center magnetron's power supply. The respective trigger signal is provided to the controller by another frequency generator. If nanocomposites were prepared by quasi-co-sputtering, at least 1 min of continuous operation were applied at the beginning of the deposition in order to form a well-defined seed layer of AlN for the further growth of the composite.

Bibliography

1. D. Vollath, *Nanomaterials - An Introduction to Synthesis, Properties and Applications* (Wiley, Weinheim, 2008).

2. R. K. Waits, J. Vac. Sci. Technol. **15**, 179 (1978).

3. S. Berg, H.-O. Blom, T. Larsson, and C. Nender, J. Vac. Sci. Technol. A **5**, 202 (1986).

4. S. Schiller, K. Goedicke, J. Reschke, V. Kirchhoff, S. Schneider, and F. Milde, Surf. Coat. Tech. **61**, 331 (1993).

5. F. Faupel, V. Zaporojtchenko, T. Strunskus, and M. Elbahri, Adv. Eng. Mater. **12**, 1177 (2010).

6. K. Sattler, J. Muhlbach, and E. Recknagel, Phys. Rev. Lett. **45**, 821 (1980).

7. H. Haberland, M. Moseler, Y. Qiang, O. Rattunde, T. Reiners, and Y. Thurner, Surf. Rev. Lett. **3**, 887 (1996).

8. C.-W. Nan, Y. Shen, and J. Ma, Annu. Rev. Mater. Res. **40**, 131 (2010).

9. C.-W. Nan, M. I. Bichurin, S. Dong, D. Viehland, and G. Srinivasan, J. Appl. Phys. **103**, 031101 (2008).

10. J. S. Moya, S. López-Esteban, and C. Pecharromán, Prog. Mater. Sci. **52**, 1017 (2007).

11. C. Brosseau, A. Beroual, and A. Boudida, J. Appl. Phys. **88**, 7278 (2000).

12. J. Curie and P. Curie, C. R. Acad. Sci. Paris **91**, 294 (1880).

13. R. C. Buchanan, ed., *Ceramic Materials for Electronics* (Dekker, New York, 2004), pp. 209-216.

14. G. Lippmann, Ann. Chim. Phy. **24**, 145 (1881).

15. J. Curie and P. Curie, C. R. Acad. Sci. Paris **93**, 1137 (1881).

16. K. Uchino, *Ferroelectric devices* (Taylor&Francis, 2010), pp. 25-35.

17. J. P. Joule, Annals of Electricity, Magnetism, and Chemistry **8**, 219 (1842).

18. R. C. O'Handley, *Modern Magnetic Materials: Principles and Applications* (John Wiley & Sons, New York, 2000), pp. 229-234.

19. G. Engdahl, *Handbook of Giant Magnetostrictive Materials* (Academic, 2000), pp. 130-132.

20. B. D. Cullity and C. D. Graham, *Introduction to Magnetic Materials* (John Wiley & Sons, Hoboken, NJ, 2009), ch. 8.

21. R. M. Bozorth, *Ferromagnetism* (IEEE Press, 1993).

22. V. Clavijo-Jordan, V. D. Kodibagkar, S. C. Beeman, B. D. Hann, and K. M. Bennett, WIREs Nanomed. Nanobiotechnol. **4**, 345 (2012).

23. K. E. Scarberry, E. B. Dickerson, Z. J. Zhang, B. B. Benigno, and J. F. McDonald, Nanomed.-Nanotechnol. **6**, 399 (2010).

24. E. Bellido, N. Domingo, I. Ojea-Jiménez, and D. Ruiz-Molina, small **8**, 1465 (2012).

25. M. Nelo, A. K. Sowpati, V. K. Palukuru, J. Juuti, and H. Jantunen, Prog. Electromagn. Res. **110**, 253 (2010).

26. J. Zhu, K. Kailasam, A. Fischer, and A. Thomas, ACS Catal. **1**, 342 (2011).

27. N. Malvadkar, S. Park, M. Urquidi-MacDonald, H. Wang, and M. C. Demirel, J. Power Sources **182**, 323 (2008).

28. S. Sun, Adv. Mater. **18**, 393 (2006).

29. D. Weller and M. F. Doerner, Annu. Rev. Mater. Sci. **30**, 611 (2000).

30. B. D. Cullity and C. D. Graham, *Introduction to Magnetic Materials* (John Wiley & Sons, Hoboken, NJ, 2009), ch. 11.

31. R. C. O'Handley, *Modern Magnetic Materials: Principles and Applications* (John Wiley & Sons, New York, 2000), ch. 12.

32. G. Herzer, IEEE T. Magn. **26**, 1397 (1990).

33. R. C. O'Handley, *Modern Magnetic Materials: Principles and Applications* (John Wiley & Sons, New York, 2000), pp. 449-452.

34. S. Ge, D. Yao, M. Yamaguchi, X. Yang, H. Zuo, T. Ishii, D. Zhou, and F. Li, J. Phys. D: Appl. Phys. **40**, 3660 (2007).

35. A. E. Berkowitz, W. J. Schuele, and P. J. Flanders, J. Appl. Phys. **39**, 1261 (1968).

36. H. M. Lu, W. T. Zheng, and Q. Jiang, J. Phys. D: Appl. Phys. **40**, 320 (2007).

37. J. M. D. Coey, Phys. Rev. Lett. **27**, 1140 (1971).

38. F. T. Parker, M. W. Foster, D. T. Margulies, and A. E. Berkowitz, Phys. Rev. B **47**, 7885 (1993).

39. W. Gong, H. Li, Z. Zhao, and J. Chen, J. Appl. Phys. **69**, 5119 (1991).

40. M. K. Hedayati, M. Javaherirahim, B. Mozooni, R. Abdelaziz, A. Tavassolizadeh, V. S. K. Chakravadhanula, V. Zaporojtchenko, T. Strunkus, F. Faupel, and M. Elbahri, Adv. Mater. **23**, 5410 (2011).

41. A. A. Ashkarran, S. M. Aghigh, M. Kavianipour, and N. J. Farahani, Curr. Appl. Phys. **11**, 1048 (2011).

42. W. Tsang, V. Stolojan, S. Wong, J. Linder, B. Sealy, and S. Silva, Rev. Adv. Mater. Sci. **15**, 179 (2009).

43. L. Maya, M. Paranthaman, J. R. Thompson, T. Thundat, and R. J. Stevenson, Mat. Res. Soc. Symp. Proc. **457**, 213 (1996).

44. R. P. Ortiz, A. Facchetti, and T. J. Marks, Chem. Rev. **110**, 205 (2010).

45. A. L. Efros and B. I. Shklovskii, Phys. Status Solidi B **76**, 475 (1976).

46. D. J. Bergman and Y. Imry, Phys. Rev. Lett. **39**, 1222 (1977).

47. C. Pecharromán, F. Esteban-Betegón, J. F. Bartolomé, S. López-Esteban, and J. S. Moya, Adv. Mater. **13**, 1541 (2001).

48. H. Scher and R. Zallen, J. Chem. Phys. **53**, 3759 (1970).

49. R. Zallen, *The Physics of Amorphous Solids* (Wiley, New York, 1983), pp. 183-191.

50. R. C. Buchanan, ed., *Ceramic Materials for Electronics* (Dekker, New York, 2004), pp. 1-16.

51. A. J. Moulson and J. M. Herbert, *Electroceramics* (John Wiley & Sons, Chichester, 2003), 2nd ed., ch. 5.

52. H. Lustfeld, C. Pithan, and M. Reißel, J. Eur. Ceram. Soc. **32**, 859 (2012).

53. J. Huang, Y. Cao, M. Hong, and P. Du, Appl. Phys. Lett. **92**, 022911 (2008).

54. S. George and M. T. Sebastian, Compos. Sci. Technol. **68**, 2461 (2008).

55. B. Gojdka, V. Hrkac, J. Xiong, M. Gerken, L. Kienle, T. Strunskus, V. Zaporojtchenko, and F. Faupel, J. Appl. Phys. (2012).

56. M. Fiebig, J. Phys. D: Appl. Phys. **38**, R123 (2005).

57. J. van Suchtelen, Philips Res. Rep. **27**, 28 (1972).

58. W. Eerenstein, N. D. Mathur, and J. F. Scott, Nature **442**, 759 (2006).

59. J. Ma, J. Hu, Z. Li, and C.-W. Nan, Adv. Mater. **23**, 1062 (2011).

60. C.-W. Nan, Phys. Rev. B **50**, 6082 (1994).

61. R. Jahns, H. Greve, E. Woltermann, E. Lage, E. Quandt, and R. Knoechel, Medical Measurements and Applications Proceedings p. 107 (2011).

62. C.-W. Nan and D. R. Clarke, J. Am. Ceram. Soc. **80**, 1333 (1997).

63. Z. Xing, J. Li, and D. Viehland, Appl. Phys. Lett. **91**, 182902 (2007).

64. X. Zhuang, M. L. C. Sing, C. Cordier, S. Saez, C. Dolabdjian, J. Das, J. Gao, J. Li, and D. Viehland, IEEE Sens. J. **11**, 2183 (2011).

65. R. A. Islam and S. Priya, Advances in Condensed Matter Physics **2012**, 320612 (2012).

66. A. E. Clark, *Ferromagnetic Materials* (North Holland, Amsterdam, 1980), p. 531.

67. R. M. Bozorth, E. F. Tilden, and A. J. Williams, Phys. Rev. **99**, 1788 (1955).

68. J. H. Park, H. M. Jang, H. S. Kim, C. G. Park, and S. G. Lee, Appl. Phys. Lett. **92**, 062908 (2008).

69. J. H. Edgar, ed., *Properties of group III nitrides* (INSPEC, London, 1994).

70. H. Vollstadt, E. Ito, M. Akaishi, S. Akimoto, and O. Fukunaga, Proc. Jpn. Acad. B **66**, 7 (1990).

71. Q. Xia, H. Xia, and A. L. Ruoff, J. Appl. Phys. **73**, 8198 (1993).

72. V. Fuflyigin, E. Salley, A. Osinsky, and P. Norris, Appl. Phys. Lett. **77**, 3075 (2000).

73. F. Martin, P. Muralt, M.-A. Dubois, and A. Pezous, J. Vac. Sci. Technol. A **22**, 361 (2004).

74. S. Marauska, V. Hrkac, T. Dankwort, R. Jahns, H. J. Quenzer, R. Knöchel, L. Kienle, and B. Wagner, Microsyst. Technol. **18**, 787 (2012).

75. S. A. Wilson, R. P. J. Jourdain, Q. Zhang, R. A. Dorey, C. R. Bowen, M. Willander, Q. U. Wahab, M. Willander, S. M. Al-hilli, O. Nur, et al., Mater. Sci. Eng. R **56**, 1 (2007).

76. M. Akiyama, K. Nagao, N. Uenoa, H. Tateyama, and T. Yamada, Vacuum **74**, 699 (2004).

77. M.-A. Dubois and P. Muralt, J. Appl. Phys. **89**, 6389 (2001).

78. S. Strite, M. E. Lin, and H. Morkoç, Thin Solid Films **231**, 197 (1993).

79. K. M. Taylor and C. Lenie, J. Electrochem. Soc. **107**, 308 (1960).

80. W. M. Haynes and D. R. Lide, eds., *CRC Handbook of Chemistry and Physics* (CRC Press, Boca Raton, 2010), 91st ed.

81. D. Gerlich, S. L. Dole, and G. A. Slack, J. Phys. Chem. Solids **47**, 437 (1986).

82. B. D. Cullity and C. D. Graham, *Introduction to Magnetic Materials* (John Wiley & Sons, Hoboken, NJ, 2009), p. 387.

83. B. D. Cullity and C. D. Graham, *Introduction to Magnetic Materials* (John Wiley & Sons, Hoboken, NJ, 2009).

84. R. C. O'Handley, *Modern Magnetic Materials: Principles and Applications* (John Wiley & Sons, New York, 2000), p. 225.

85. R. C. O'Handley, *Modern Magnetic Materials: Principles and Applications* (John Wiley & Sons, New York, 2000), p. 437.

86. W. H. Meiklejohn and C. P. Bean, Phys. Rev. **102**, 1413 (1956).

87. W. Cho, I. Kagomiya, K. Kakimoto, and H. Ohasato, Appl. Phys. Lett. **89**, 152905 (2006).

88. Z.-M. Dang, Y.-H. Lin, and C.-W. Nan, Adv. Mater. **15**, 1625 (2003).

89. C. Kittel, *Einführung in die Festkörperphysik* (R. Oldenbourg, München, 1991), 9th ed., p. 179.

90. M. H. Chowdhury, M. A. Mannan, and S. A. Mahmood, IJETSE **2**, 1 (2010).

91. P. K. Panda, J. Mater. Sci. **44**, 5049 (2009).

92. C. L. Li, Z. H. Chen, Y. L. Zhou, and D. F. Cui, J. Phys.: Condens. Matter **13**, 5261 (2001).

93. K. Suzuki, T. Kaneko, H. Yoshida, H. Morita, and H. Fujimori, J. Alloy Compd. **224**, 232 (1995).

94. W. L. Warren, D. Dimos, and B. A. Tuttle, J. Am. Ceram. Soc. **77**, 2753 (1994).

95. I. P. Raevski, S. M. Maksimov, A. V. Fisenko, S. A. Prosandeyev, I. A. Osipenko, and P. F. Tarasenko, J. Phys.: Condens. Matter **10**, 8015 (1998).

96. M. Ohring, *The Materials Science of Thin Films* (Academic Press, San Diego, 1992).

97. D. L. Smith, *Thin-Film Deposition* (McGraw-Hill, New York, 1995).

98. V. S. Smentkowski, Prog. Surf. Sci. **64**, 1 (2000).

99. P. J. Kelly and R. D. Arnell, Vacuum **56**, 159 (2000).

100. W. Grove, Phil. Trans. Roy. Soc. **142**, 87 (1852).

101. S. Schiller, U. Heisig, K. Goedicke, K. Schade, G. Teschner, and J. Henneberger, Thin Solid Films **64**, 455 (1979).

102. P. D. Davidse and L. I. Maissel, J. Appl. Phys. **37**, 574 (1966).

103. M. Ohring, *The Materials Science of Thin Films* (Academic Press, San Diego, 1992), pp. 105-107.

104. D. L. Smith, *Thin-Film Deposition* (McGraw-Hill, New York, 1995), pp. 453-470.

105. R. Messier, A. P. Giri, and R. A. Roy, J. Vac. Sci. Technol. **2**, 500 (1984).

106. D. L. Smith, *Thin-Film Deposition* (McGraw-Hill, New York, 1995), pp. 402-432.

107. D. Depla and S. Mahieu, eds., *Reactive Sputter Deposition* (Springer, Berlin, 2008), pp. 229-251.

108. J. Goree, Plasma Sources Sci. T. **3**, 400 (1994).

109. H. Kersten, H. Deutsch, and G. Kroesen, Int. J. Mass. Spectrom. **233**, 51 (2004).

110. H. M. Mott-Smith and I. Langmuir, Phys. Rev. **28**, 727 (1926).

111. E. C. Whipple, Rep. Prog. Phys. **44**, 1197 (1981).

112. G. S. Selwyn, J. Singh, and R. S. Bennett, J. Vac. Sci. Technol. A **7**, 2758 (1989).

113. G. S. Selwyn, J. E. Heidenreich, and K. L. Haller, J. Vac. Sci. Technol. A **9**, 2817 (1991).

114. M. Bonitz, N. Horing, and P. Ludwig, *Introduction to Complex Plasmas* (Springer, Heidelberg, 2010).

115. W. Sproul, D. Christie, and D. Carter, Thin Solid Films **491**, 1 (2005).

116. L. B. Jonsson, T. Nyberg, and S. Berg, J. Vac. Sci. Technol. A **17**, 1827 (1999).

117. D. Depla and S. Mahieu, eds., *Reactive Sputter Deposition* (Springer, Berlin, 2008).

118. D. Depla and S. Mahieu, eds., *Reactive Sputter Deposition* (Springer, Berlin, 2008), ch. 5.

119. M. Ohring, *The Materials Science of Thin Films* (Academic Press, San Diego, 1992), p. 128.

120. S. Kadlec, J. Musil, and J. Vyskoĉil, Vacuum **37**, 729 (1987).

121. T. Nyberg, S. Berg, U. Helmersson, and K. Hartig, Appl. Phys. Lett. **86**, 164106 (2005).

122. W. D. Sproul, Vacuum **51**, 641 (1998).

123. J. W. Bradley and T. Welzel, J. Phys. D: Appl. Phys. **42**, 093001 (2009).

124. J. V. cek, A. Pajdarov, and J. Musil, Contrib. Plasma Phys. **44**, 426 (2004).

125. A. Belkind, A. Freilich, and R. Scholl, J. Vac. Sci. Technol. A **17**, 1934 (1999).

126. L. Jonsson, T. Nyberg, I. Katardjiev, and S. Berg, Thin Solid Films **365**, 43 (2000).

127. J. Sellers, Surf. Coat. Tech. **98**, 1245 (1998).

128. P. J. Kelly and R. D. Arnell, J. Vac. Sci. Technol. A **17**, 945 (1999).

129. J. Cherng and D. Chang, Vacuum **84**, 653 (2010).

130. Y. M. Kim, Y. M. Chung, M. J. Jung, J. V. c ek, J. Musil, and J. G. Han, Surf. Coat. Tech. **200**, 835 (2005).

131. K. Wegner, P. Piseri, H. V. Tafreshi, and P. Milani, J. Phys. D: Appl. Phys. **39**, R439 (2006).

132. H. Haberland, M. Karrais, M. Mall, and Y. Thurner, J. Vac. Sci. Technol. A **10**, 3266 (1992), clust.

133. B. M. Smirnov, I. Shyjumon, and R. Hippler, Phys. Scr. **73**, 288 (2006).

134. H. Biederman, Surf. Coat. Tech. **205**, S10 (2011).

135. M. Drabik, A. Choukourov, A. Artemenko, O. Polonskyi, O. Kylian, J. Kousal, L. Nichtova, V. Cimrova, D. Slavinska, and H. Biederman, J. Phys. Chem. C **115**, 20937 (2011).

136. B. Gojdka, V. Hrkac, T. Strunskus, V. Zaporojtchenko, L. Kienle, and F. Faupel, Nanotechnology **22**, 465704 (2011).

137. J. Bansmann, S. H. Baker, C. Binns, J. A. Blackman, J. P. Bucher, J. Dorantes-DÃ¡vila, V. Dupuis, L. Favre, D. Kechrakos, A. Kleibert, et al., Surf. Sci. Rep. **56**, 189 (2005).

138. M. Han, C. Xu, D. Zhu, L. Yang, J. Zhang, Y. Chen, K. Ding, F. Song, and G. Wang, Adv. Mater. **19**, 2979 (2007).

139. B. M. Smirnov, *Cluster Processes in Gases and Plasmas* (Wiley-VCH, Weinheim, 2010), pp. 385-391.

140. J. A. Thornton, Thin Solid Films **54**, 23 (1978).

141. I. Shyjumon, M. Gopinadhan, C. A. Helm, B. M. Smirnov, and R. Hippler, Thin Solid Films **500**, 41 (2005).

142. B. M. Smirnov, *Cluster Processes in Gases and Plasmas* (Wiley-VCH, Weinheim, 2010).

143. B. M. Smirnov, I. Shyjumon, and R. Hippler, Phys. Rev. E **75**, 066402 (2007).

144. V. N. Popok, I. Barke, E. E. B. Campbell, and K.-H. Meiwes-Broer, Surf. Sci. Rep. **66**, 347 (2011).

145. B. M. Smirnov and A. J. Strizhev, Phys. Scr. **49**, 615 (1994).

146. B. M. Smirnov, *Cluster Processes in Gases and Plasmas* (Wiley-VCH, Weinheim, 2010), ch. 9.

147. B. M. Smirnov, *Cluster Processes in Gases and Plasmas* (Wiley-VCH, Weinheim, 2010), pp. 265-283.

148. B. M. Smirnov, *Cluster Processes in Gases and Plasmas* (Wiley-VCH, Weinheim, 2010), pp. 391-392.

149. O. Polonskyi, P. Solař, O. Kylián, M. Drábik, A. Artemenko, J. Kousal, J. Hanuš, J. Pešička, I. Matolínová, E. Kolíbalová, et al., Thin Solid Films **520**, 4155 (2012).

150. S. Pratontep, S. J. Carroll, C. Xirouchaki, M. Streun, and R. E. Palmer, Rev. Sci. Instrum. **76**, 045103 (2005).

151. J. Townsend, *Electricity in Gases* (Clarendon Press, Oxford, 1915).

152. L. Reimer, *Scanning electron microscopy : physics of image formation and microanalysis* (Springer, Berlin, 1998).

153. D. B. Williams and C. B. Carter, *Transmission Electron Microscopy - A Textbook for Materials Science* (Springer, New York, 2009).

154. B. D. Cullity, *Elements of X-Ray Diffraction* (Addison-Wesley, Reading, MA, 1978), 2nd ed.

155. A. L. Kholkin, C. Wütchrich, D. V. Taylor, and N. Setter, Rev. Sci. Instrum. **67**, 1935 (1996).

156. W. Y. Pan and L. E. Cross, Rev. Sci. Instrum. **60**, 2701 (1989).

157. K. Lefki and G. J. M. Dormans, J. Appl. Phys. **76**, 1764 (1994).

158. P. Muralt, J. Am. Ceram. Soc. **91**, 1385 (2008).

159. G. Sauerbrey, Z. Phys. **155**, 206 (1959).

160. B. Gojdka, V. Zaporojtchenko, V. Hrkac, J. Xiong, L. Kienle, T. Strunskus, and F. Faupel, Appl. Phys. Lett. **100**, 133104 (2012).

161. V. Mortet, M. Nesladek, J. D'Haen, G. Vanhoyland, O. Elmazria, M. B. Assouar, P. Alnot, and M. D'Olieslaeger, phys. stat. sol. (a) **193**, 482 (2002).

162. C.-S. Chen, B.-H. Hwang, H.-Y. Lu, and T.-C. Hsu, J. Phys. D: Appl. Phys. **35**, 2608 (2002).

163. M.-A. Dubois, Ph.D. thesis, École Polytechnique Fédérale de Lausanne (1999).

164. R. Lanz, C. Lambert, L. Senn, L. Gabathuler, and G. J. Reynolds, Proc. IEEE Int. Ultrason. **15**, 1481 (2006).

165. G. T. Landi, S. A. Romero, and A. D. Santos, Rev. Sci. Instrum. **81**, 033908 (2010), clust.

166. L. He, X. Chen, Y. Mu, F. Song, and M. Han, Nanotechnology **21**, 495601 (2010).

167. F. Bødker, S. Mørup, S. W. Charles, and S. Linderoth, J. Magn. Magn. Mater. **196**, 18 (1999).

168. P. Milani, P. Piseri, E. Barborini, A. Podesta, and C. Lenardi, J. Vac. Sci. Technol. A **19**, 2025 (2001), clust.

169. P. Piseri, A. Podesta, E. Barborini, and P. Milania, Rev. Sci. Instrum. **72**, 2261 (2001), clust.

170. H. Haberland, Z. Insepov, and M. Moseler, Phys. Rev. B **51**, 11061 (1995), clust.

171. F. Voigt, R. Brüggemann, T. Unold, F. Huisken, and G. Bauer, Mater. Sci. Eng. C **25**, 584 (2005).

172. G. L. Bezemer, J. H. Bitter, H. P. C. E. Kuipers, H. Oosterbeek, J. E. Holewijn, X. Xu, F. Kapteijn, A. J. van Dillen, and K. P. de Jong, J. Am. Chem. Soc. **128**, 3956 (2006).

173. S. Gangopadhyay, G. C. Hadjipanayis, C. M. Sorensen, and K. J. Klabunde, IEEE T. Magn. **28**, 3174 (1992).

174. S. I. Woods, J. R. Kirtley, S. Sun, and R. H. Koch, Phys. Rev. Lett. **87**, 137205 (2001).

175. C. Petit, A. Taleb, and M.-P. Pileni, Adv. Mater. **10**, 259 (1998).

176. D. L. Peng, K. Sumiyama, S. Yamamuro, T. Hihara, and T. J. Konno, Phys. Status Solidi A **172**, 209 (1999).

177. J. F. Löffler, H.-B. Braun, and W. Wagner, Phys. Rev. Lett. **85**, 1990 (2000).

178. J. Perez, V. Dupuis, J. Tuaillon, A. Perez, V. Paillard, P. Melinon, M. Treilleux, L. Thomas, B. Barbara, and B. Bouchet-Fabre, J. Magn. Magn. Mater. **145**, 74 (1995).

179. T. Peter, O. Polonskyi, B. Gojdka, A. M. Ahadi, T. Strunskus, V. Zaporojtchenko, H. Biederman, and F. Faupel (2012), submitted.

180. A. Banerjee, R. Krishna, and B. Das, Appl. Phys. A **90**, 299 (2008).

181. W. M. Haynes and D. R. Lide, eds., *CRC Handbook of Chemistry and Physics* (CRC Press, Boca Raton, 2010), 91st ed., ch. 9.

182. T. Yamaki, M. Sekiya, and K. Tanaka, Chem. Phys. Lett. **376**, 487 (2003).

183. M. Li, J. Shi, Y. Nakamura, and R. Yu, Appl. Phys. A **89**, 807 (2007).

184. V. Hrkac, Ph.D. thesis, Christian-Albrechts-University of Kiel (to be published).

185. M. Panda, V. Srinivas, and A. K. Thakur, Appl. Phys. Lett. **93**, 242908 (2008).

186. Z. Rubin, S. A. Sunshine, M. B. Heaney, I. Bloom, and I. Balberg, Phys. Rev. B **59**, 12196 (1999).

187. J. F. Blackburn, M. Vopsaroiu, and M. G. Cain, J. Appl. Phys. **104**, 074104 (2008).

188. G. V. Duong, R. Groessinger, and R. S. Turtelli, IEEE T. Magn. **42**, 3611 (2006).

189. L. P. Curecheriu, M. T. Buscaglia, V. Buscaglia, L. Mitoseriu, P. Postolache, A. Ianculescu, and P. Nanni, J. Appl. Phys. **107**, 104106 (2010).

190. J. Xu and C. P. Wong, Appl. Phys. Lett. **87**, 082907 (2005).

191. S. D. Yoon, C. Vittoria, Y. N. Srivastava, A. Widom, and V. G. Harris, Appl. Phys. Lett. **92**, 042508 (2008).

192. V. Castel, C. Brosseau, and J. B. Youssef, J. Appl. Phys. **106**, 064312 (2009).

193. S. Sawa, N. Tanaka, R. Katoh, and K. Sumiyama, Mater. Trans. **49**, 1219 (2008).

194. D. Cohen, Science **175**, 664 (1972).

195. E. R. Flynn and H. C. Bryant, Phys. Med. Biol. **50**, 1273 (2005).

196. J. Malmivuo and R. Plonsey, *Bioelectromagnetism - Principles and Applications of Bioelectric and Biomagnetic Fields* (Oxford University Press, New York, 1995).

197. M. Mahmoudi, S. Sant, B. Wang, S. Laurent, and T. Sen, Adv. Drug Deliver. Rev. **63**, 24 (2011).

198. S. Knappe, T. H. Sander, O. Kosch, F. Wiekhorst, J. Kitching, and L. Trahms, Appl. Phys. Lett. **97**, 133703 (2010).

199. T. H. Sander, J. Preusser, R. Mhaskar, J. Kitching, L. Trahms, and S. Knappe, Biomed. Opt. Express **3**, 981 (2012).

200. H. Greve, E. Woltermann, H.-J. Quenzer, B. Wagner, and E. Quandt, Appl. Phys. Lett. **96**, 182501 (2010).

201. B. Gojdka, R. Jahns, K. Meurisch, H. Greve, R. Adelung, E. Quandt, R. Knöchel, and F. Faupel, Appl. Phys. Lett. **99**, 223502 (2011).

202. Nature **480**, 155 (2011), research highlight.

203. B. D. Cullity and C. D. Graham, *Introduction to Magnetic Materials* (John Wiley & Sons, Hoboken, NJ, 2009), pp. 270-271.

204. A. Ludwig and E. Quandt, IEEE T. Magn. **38**, 2829 (2002).

205. J. D. Livingston, phys. stat. sol. (a) **70**, 591 (1982).

206. R. L. Jones, Phys. Rev. Lett. **1**, 259 (1913).

207. S. Chikazumi, J. Phys. Soc. Japan **5**, 327 (1950).

208. B. S. Berry and W. C. Pritchet, Phys. Rev. Lett. **34**, 1022 (1975).

209. B. D. Cullity and C. D. Graham, *Introduction to Magnetic Materials* (John Wiley & Sons, Hoboken, NJ, 2009), ch. 10.

210. B. D. Cullity and C. D. Graham, *Introduction to Magnetic Materials* (John Wiley & Sons, Hoboken, NJ, 2009), pp. 338-345.

211. B. D. Cullity and C. D. Graham, *Introduction to Magnetic Materials* (John Wiley & Sons, Hoboken, NJ, 2009), p. 340.

212. J. M. Bustillo, R. T. Howe, and R. S. Muller, Proceedings of the IEEE **86**, 1552 (1998).

213. W. P. Eaton and J. H. Smith, Smart Mater. Struct. **6**, 530 (1997).

214. C.-M. Ho and Y.-C. Tai, Annu. Rev. Fluid Mech. **30**, 579 (1998).

215. W. Pang, H. Zhao, E. S. Kim, H. Zhang, H. Yuc, and X. Hu, Lab Chip **12**, 29 (2012).

216. M. R. J. Gibbs, J. Magn. Magn. Mater. **290-291**, 1298 (2005).

217. D. Lange, C. Hagleitner, A. Hierlemann, O. Brand, and H. Baltes, Anal. Chem. **74**, 3084 (2002).

218. T. Betts, C. Tipple, M. Sepaniak, and P. Datskos, Anal. Chim. Acta **422**, 89 (2000).

219. F. Battiston, J.-P. Ramseyer, H. Lang, M. Baller, C. Gerber, J. Gimzewski, E. Meyer, and H.-J. Güntherodt, Sensor. Actuat. B **77**, 122 (2001).

220. R. Raiteri, M. Grattarola, H. J. Butt, and P. Skadal, Sensor. Actuat. B **79**, 115 (2001).

221. H. F. Ji, K. M. Hansen, Z. Hu, and T. Thundat, Sensor. Actuat. B **72**, 393 (2001).

222. R. Osiander, S. A. Ecelberger, R. B. Givens, D. K. Wickenden, J. C. Murphy, and T. J. Kistenmacher, Appl. Phys. Lett. **69**, 2930 (1996).

223. T. R. Albrecht, P. Grütter, D. Horne, and D. Rugar, J. Appl. Phys. **69**, 668 (1991).

224. F. Lochon, I. Dufour, and D. R. é re, Sensor. Actuat. B **108**, 979 (2005).

225. H. Bhaskaran, M. Li, D. Garcia-Sanchez, P. Zhao, I. Takeuchi, and H. X. Tang, Appl. Phys. Lett. **98**, 013502 (2011).

226. N. Yoshizawa, I. Yamamoto, and Y. Shimada, IEEE T. Magn. **41**, 4359 (2005).

227. S. Baillet, J. C. Mosher, and R. M. Leahy, IEEE Signal. Proc. Mag. **18**, 14 (2001).

228. F. H. Raab, E. B. Blood, T. O. Steiner, and H. R. Jones, IEEE T. Aero. Elec. Sys. **15**, 709 (1979).

229. R. Jahns, H. Greve, E. Woltermann, E. Quandt, and R. Knöchel, Sensor. Actuat. A **183**, 16 (2012).

230. C. J. H. Brenan, P. G. Charette, and I. W. Hunter, Rev. Sci. Instrum. **63**, 3492 (1992).

231. S. K. Mandal, G. Sreenivasulu, V. M. Petrov, and G. Srinivasan, Appl. Phys. Lett. **96**, 192502 (2010).

232. S. M. Wu, S. A. Cybart, P. Yu, M. D. Rossell, J. X. Zhang, R. Ramesh, and R. C. Dynes, Nat. Mater. **9**, 756 (2010).

233. E. Lage, C. Kirchhof, V. Hrkac, L. Kienle, R. Jahns, R. Knöchel, E. Quandt, and D. Meyners, Nat. Mater. **11**, 523 (2012).

234. M. Hämäläinen, R. Hari, R. J. Ilmoniemi, J. Knuutila, and O. V. Lounasmaa, Rev. Mod. Phys. **65**, 413 (1993).

235. J. Nenonen and T. Katila, J. Clin. Eng. **16**, 423 (1991).

236. S. Marauska, R. Jahns, H. Greve, E. Quandt, R. Knöchel, and B. Wagner, J. Micromech. Microeng. **22**, 065024 (2012).

237. B. Lassagne, D. Ugnati, and M. Respaud, Phys. Rev. Lett. **107**, 130801 (2011).

238. S. Marauska, R. Jahns, C. Kirchhof, M. Claus, E. Quandt, R. Knöchel, and B. Wagner, in *Proceedings MME 2012* (Ilmenau, Germany, 2012), b05.

239. M. Dienel, M. Naumann, A. Sorger, D. Tenholte, S. Voigt, and J. Mehner, Vacuum **86**, 536 (2012).

240. Z. Kádár, A. Bossche, P. Sarro, and J. Mollinger, Sensor. Actuat. A - Phys. **70**, 225 (1998).

241. Y. Tao, A. P. Malshe, and W. D. Brown, Microelectron. Reliab. **44**, 251 (2004).

242. E. A. Pereira, A. L. Green, R. J. Stacey, and T. Z. Aziz, J. Clin. Neurosci. **19**, 27 (2012).

243. Wahajuddin and S. Arora, Int. J. Nanomed. **7**, 3445 (2012).

244. T. Neuberger, B. Schöpf, H. Hofmann, M. Hofmann, and B. von Rechenberg, J. Magn. Magn. Mater. **293**, 483 (2005).

245. M. Lewin, N. Carlesso, C.-H. Tung, X.-W. Tang, D. Cory, D. T. Scadden, and R. Weissleder, Nat. Biotechnol. **18**, 410 (2000).

246. *AE MDX 500 user manual*, Advanced Energy (v. 03/1997), p. 4-7.

247. *AE MDX 500 user manual*, Advanced Energy (v. 03/1997), p. 3-16.

List of Publications

In order of authorship appearance and chronological order

1. B. Gojdka, V. Hrkac, J. Xiong, M. Gerken, L. Kienle, T. Strunskus, V. Zaporojtchenko and F. Faupel, "*A critical evaluation of the 0-3 approach for magnetoelectric nanocomposites with metallic nanoparticles*", Journal of Applied Physics **112**, 044303 (2012)

2. B. Gojdka, V. Zaporojtchenko, V. Hrkac, J. Xiong, L. Kienle, T. Strunskus and F. Faupel, "*Highly versatile concept for precise tailoring of nanogranular composites with a gas aggregation cluster source*", Applied Physics Letters **100**, 133104 (2012)

3. B. Gojdka, R. Jahns, K. Meurisch, H. Greve, R. Adelung, E. Quandt and F. Faupel, "*Fully Integrable Magnetic Field Sensor based on delta-E Effect*", Applied Physics Letters **99**, 223502 (2011)

   This article was presented in the journal *Nature* as a "Research Highlight", Nature **480**, 155 (2011)

4. B. Gojdka, V. Hrkac, T. Strunskus, V. Zaporojtchenko, L. Kienle and F. Faupel, "*Study of cobalt clusters with very narrow size distribution deposited by high-rate cluster source*", Nanotechnology **22**, 465704 (2011)

5. K. Meurisch, B. Gojdka, T. Strunskus, V. Zaporojtchenko and F. Faupel, "*Vapour phase deposition of highly crystalline self-poled piezoelectric nylon-11*", Journal of Physics D: Applied Physics **45**, 055304 (2012)

6. T. Peter, O. Polonskyi, B. Gojdka, A. M. Ahadi, T. Strunskus, V. Zaporojtchenko, H. Biederman and F. Faupel, "*Influence of reactive gas admixture on transition metal cluster nucleation in a gas aggregation cluster source*", accepted